Please cite this article in press as: Shen et al., Electrochemical ammonia synthesis: mechanistic understanding and catalyst design, Chem (2021), https://doi.org/10.1016/j.chempr.2021.01.009

Chem

CellPress

Review

Electrochemical ammonia synthesis: mechanistic understanding and catalyst design

Huidong Shen,[1] Changhyeok Choi,[2] Justus Masa,[3] Xin Li,[1] Jieshan Qiu,[1] Yousung Jung,[2,*] and Zhenyu Sun[1,*]

SUMMARY

NH_3 production is dependent on the century-old Haber-Bosch process, which is energy and capital intensive and relies on H_2 from steam reforming, hence, contributing to greenhouse gas emissions. Electrochemical NH_3 synthesis can be realized by reaction of N_2 and a proton source under mild conditions powered by renewable electricity, which offers a promising carbon-neutral and sustainable strategy. However, N_2 has remarkable thermodynamic stability and requires high energy to be activated. Implementation of this "clean" NH_3 synthesis route therefore still requires significant enhancement in energy efficiency, conversion rate, and durability, which is only achievable through the design of efficient electrocatalysts. This article provides a timely theoretical and experimental overview of recent advances in the electrocatalytic conversion of N_2 to NH_3 underlining the development of novel electrocatalysts. Advances of *in situ* and *operando* studies for mechanistic understanding of the reaction and the main challenges and strategies for improving electrocatalytic N_2 reduction are highlighted.

INTRODUCTION

Ammonia plays a key role in sustaining life and the global chemical economy with an annual production exceeding 200 million tons.[1] The bulk of industrial NH_3 is primarily used to make fertilizers in agriculture (~80%) and to produce explosives, pharmaceuticals, refrigerants, and cleaning products (~20%). NH_3 is also being reckoned to be a potential fuel as well as ideal hydrogen carrier with a high gravimetric hydrogen content (~17.6 wt %) and large volumetric hydrogen energy density (10.7 kg H_2/100 L), in addition to advantages of easy liquefaction for handling, storage, and transportation. NH_3 fuel produces zero CO_2 and low overall emissions. N_2 is regenerated at the point of use and released into the atmosphere in a closed-cycle process. Currently, about 90% of the NH_3 produced worldwide still relies on the century-old, fossil-fuel-powered Haber-Bosch process, which entails thermocatalytic conversion of N_2 and H_2 ($N_2 + 3H_2 \rightarrow 2NH_3$ with a standard enthalpy of formation $\Delta H_f^0 = -45.9$ kJ mol^{-1} and standard Gibbs free energy $\Delta G_f^0 = -16.48$ kJ mol^{-1}) at high temperature (>300°C) and intense pressure (>15 MPa), over Fe- or Ru-based catalysts (utilized in the Kellog, Brown, and Root [KBR] advanced ammonia process [KAAP]) with promoters (such as Al_2O_3 and K). Recently, a nickel-loaded LaN catalyst was reported to be capable of accelerating the dissociation of N_2 (the kinetically determining step), comparable with ruthenium-based catalysts.[2] The Haber-Bosch process is among the top largest industrial chemical processes. The reaction has been claimed to be one of the greatest inventions of the 20th century and has been the subject of three chemistry Nobel prizes. However, it is capital intensive,

The bigger picture

Ammonia, the second largest synthetic chemical commercialized worldwide, is widely used as a fertilizer and is a key intermediate for production of all nitrogen-atom-containing chemicals. It could also be employed for fueling applications. Electrochemical N_2 reduction reaction (NRR) offers a renewable and distributed route for NH_3 production. Heightened research efforts have focused on the design and development of advanced electrocatalysts to enhance the efficiency of NRR to make it competitive against the Haber-Bosch process from the economic and ecological viewpoints. We describe the latest advances in the NRR from both theoretical and experimental aspects and provide a guide on how electrocatalysis of NRR could be improved. We discuss the roles of emerging *in situ* and *operando* methods in elucidating the dynamic catalyst structure and other reaction parameters. The possible reaction pathways and the major challenges in improving the NRR are also highlighted.

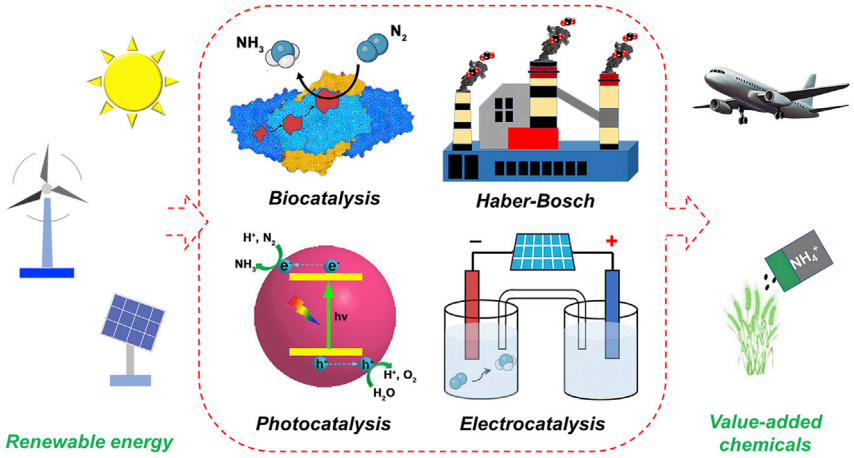

Figure 1. Schematic representation of nitrogen fixation processes, including biological, industrial, photocatalytic, and electrocatalytic NRR

requiring large and centralized plant infrastructure, and energetically demanding, requiring an energy input of ~485 kJ mol^{-1} (responsible for over 1% of the world's annual energy consumption). The process combines N_2 from the air with pure H_2 derived from endothermic steam-methane reforming (i.e., $CH_4 + H_2O \rightarrow CO + 3H_2$), consuming 3%–5% of global natural gas or other fossil resources (e.g., coal), which emits huge quantities of the greenhouse gas CO_2 into the atmosphere (from water gas shift, i.e., $CO + H_2O \rightarrow CO_2 + H_2$, the global average is ~2.86 tons of CO_2 released per ton of NH_3 and 1.6 tons of CO_2 released per ton of NH_3 in the most efficient plants).[3] The Haber-Bosch process also has a drawback of low energy efficiency with an NH_3 conversion of less than 15% per cycle (limited by thermodynamics). Demand for NH_3 continues to increase to support the growing global population. Hence, a high-efficiency, mild (avoiding unfavorable equilibrium issues), sustainable, and eco-friendly alternative approach to manufacturing NH_3 is of significant importance for both scientific research and industrial applications.

From these scenarios, three major clean routes for ammonia synthesis involving biocatalysis, photocatalysis, and electrocatalysis have sparked increasing research interest in recent years, as illustrated in Figure 1. Biological nitrogen fixation in nature is attained under mild conditions (<40°C, atmospheric pressure) by metalloenzyme nitrogenases that are composed of FeMo, FeV, or FeFe cofactor as active sites with FeMo being the most active and abundant enzyme for N_2 reduction.[4] A minimum of 16 moles of adenosine triphosphate (ATP) is necessary to reduce one mole of N_2 ($N_2 + 8H^+ + 8e^- + 16ATP \rightarrow 2NH_3 + H_2 + 16ADP + 16PO_4^{3-}$ where ADP is adenosine diphosphate) with concomitant formation of one mole of H_2 and a corresponding transfer of 8(e^-/H^+), not 6 (which could result in dissipative hydrolysis of 4 ATP).[5] As a consequence, production of one NH_3 consumes 8 ATP, requiring an energy input of 244 kJ mol^{-1}. However, biological nitrogen fixation occurs only in a select group of microorganisms, and the nitrogenases are susceptible to deactivation by oxygen.[6] In addition, biological conversion of nitrogen into NH_3 has a low space-time yield. Noteworthy, NH_3 production via natural processes cannot meet the current and future NH_3 needs. Photocatalytic NH_3 synthesis only requires solar energy, water, and N_2, encompassing two coupled redox half reactions, i.e., oxidization of water by photogenerated holes ($3H_2O$ [l] + $6h^+ \rightarrow 6H^+$ [aq.] + $3/2O_2$ [g]) in the valence band (VB) and reduction of N_2 via photogenerated electrons (N_2 [g] + $6H^+$ [aq.] + 6 $e^- \rightarrow 2NH_3$ [g]) in the conduction band (CB). Nonetheless, the overall

[1]State Key Laboratory of Organic-Inorganic Composites, College of Chemical Engineering, Beijing University of Chemical Technology, Beijing 100029, People's Republic of China

[2]Department of Chemical and Biomolecular Engineering, Korea Advanced Institute of Science and Technology (KAIST), Daejeon 34141, Republic of Korea

[3]Max Planck Institute for Chemical Energy Conversion, Stiftstr. 34-36, 45470 Mülheim an der Ruhr, Germany

*Correspondence: ysjn@kaist.ac.kr (Y.J.), sunzy@mail.buct.edu.cn (Z.S.)

https://doi.org/10.1016/j.chempr.2021.01.009

Please cite this article in press as: Shen et al., Electrochemical ammonia synthesis: mechanistic understanding and catalyst design, Chem (2021), https://doi.org/10.1016/j.chempr.2021.01.009

solar-to-chemical conversion efficiency is far from satisfactory owing to poor light utilization, low density of active sites, and rapid recombination of photoexcited electron-hole pairs.

Electrochemical synthesis of NH_3 was first demonstrated by Humphrey Davy in 1,807,[7] while a relevant patent was provided in 1908. Reliable quantification of NH_3 was achieved late in 1922 by Fichter and Suter.[8] Electrochemical synthesis of NH_3 via N_2 reduction is attractive because of (1) potentially higher energy efficiency than the Haber-Bosch process,[5] (2) environmental compatibility through coupling with carbon-free renewable energy resources (solar, tidal, and wind), (3) elimination of fossil fuels as H_2 sources whereby the required protons (H^+) are generated *in situ* from water oxidation, (4) flexible control of the reactions by adjusting external parameters (such as electrochemical voltage), being conducive to modular and small-scale operation, and (5) scalability and on-demand, on-site NH_3 production. This direct N_2 reduction process is supposed to be less capital intensive than a combined water electrolysis with Haber-Bosch process, which is only about 40% energy efficient.[9] Electrochemical N_2 reduction reaction (NRR) to generate NH_3 was mostly undertaken at high temperatures (above 500°C) using proton-conductive solid electrolytes before 2000.[10] However, this high-temperature route suffers from bottlenecks of low electronic and/or ionic conductivity in the electrolyte and NH_3 decomposition, in addition to the parasitic hydrogen evolution reaction (HER). To facilitate electrochemical NH_3 synthesis at lower temperatures (100°C–500°C), molten electrolytes with higher ion conductivity such as eutectic-based systems were attempted. Unfortunately, operations at such intermediate temperatures usually require large overpotentials, thus, decreasing energy efficiency at high current densities. Poor durability in the long-term operation is another issue of concern. The synthesis of NH_3 below 100°C using aqueous electrolytes has been the focus of interest since 2000, which was motivated by Nørskov and coworkers to mimic the FeMo cofactor in the nitrogenase enzyme.[11] This low-temperature synthetic process significantly reduces equipment and operational costs and increases stability of NH_3 produced for distributed deployment. However, binding and activation of N_2 under ambient conditions remains a grand challenge because the molecule is thermodynamically very stable and kinetically inert. Homogeneous (e.g., nitrogenase enzymes and molecular catalysts) and heterogeneous catalysts have been applied to accelerate this up-hill reduction reaction. Although high turnover number is attained in homogeneous catalysis, most homogeneous systems have high cost, toxicity, poor stability, and involve complex post-separation steps, but they are less likely the case in heterogeneous catalysis, thereby limiting their prospects for industrial application. Therefore, major endeavors have been devoted to developing heterogeneous electrocatalysts based on rational design approaches. However, despite recent advances achieved in this effort (Figure 2; Table S1), breakthrough progress is still hampered with (1) low faradic efficiency (FE) (typically not more than 15% due to the overwhelming HER catalyzed at similar or even lower overpotentials), (2) large overpotential (or low energetic efficiency), (3) slow kinetics resulting in small exchange current density, and (4) deactivation of electrodes in less than 100 h, restricting practical use and technological commercialization. High current efficiency (the fraction of electric charge that is used for the formation of NH_3) is usually obtained at the expense of a low NH_3 production rate, compromising the overall economic viability of the process. The majority of N_2 reduction electrocatalysts reported thus far operate below 20 mA cm^{-2}, which is, however, far less than that required for commercial electrolyzers. Under these circumstances, heightened research efforts have focused on the design and development of advanced electrocatalysts, toward lower energy cost to compete with the Haber-Bosch process and attainment of higher current density to minimize capital costs.

Please cite this article in press as: Shen et al., Electrochemical ammonia synthesis: mechanistic understanding and catalyst design, Chem (2021), https://doi.org/10.1016/j.chempr.2021.01.009

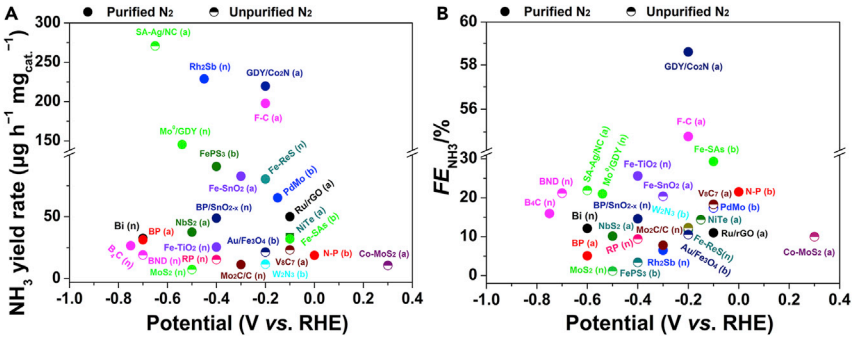

Figure 2. Summary of state-of-the-art various metallic and nonmetallic materials for aqueous electrocatalytic NRR under ambient conditions

(A) NH_3 yield rate at different applied potentials.

(B) FE of NH_3 at different applied potentials.

Full-filled circles and half-filled circles represent the process using purified N_2 and unpurified N_2, respectively. Acidic, basic, and neutral electrolytes are labeled by (a), (b), and (n) following the electrocatalysts, respectively.

Because of the high interest and rapid advances pertaining to this reaction, this article aims to provide a comprehensive and up-to-date review of nanostructured heterogeneous catalysts for the electrochemical NRR, with emphasis on relationships between structures and properties. A summary of the most important developments in catalyst design, and analytic tools and techniques for electrocatalytic N_2 reduction, as well as possible reaction mechanisms and pathways are presented. Next, we discuss the strategies available to tune the electronic structure of electrocatalysts and other relevant parameters in order to further enhance the performance and efficiency of electrochemical N_2 reduction. We also introduce emerging *in situ* and *operando* methods for investigations of the dynamic catalyst structure and other reaction parameters during the NRR. Finally, future challenges and opportunities of NH_3 synthesis by NRR are outlined.

FUNDAMENTALS OF ELECTROCHEMICAL N_2 REDUCTION

Electrochemical reduction of N_2 takes place at electrode-electrolyte interfaces and requires protons transferred from the electrolyte, electrons transferred from the electrode (catalyst), and optimized sites on the electrode surface onto which N_2 molecules can be adsorbed and subsequently activated. Three major elementary steps should be taken into account when modeling the fundamental processes: (1) diffusion and chemical adsorption of N_2 molecules and protons onto the cathode surface; (2) activation of N_2 and reductive addition of hydrogen atoms; and (3) rearrangement and desorption of the product, NH_3, or other products (e.g., hydrazine [N_2H_4] and diazene [N_2H_2]) from the electrode surface and migration into the electrolyte.

The presence of oxygen in the cathodic compartment deteriorates NRR performance, resulting in higher overpotentials. Moreover, aqueous electrocatalytic NRR is plagued by concomitant production of molecular hydrogen, similar to the cases in biological N_2 fixation and electrochemical CO_2 reduction.[12] This leads to low selectivity toward NH_3 formation and loss of efficiency, especially because the HER has intrinsically much faster kinetics compared with the NRR. For all metals, the HER proceeds at a more positive potential than for NH_3 synthesis.[13] Moreover, the rate of hydrogen production was modeled to be the first order in the electron and proton concentrations, while the rate of NH_3 production was zeroth order in both.[14] Hence, to boost the NRR, the availability and activity of protons at the

Please cite this article in press as: Shen et al., Electrochemical ammonia synthesis: mechanistic understanding and catalyst design, Chem (2021), https://doi.org/10.1016/j.chempr.2021.01.009

electrochemical interface, properties of the electrode, reaction conditions, and nature of the electrolyte should be manipulated to minimize the undesirable HER. Mitigating hydrogen evolution can be addressed by (1) selection of an electrolyte with reduced proton donor activity,[15] (2) addition of soluble coordination complexes to facilitate N–H bond formation by mediating net H atom transfers,[16] (3) optimization of reaction conditions (pH, applied potential, and reactor configuration),[17] (4) Li^+ association to decouple N_2 fixation and NH_3 evolution,[18] (5) engineering of electrode surface and electrode-electrolyte interface to regulate hydrophobicity (Figure 3A),[19] and (6) tuning of electrocatalysts to favor adsorption and binding of nitrogen instead of protons.[20] Figure 3B illustrates that diminishing proton concentrations by using an aprotic (or very alkaline) solvent offers an effective means to impede proton transfer thermodynamically. Figure 3C shows an alternative route to kinetically inhibit proton transfer by creating an aprotic and hydrophobic protection layers.

Another issue in NRR is the extremely low solubility of N_2 in aqueous electrolytes (water: ~0.00061 M at 25°C and P = 1 atm) because of its nonpolar nature, strong triple bond, and low polarizability, dramatically limiting the amount of N_2 available for reaction. To enhance N_2 dissolution, several strategies can be adopted: (1) employing low operating temperatures to reduce the Henry constant, (2) increasing N_2 feed gas pressure, (3) using non-aqueous electrolytes (such as aprotic ionic liquids), and (4) designing a hydrophobic mesoporous structure with high gas sorptivity that can adsorb N_2 but weaken interactions of water and the electrode surface. However, lowering the reaction temperature markedly restricts N_2 diffusion, and increasing operating pressure would add technological complexity and cost. Conversely, a flow rate of N_2 into catholyte below 10 sccm affects reaction kinetics, meanwhile, a higher N_2 flow rate should in principle result in larger quantitative rates and FEs, which, however, may level off above a flow rate of 20 sccm.[21] At higher flows, no effect of the gas flow rate and the position of the gas inlet was observed on the NRR results.[22] Coupling electrolytes with a high N_2 solubility and engineered electrocatalysts with a high density of N_2 adsorption sites appears to be a method of choice for enhanced NRR performance. In contrast, the low solubility and slow transport of N_2 can be overcome by design and use of gas diffusion electrodes to allow intimate contact between the gas, electrolyte, and catalyst.[23]

Parameters that may be useful in mechanistic analysis and benchmarking of electrocatalysts for the NRR include the following: (1) NH_3 production rate ($mg_{NH3}\ h^{-1}\ cm^{-2}$ or $mg\ h^{-1}\ mg_{cat.}^{-1}$); (2) FE (FE = $3nF/Q$, where 3 is the number of electrons transferred per NH_3 molecule, n is the number of moles for NH_3 produced, F is Faraday's constant (96,485 C mol^{-1}), and Q is all the charge passed during the electrolysis process); (3) overpotential (η, defined as the difference between the thermodynamic potential of NRR and the applied potential required to achieve a desired current density); (4) NRR current density at a specific electrode potential of cell voltage; (5) energy efficiency (EE% = $\Delta G_m^0/E$ = (1000 × FE × 339.2)/[3 × F × (1.23 − η)] assuming an ideal nonpolarizable anodic oxygen evolution reaction with no overpotential and kinetic limitation, where ΔG_m^0 represents the standard Gibbs free energy of NH_3 formation and E is the average mole energy input (kJ mol^{-1})); and (6) turnover frequency (TOF, s^{-1}), a measure of per-site activity of catalysts (i_o [A cm^{-2}] × FE/active site density (sites cm^{-2}) × [1.602 × 10^{-19} (C/e^{-1}) × $6e^{-1}/N_2$], where i_o refers to exchange current density). For the sake of accurate comparison between different materials, a combined figure of merit is preferred. In some cases, a single metrics may fail to accurately represent the catalytic property. FE is commonly used as a measure of the amount of charge that is effectively used for a specific faradic reaction relative to the total charge that flows. However, only comparing FE is unlikely

Please cite this article in press as: Shen et al., Electrochemical ammonia synthesis: mechanistic understanding and catalyst design, Chem (2021), https://doi.org/10.1016/j.chempr.2021.01.009

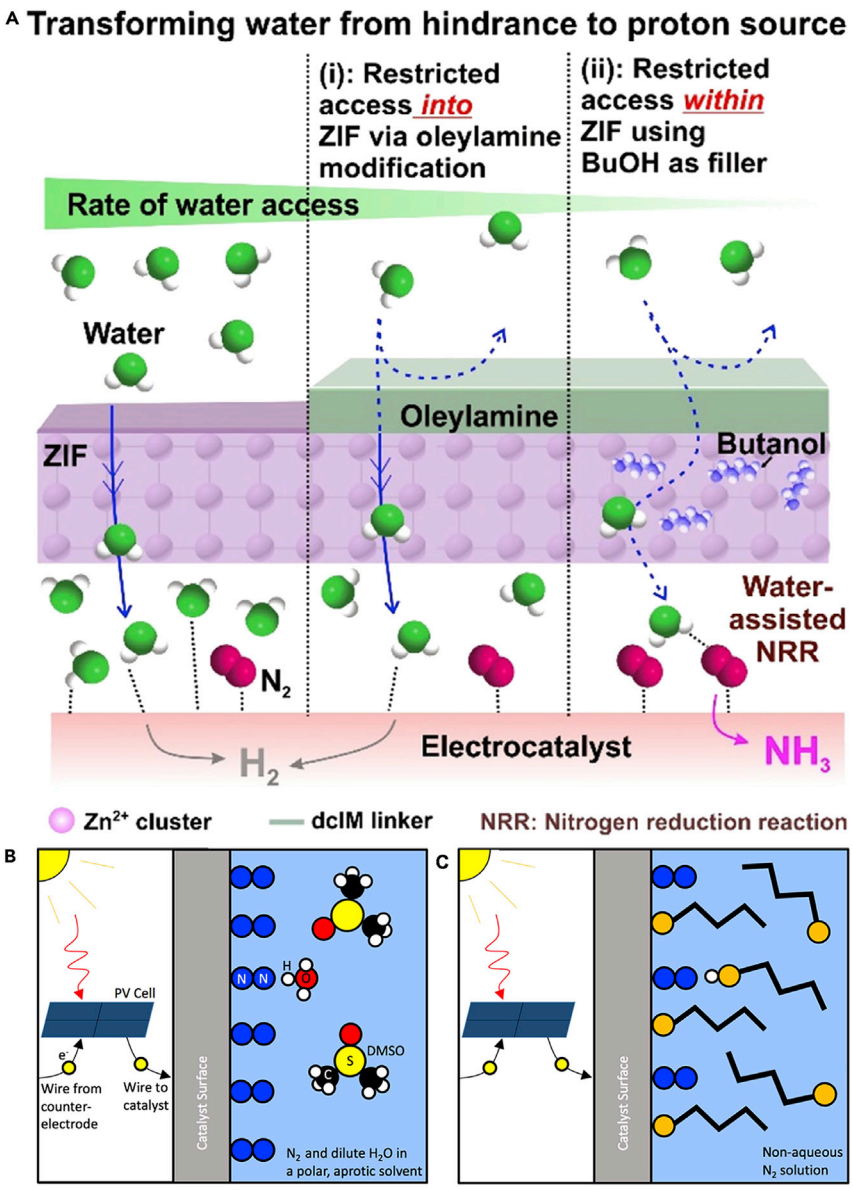

Figure 3. Strategies to improve selectivity of electrochemical NH_3 synthesis

(A) Transforming water into NRR proton source by surface modification with oleylamine and addition of butanol. Reprinted with permission from Koh et al.[19] Copyright 2020 American Chemical Society.

(B) Limiting proton transfer rate by reducing the concentration of protons in the bulk solution.

(C) Limiting proton transfer rate by increasing the barrier for proton transfer to the surface. Reprinted with permission from Singh et al.[14] Copyright 2017 American Chemical Society.

to give a complete picture of catalyst performance. Note that an improvement in FE may be not necessarily accompanied with an increase in yield rate. The latter is linked to product partial current density. A production rate normalized to electrochemical surface area (ECSA) provides information for intrinsic performance of a catalyst. While normalization based on geometric surface area is fundamental from the viewpoint of cost of a practical NRR cell. Additionally, high area-normalized NH_3 yield rate does not always mean large mass-normalized NH_3 yield rate. Reporting of both mass- and area-normalized NH_3 production is reasonable to compare N_2

Please cite this article in press as: Shen et al., Electrochemical ammonia synthesis: mechanistic understanding and catalyst design, Chem (2021), https://doi.org/10.1016/j.chempr.2021.01.009

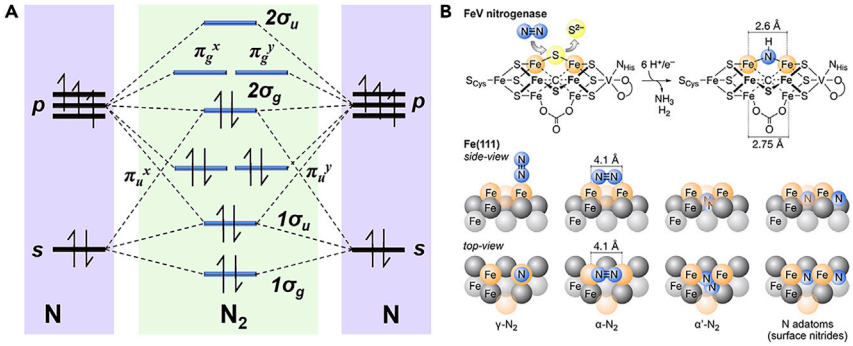

Figure 4. Simplified molecular orbital of N_2 and its binding modes

(A) Molecular orbital diagram.

(B) Proposed location of N_2 activation at the FeV cofactor (Top) and side-and top-views of the binding modes prior to the formation of μ-nitrides (i.e., linear Fe_2) on Fe(111) surfaces (Bottom). The top, second, and third layers of Fe are depicted with orange, dark gray, and light gray spheres, respectively. Reprinted with permission from Liu et al.[4] Copyright 2020 American Chemical Society.

fixation among different catalysts. To attain an efficient N_2 electrolyzer, it is indispensable to maximize NH_3 generation rate per unit of energy input, NH_3 partial current density at the highest energy efficiency as well as the energy efficiency at the largest partial current density.

The overall cell voltage required for NRR involves potentials for both the anode and cathode processes ($E_{cell} = E_{anode} - E_{cathode}$), where water oxidation ($3\,H_2O \rightleftharpoons 6\,H^+ + 3/2\,O_2 + 6e^-$, E^0[298 K] = +1.229 V [versus standard hydrogen electrode, SHE]) is recognized as the default anode process. Coupling this to cathodic NRR generates a minimum of several hundred millivolt overpotential for real-world electrocatalytic NRR. The role of the anode in NRR should not be neglected because it consumes almost half of the electrical input. Lowing oxygen evolution reaction overpotential and improving the anode efficiency can reduce the total energy cost of electrochemical NH_3 synthesis, thus, promoting the prospects of its practical implementation.

Thermodynamics and kinetics of NRR

An N_2 molecule comprises two nitrogen atoms bound by a disproportionately strong homonuclear triple bond. Each atom possesses a pair of electrons in the 2s orbital with opposite spin direction and three lone-pair electrons dispersed in the 2p orbitals with the same spin direction. Hybridization of the s-p atomic orbitals leads to formation of four bonding orbitals (two σ and two π orbitals) and four antibonding orbitals (two σ^* and two π^* orbitals), with the shared electrons in the π and 2σ orbitals forming an N≡N bond (Figure 4A).[24] From a thermodynamic perspective, NRR is feasible with overall negative Gibbs free energy. Nevertheless, activating N_2 at ambient conditions is a formidable challenge because of (1) large energy gap between the highest occupied molecular orbital (HOMO) and lowest unoccupied molecular orbital (LUMO) of N_2 (10.82 eV), impeding electron transfer; (2) high enthalpy of the first H atom addition to form N_2H^+ (ΔH^0 = +37.6 kJ mol^{-1}) before breakage of the N–N bond; (3) extreme stability and inertness of N_2 with high cleavage energy (945 kJ mol^{-1}) and first-bond breaking energy (410 kJ mol^{-1}), non-polarity (absence of permanent dipole), and large triplet state energy (6.17 eV); and (4) negative electron affinity (−1.9 eV), low proton affinity (5.12 eV), and large ionization potential (15.85 eV).

Electrochemical NRR proceeds through coupled or sequential proton/electron transfer processes, as summarized in Table 1. The former process seems to occur more

Please cite this article in press as: Shen et al., Electrochemical ammonia synthesis: mechanistic understanding and catalyst design, Chem (2021), https://doi.org/10.1016/j.chempr.2021.01.009

Table 1. HER and electrochemical NRR processes with corresponding equilibrium potentials

Equation	Reaction	E^0 (V)[25,26]
1	N_2 (g) + $6H^+$ (aq.) + $6e^-$ ⇌ $2NH_3$ (g)	0.0577 (versus SHE)
2	N_2 (g) + $8H^+$ (aq.) + $6e^-$ ⇌ $2NH_4^+$ (*aq.*)	+0.274 (versus SHE)
3	N_2 (g) + 8HBase$^+$ (*MeCN*[a]) + $6e^-$ ⇌ $2NH_4^+$ (*MeCN*) + 8Base	+0.361 – 0.079 pK_a (versus $Fc^{+/0}$)
4	N_2 (g) + $2H_2O$ (l) + $6H^+$ (*aq.*) + $6e^-$ ⇌ $2NH_3 \cdot H_2O$ (aq.)	+0.092 (versus SHE) or +0.23 (versus RHE)[b]
5	N_2 (g) + 6HBase$^+$ (MeCN) + $6e^-$ ⇌ $2NH_3$ (MeCN) + 6Base	+0.035 – 0.059 pK_a (versus $Fc^{+/0}$)
6	$2H^+$ (aq.) + $2e^-$ ⇌ H_2 (g)	0 (versus SHE)
7	N_2 + $6H_2O$ (l) + $6e^-$ ⇌ $2NH_3$ (g) + $6OH^-$ (aq.)	−0.736 (versus RHE, pH 14)
8	$2H_2O$ (l) + $2e^-$ ⇌ H_2 (g) + $2OH^-$ (aq.)	−0.828 (versus normal hydrogen electrode, NHE, pH 14)
9	N_2 (g) + H^+ (aq.) + e^- ⇌ N_2H (g)	−3.2 (versus RHE)
10	N_2 (g) + $2H^+$ (aq.) + $2e^-$ ⇌ N_2H_2 (g)	−1.10 (versus RHE)
11	N_2 (g) + 2HBase$^+$ (MeCN) + $2e^-$ ⇌ N_2H_2 (MeCN) + 2Base	−1.22 – 0.059 pK_a (versus $Fc^{+/0}$)
12	N_2 (g) + $4H^+$ (aq.) + $4e^-$ ⇌ N_2H_4 (g)	−0.33 (versus RHE)
13	N_2 (g) + 4HBase$^+$ (MeCN) + $4e^-$ ⇌ N_2H_4 (g) + 4Base	−0.398 – 0.059 pK_a (versus $Fc^{+/0}$)
14	N_2 (g) + $4H_2O$ (l) + $4e^-$ ⇌ N_2H_4 (g) + $4OH^-$ (aq.)	−1.16 (versus NHE, pH 14)
15	N_2 (g) + $5H^+$ (*aq.*) + $4e^-$ ⇌ $N_2H_5^+$(aq.)	−0.23 (versus RHE)
16	N_2 (g) + 5HBase$^+$ (MeCN) + $4e^-$ ⇌ $N_2H_5^+$(MeCN) + 5Base	−0.153– 0.074 pK_a (versus $Fc^{+/0}$)
17	N_2 (g) + e^- ⇌ N_2^- (aq.)	−4.16 (versus NHE) or −3.37 (versus RHE, pH 14)

[a]Acetonitrile.
[b]Thermodynamic equilibrium potential is calculated based on Nernst equation.

favorably than the latter one with lower energetic barriers, while the disruptive two-electron HER is also more severe at similar potentials in aqueous electrolytes (Equations 4 versus 6; Equations 7 versus 8). Multiple intermediates (such as N_2H_4 and N_2H_2) may be involved during the concerted proton-electron transfer steps.[25,26] The addition of the first H atom to form N_2H (Equation 9) demands a rather negative equilibrium potential (−3.2 V versus reversible hydrogen electrode, RHE), while an even more negative potential is needed for the first electron transfer to yield N_2^- (Equation 17). At a high pH of 14, Equation 17 may compete with Equation 9 provided a weak affinity for $*N_2H$ (* represents an active site on a catalyst) but a stabilizing interaction of the catalyst with the N_2^-. The preferred pathway between concerted proton-electron transfer and sequential proton-electron transfer was recently reported to be pH dependent. However, the majority of theoretical calculations of NRR thus far did not consider the pH impact. Hence, further exploration in this regard is necessary.

An advanced catalyst likely entails catalytic centers in favor of electron transport that are in close proximity to sites providing protons. However, it is very unlikely for electrochemical reduction of N_2 to be kinetically limited by proton concentration in electrolyte, which would occur if the mass transport of protons cannot match the NRR rate that reaches the highest value for a specific system. In a typical electrochemical process, the activity increases exponentially with overpotential. However, this is not the case for the NRR, in which the performance first increases with overpotential in the small overpotential regimes but declines at relatively larger overpotentials. The drop of the NRR rate may be due to two possibilities: (1) the mass-diffusion limitation and (2) fewer available $*N_2$ molecules for further hydrogenation in light of the fact that the electron and proton transfer steps of $*N_2$ molecules are more rapid at

Please cite this article in press as: Shen et al., Electrochemical ammonia synthesis: mechanistic understanding and catalyst design, Chem (2021), https://doi.org/10.1016/j.chempr.2021.01.009

higher reducing voltages.[27] This is likely to be associated with the competitive HER, in which higher surface coverage of *H occurs at larger overpotentials, while the N_2 adsorption rate does not lean on potential. The surface coverage of $*N_2$ decreases owing to occupation of active sites by *H, thus, resulting in the decline of NRR activity.

Adsorption of N_2 and the linear scaling relationships

Adsorption and binding of N_2 is essential for initiation of the NRR. In Fe_7MS_9C cofactors (M = Mo, V, or Fe) of nitrogenase enzymes, a "belt" position that spans two low-coordinate Fe ions (d_{Fe-Fe} = ca. 2.6 Å, Figure 4B) has been proposed for N_2 adsorption.[28] In industrial NH_3 synthesis, it is supposed that specific multi-iron centers bind and activate N_2. Following initial physisorption through end-on N_2 binding (γ-N_2, Figure 4B), the adsorbate transforms into a bridging, side-on binding mode (α-N_2, Figure 4B) preceding N–N bond scission.[4]

A high-performing NRR electrocatalyst should have an "ideal" binding strength for N according to the Sabatier principle. A too strong bonding implies high coverage and surface poisoning, while a too weak adsorption entails very low coverage and thus low reaction rate. Transition metals such as Ti, Y, Sc, and Zr were calculated to possess a higher affinity toward N compared with hydrogen, benefiting NRR.[29] Fe, Mo, and many other transition metals were predicted to chemically adsorb N_2 forming metal-nitrogen bonds as a result of the interaction between the metals and the N 2p states.[30] Noble metals including Rh, Ru, Au, Pt, and Ir exhibit appropriate N binding strength, but they also have a strong ability to bind hydrogen. Pt and Ir even display stronger binding of hydrogen relative to N_2, detrimental to NRR. Cu and Ag were calculated to have weak binding for N_2, while Re showed an exceptionally large adsorption energy for N_2, hindering the reaction in both cases.[31] Unlike pure metals, transition metal nitrides such as ZrN, NbN, chromium nitride (CrN), and vanadium nitride (VN) were believed to trigger NRR by way of a Mars-van Krevelen mechanism,[32,33] in which a surface N atom is reduced to NH_3 and the catalyst later regenerated with dissolved N_2, rather than adsorbing N_2 to the catalyst surface in the first step. Apart from the aforementioned N_2 binding configurations, new active sites to adsorb N_2, such as surface carbon[34] and oxygen vacancies in metal oxides[21,35] as well as electron-deficient atoms (as Lewis bases) in boron-doped graphene,[36] have recently been identified and demonstrated to facilitate NRR.

The multi-step six-electron NRR involves several different transition states. N_2 bound to the surface may be directly broken into adsorbed N atoms or first partly reduced by generating an N_2–H bond followed by further hydrogenation and dissociation. The adsorption energy of the intermediates and activation barrier for N_2 dissociation were encoded by the Brønsted-Evans-Polanyi (BEP) linear correlation typically on the surfaces of metals.[13] Transition metals were suggested to be limited by the scaling relations between the binding energy of $*N_2H$ generation and *NH protonation. Transition metal nitrides are also limited by the weak binding for $*N_2H$ formation but strong binding for *N protonation. This renders it difficult to design an active catalyst that can cleave the N–N bond to yield the $*N_2H$ intermediate but not bind NH_x intermediates too strongly for reasonable catalytic turnovers. Indeed, no metals were found to display a combination of intermediate nitrogen binding and low energy N_2 scission transition state, as depicted at the bottom middle of the plot in Figure 5.[37] On the other hand, selectivity for NRR is restricted by the scaling between the free energy changes of the HER step and *N (in the nitride case) or *NH (in the metal case) protonation or $*N_2H$ formation. Consequently, to attain efficient

Please cite this article in press as: Shen et al., Electrochemical ammonia synthesis: mechanistic understanding and catalyst design, Chem (2021), https://doi.org/10.1016/j.chempr.2021.01.009

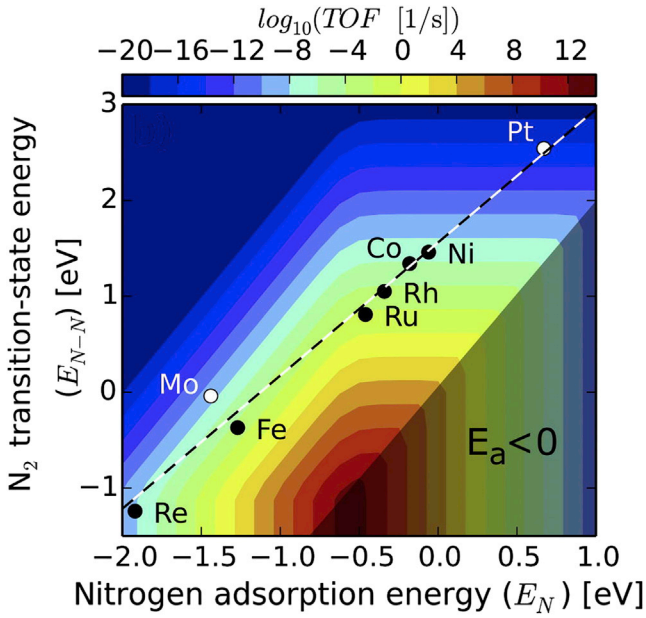

Figure 5. Linear scaling between nitrogen-binding energy and activation barrier for N_2 dissociation (TOF: turnover frequency; E_a: activation energy)
Reprinted with permission from Medford et al.[37] Copyright 2015 Elsevier.

NRR, it is required to break the energetic linearity constrains between key intermediates (*H, *NH_x, or N_2H_x species where x = 0–2). To this end, new or coordinated catalyst design schemes (through geometric and electronic effects as well as electronic dynamics) need to be developed. Exploration of promoters and solvents beyond H_2O may be another alternative route.[38]

Protocols for N_2 electrolysis

Confirmation of product origin (from N_2 or not)

Particular caution should be taken when performing NRR due to ambient ammonia contamination.[1,39] As early as 1984, minor amounts of nitrate or nitrite impurities in alkali electrolytes were reported to undergo cathodic reduction very readily, contributing predominantly to the reported yield of NH_3.[40] Therefore, stringent experimental protocols should be adapted for NRR to avoid misinterpretation of results (false positives). This precaution was reiterated recently by Chorkendorff and coworkers, who proposed a measurement protocol to alleviate the possibility of misinterpretation of NRR data due to adventitious NH_3 contamination, as shown in Figure 6.[1] Any labile nitrogen-containing contaminants that may stem from electrocatalysts (especially those that involve nitrogen species originating from their preparation), electrochemical reactor, chemicals (solvents, electrolytes), air, supplied N_2 gas, human breath, sample tubing, Nafion membranes, lab coats, nitrile gloves, glassware, downstream traps, and stale Milli-Q water, among others must be excluded.[41] Virtually, high levels of NO_3^-, NO_2^-, and nitrides of up to 1,610 ± 48 ppm were detected in some commercial metal oxides/metallic irons.[42] To fully verify a genuine NRR, at a minimum, a set of rigorous control and verification experiments (for multiple repeats at each condition) need to be conducted in either Ar-saturated electrolyte (under exactly the same conditions as the NRR experiments), or under N_2 without catalyst, or with the binder, or at an open circuit potential, or N_2-Ar alternate cycling, or by exposing the electrolyte in the air for extended periods.[43] It is essential to quantify and confirm the levels of ionic and gaseous NO_x

Please cite this article in press as: Shen et al., Electrochemical ammonia synthesis: mechanistic understanding and catalyst design, Chem (2021), https://doi.org/10.1016/j.chempr.2021.01.009

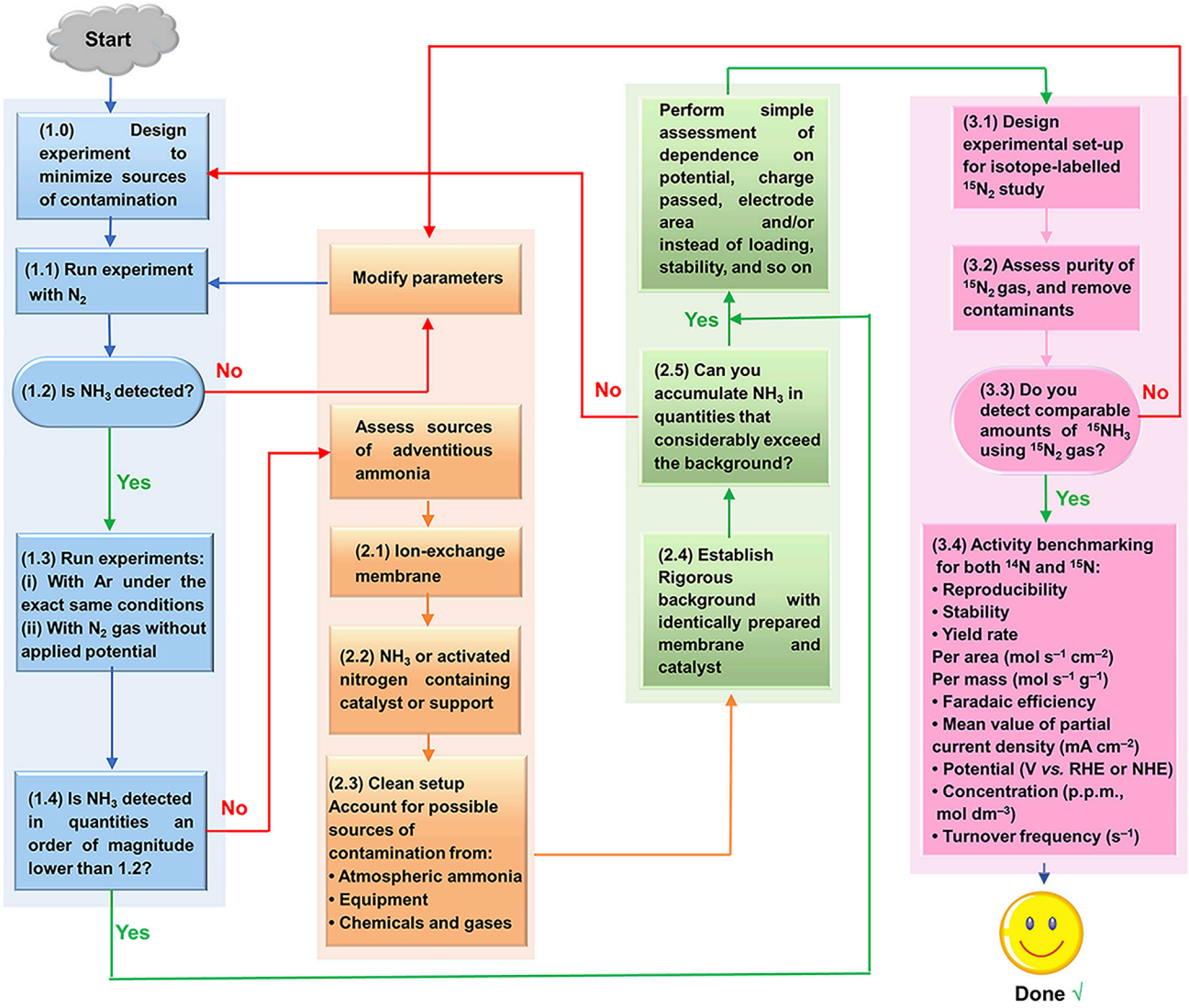

Figure 6. Suggested experimental protocol for NRR

compounds before carrying out NRR measurements. Isotopic labeling using molecules such as $^{15}N_2$ in combination with isotope-sensitive proton nuclear magnetic resonance spectroscopy (^{1}H NMR) should ideally be carried out to confirm the actual reduction of N_2 (especially for catalysts that either contain nitrogen in their structures or are prepared from nitrates or ammonium precursors), namely detection of solely $^{15}NH_4^+$ (featuring a symmetric doublet at 7.12 ppm with a spacing of ~73.2 Hz as opposed to a triplet for $^{14}NH_4^+$ at 7.12 ppm with a spacing of ~52.2 Hz). If appreciable $^{14}NH_4^+$ is generated, nitrogen is most likely present in other extraneous sources. Under the same conditions, the amount of NH_3 produced by the $^{15}N_2$ test should be consistent with the corresponding $^{14}N_2$ test. Also, repeats of measurements (over 3 times) should be performed for each catalyst type/composition to validate that NH_3 production is repeatable and reliable.

Purification of N_2 feed gas, electrolyte salts, and electrocatalysts

Perhaps more importantly, the purged N_2 gas ($^{14}N_2$ and $^{15}N_2$) should be scrubbed to remove any possible NH_3 and nitrogen oxides (NO_x) prior to starting NRR. The NO_x

Please cite this article in press as: Shen et al., Electrochemical ammonia synthesis: mechanistic understanding and catalyst design, Chem (2021), https://doi.org/10.1016/j.chempr.2021.01.009

species (NO, NO_2, and N_2O) are thermodynamically and kinetically more facile to be reduced than N_2.[44] A 10 ppm of reducible N-impurities could potentially result in about 4.0 μg per hour of NH_3 or other nitrogen-containing compounds.[39] This dramatically affects precise quantification of NH_3 from NRR in light of the fact that typical NH_3 yields are in the range of 10–1,000 nmol. It is worth noting that the level of NH_3 and NO_x impurities in almost all $^{14}N_2$ gas (with a purity $\leq$99.999%) reported for NRR is uncertain or not specified. In addition, the isotopically labeled $^{15}N_2$ feedstock (with a purity mostly $\leq$99.9%) can be contaminated with impurities (as high as 0.1%), mainly in the forms of ^{15}N-ammonia, ^{15}N-nitrite/nitrate, and ^{15}N-nitrous oxide.[45] These point to the necessity of additional N_2 purification. Removal of extraneous NH_3 contamination can be readily addressed by passing the feed gas through H_2SO_4 as adsorbent. The nitrite/nitrate and NO_2 are soluble in water and therefore can be effectively absorbed and eliminated from the stock gas by the aqueous solution. NO and other sparingly soluble NO_x pollutants can be transformed into N_2 and H_2O via selective catalytic reduction (SCR) of NO_x with NH_3 in a fixed-bed quartz tube reactor over Cu-based catalysts or $Ce_{0.1}Ti_{0.9}O_2$[46] at 300°C for 1 h, followed by repeated absorption and removal of NH_3 in H_2SO_4 solutions (confirmed by detection before NRR test). Alternatively, these N-species can be oxidized (to NO_3^-) and removed by use of a dual oxidant solution ($H_2O_2/S_2O_8^{2-}$) at 50°C and pH of 11.[47] During gas purification, special care should be taken to avoid new adventitious contamination.

In light of the possible presence of impurities (such as NO_x^-, nitrides) in electrolyte salts and electrode materials, they should be treated at high temperatures or washed with KOH solution before use to remove the contaminants. The actual amounts of NO_x and nitrides should be determined and reported after the treatments.

Cleaning of pretreated PEMs right before use

A proton exchange membrane (PEM) (such as Nafion 211 and Nafion 117) is utilized in a typical electrochemical NRR cell allowing the crossover of protons and inhibiting the diffusion of O_2 from the anodic compartment to the cathodic compartment. Before applying a Nafion membrane in the electrochemical cell, it is commonly pretreated using (3.0–5.0)% H_2O_2 aqueous solution at 80°C to eliminate organic impurities and subsequently (0.1–1.0) M H_2SO_4 at 80°C to remove metallic species and to protonate the membrane, which is further washed with ultrapure water. However, some amounts of NH_3 from the atmosphere especially in highly populated and polluted regions may be adsorbed on the membrane, thus, interfering with the NRR results. Hence, directly prior to use in NRR, the pretreated membrane should be cleaned by ultrasonication (or extensive soaking) in diluted H_2SO_4 and ultrapure water. This enables effective extraction of NH_4^+ from Nafion into the solution, minimizing the effect of environmental ammonia contamination.

Quantification of ammonia

Six main types of techniques, including (1) spectrophotometry, (2) ion chromatography, (3) ion-selective electrode (ISE), (4) fluorescence, (5) ^{1}H NMR, and (6) ultra-high-performance liquid chromatography mass spectrometry (UPLC-MS) have been proposed to determine the amount of NH_3 produced during NRR. Current electrochemical NRR studies are heavily reliant on aqueous-based spectrophotometric/colorimetric assays using indophenol blue[48] and Nessler's reagent,[49] which are well-established with advantages of good sensitivity (0–0.6 $mg_{NH3\text{-}N}$ L^{-1}) and low cost. The indophenol blue method, or the salicylate method, is based on the modified Berthelot reaction, in which ammonia reacts with sodium salicylate and

Please cite this article in press as: Shen et al., Electrochemical ammonia synthesis: mechanistic understanding and catalyst design, Chem (2021), https://doi.org/10.1016/j.chempr.2021.01.009

hypochlorite in an alkaline solution to produce indophenol blue that absorbs at 655 nm.[50] The Nessler's reagent method follows a reaction of ammonia with iodide and mercury ions to generate a reddish-brown complex absorbing at 420 nm. Although this method requires less reagents and shorter detection time than the salicylate method, the Nessler's reagent is highly toxic and has a lifetime of only 3 weeks. Additional pretreatments, for example by sodium potassium tartrate ($KNaC_4H_4O_6 \cdot 4H_2O$) solution, are needed to eliminate metallic ions (Fe^{3+}, Ni^{2+}, Co^{2+}, Cr^{3+}, and Ag^+), sulfides (S^{2-}), and organics that could interfere with the Nessler's reagent (a solution of K_2HgI_4 and KOH).

Ion chromatography is a well-known alternative method. It provides benefits of low detection limit (3×10^{-7} mol L^{-1}), good reproducibility, precision, and rapid detection of multiple ions at the same time, provided with suitable columns (such as Dionex IonPac CS16-4mm Column) and eluents.[41] However, Na^+-involving electrolytes are unsuitable attributed to overlapping of the Na^+ and NH_4^+ peaks as well as its short retention time.[51] Additionally, challenges remain in isotopically differentiating $^{14}NH_3$ from $^{15}NH_3$ because $^{15}NH_4^+$ and H_3O^+ share the same nominal *m/z*, which cannot be addressed even by using advanced coupled ion chromatography mass spectrometry (IC-MS).

Two types of ISEs have been demonstrated for measuring ammonia nitrogen.[52] One is ammonia-selective electrode via testing potential difference emanating from diffusion of generated NH_3 gas through a hydrophobic membrane (typically PTFE). The ammonia/ammonium concentration in the solution can, thus, be determined according to the Nernst equation. The other is ammonium-ion-sensing electrode with a polyvinylchloride (PVC) membrane containing an ammonium carrier. All NH_3 in samples is converted to NH_4^+ by acidification for measurement. The ISE method offers advantageous features of convenience, large detection range (0.03–1,400 $mg_{NH3\text{-}N}$ L^{-1}) with high concentration of ammonia nitrogen, and suitability for continuous monitoring.[52] However, the inherent poor sensitivity of ISE especially for ammonia nitrogen at low concentrations (< 0.5 $mg_{NH3\text{-}N}$ L^{-1}) limits its widespread application.

The fluorometric method involves the reaction of ammonium with *o*-phthaldialdehyde (OPA) and sulfite featuring high sensitivity (detection limit of 1 nmol L^{-1}) and was first developed by Cohn and Lyle in 1966.[53] Despite attempts to improve sensitivity, this method suffers from interference by amino acids and amines, affecting ammonium measurements.

^1H NMR has been widely used for quantification of NH_4^+ in biocatalytic and homogeneous catalytic N_2 reduction.[54] In contrast to indirect spectrophotometry and ion chromatography protocols, the ^1H NMR method is direct and highly selective for analysis of both $^{14}NH_4^+$ and $^{15}NH_4^+$ (concentration in the range 5–10 μM with a 600-MHz NMR spectrometer and 1 μM with a 900-MHz NMR spectrometer).[55] However, it suffers from laborious ammonia isolation via distillation. In addition, suboptimal NMR settings lead to lengthy data acquisition time and influence accurate quantification.

UPLC-MS was recently reported to distinguish and quantify $^{14}NH_3$ (MS peak at m/z = 251.0854 for ^{14}N) and $^{15}NH_3$ (MS peak at m/z = 252.0825 for ^{15}N).[56] This analytical method was developed based on a dansyl chloride derivatization process by mixing dansyl chloride and ammonia solutions at optimal pH (~9.5 $\pm$ 0.5). An ammonia concentration in the range of 0.6–43.5 μM was claimed to be rapidly measured for both $^{14}NH_3$ and $^{15}NH_3$.

Please cite this article in press as: Shen et al., Electrochemical ammonia synthesis: mechanistic understanding and catalyst design, Chem (2021), https://doi.org/10.1016/j.chempr.2021.01.009

Note that each of these methods has advantages and limits for assaying ammonia. To evaluate the overall level of accuracy and accountability, it is strongly recommended to use a combination of different approaches. Moreover, it is imperative to develop more selective, sensitive, accurate, and robust protocols for ammonia quantification, as well as *in situ* and continuous processes for monitoring the NRR.

Quantification of by-products

From the Equations 10 and 12 (Table 1), N_2H_2 and N_2H_4 are also produced during NRR as by-products, respectively. Such by-products may reduce the FE of ammonia; however, these are important indicators for identifying reaction pathway of NRR. The observation of N_2H_2 and N_2H_4 is an evidence for that the alternative pathway is preferred to the distal pathway (Figure 8), and thus, the observation of by-products has been employed for *in situ* mechanistic studies of NRR (discussed in detail in the subsequent Mechanistic understanding of NRR section).[57,58] Diazene is unstable and can be easily decomposed into ammonia and nitrogen in the electrolyte. Thus, diazene has not been quantified during the NRR while it has been detected by *in situ* mechanistic studies on NRR.[57,58] For example, in a spectroscopic method to quantify the hydrazine in electrolytes, known as the method of Watt and Chrisp,[59] a mixture of *p*-dimethylaminobenzaldehyde, ethanol, and concentrated HCl is used as a color reagent. Calibration curve is obtained by using a mixture of color reagent and N_2H_4 solution in dilute HCl (0.1 M) with different N_2H_4 concentrations. The absorbance of the resulting solution is obtained at 458 nm. In this method, the optimum concentration range of hydrazine is 0.06 to 0.47 ppm, where the relative error does not exceed 1%.

Electrolytes

Electrolytes serve as a hydrogen source and also provide a medium to trap N_2 and transfer protons and intermediates. Engineering of electrolytes can decrease the ionic resistance in the electrochemical reactor, which is particularly critical for energy efficiency at high currents. Akin to many other electrochemical reactions, the proton activity, donor identity, the acid dissociation constant, and ion conductivity of electrolytes affect activation barriers and reaction rates of NRR. However, further in-depth experimental and theoretical investigations of electrolyte effects are required. Electrolytes are generally classified into six types, including (1) liquid electrolytes (aqueous solutions, organic solvents, and ionic liquids with operating temperature $\leq$50°C),[15,41,60] (2) molten salt electrolytes (molten 0.5 NaOH/0.5 KOH, molten LiOH, eutectic of LiCl, KCl, and CsCl with Li_3N operated between 200°C and 500°C),[60] (3) polymer membrane electrolytes (Nafion N117 and 102 membranes, sulfonated polysulfone membrane operated from room temperature to 80°C),[60] (4) composite membrane electrolytes (Na, K, and Li carbonates mixed with $LiAlO_2$ operated at 400°C),[60] (5) O_2^--conducting membrane electrolytes (doped ZrO_2, doped Bi_2O_3, doped CeO_2, doped $LaGaO_3$ at A and B sites, doped $BaSrO_3$ and $SrCeO_3$, and Y_2O_3-ZrO_2 operated at 650°C),[60] and (6) ceramics/inorganic proton conducting solid electrolytes (Yb doped Sr-cerate, $SrCe_{0.95}Yb_{0.05}O_{3-\delta}$, $BaCe_{0.9}Sm_{0.1}O_{3-\delta}$ + $BaCe_{0.8}Gd_{0.1}Sm_{0.1}O_{3-\delta}$ complex perovskites, Gd-doped barium cerate, $Ce_{0.8}M_{0.2}O_{2-\delta}$ [M = La, Y, Gd, Sm], $Ba_3(Ca_{1.18}Nb_{1.82})O_{9-\delta}$, $Ba_3CaZr_{0.5}Nb_{1.5}O_{9-\delta}$, $Ba_3Ca_{0.9}Nd_{0.28}Nb_{1.82}O_{9-\delta}$, $La_{1.9}Ca_{0.1}Zr_2O_{6.95}$, Ca^{2+}-doped $La_2M_2O_7$ [M = Ce, Zr], $La_{1.95}Ca_{0.05}Zr_2O_7$, $La_{1.95}Ca_{0.05}Ce_2O_7$, and $SrZr_{0.95}Y_{0.05}O_{3-\delta}$ operated in the range 450°C–750°C).[60] The majority of ambient electrocatalytic NRR studies are conducted in liquid electrolytes. Recent progress in this regard will be discussed in the following. For the other electrolytes, readers are referred to earlier reviews.[60]

Please cite this article in press as: Shen et al., Electrochemical ammonia synthesis: mechanistic understanding and catalyst design, Chem (2021), https://doi.org/10.1016/j.chempr.2021.01.009

Aqueous solutions (acidic, neutral, and alkaline solutions)

Most studies on electrochemical NRR at mild conditions have concentrated on acidic, neutral, or basic N_2-saturated aqueous electrolytes with OH^-, SO_4^{2-}, or Cl^- anions and alkali metal cations (e.g., Na^+ and K^+).[61] The pH and counterions of electrolytes impact the energetics of adsorbed intermediates and solvated ions. Acidic electrolytes favor HER while alkaline electrolyte suppresses proton supply and transfer. Electrolysis in acidic media can cause accumulation of ammonium salts in the electrolyte and alteration of the solution's pH, rendering them poorly amenable to successive and long-term operation. Lower electrolyte pH may lead to a positive shift of equilibrium potential resulting from easier protonation of as-formed NH_3 into NH_4^+. However, decreasing pH also results in enhanced HER through proton reduction. Manipulation of proton concentrations in electrolytes enables one to increase surface coverage of N_2 instead of H and accelerate the rate of formation and consumption of early NRR intermediates,[16] thereby promoting NRR over HER. However, the impact of electrolytes on NRR is apparently not universal. This may be associated with variations in cell configurations, inherent properties of electrocatalysts, impurity effects in electrolytes, and local pH environments, among others.[41]

Specifically, adsorbed alkaline cations in the inner Helmholtz plane (IHP) alter the potential of the outer Helmholtz plane (OHP) and can also block hydrogen adsorption, thereby limiting the HER.[17,62] Meanwhile, cations were proposed to be solvated by water in the OHP, favoring N_2 adsorption. Unlike CO_2 reduction, cations with a smaller radius were found to favor better NRR activity, following the trend $Li^+ > Na^+ > K^+ > Cs^+$.[63] In addition, the 2p orbitals of adsorbed nitrogen were calculated to shift to lower energies in the presence of K^+, which facilitated electron transfer to *NNH for N–N activation.[17]

Hitherto, the effects of anionic species on NRR have been rarely explored. Anions with different buffer capacities (e.g., HCO_3^- and $H_2PO_4^-$) are likely to affect the local pH at the electrode and hence the NRR selectivity. Also, PO_4^{3-} was calculated to easily adsorb N_2 via bonding thus increasing N_2 solubility in water.[64] Adsorbed phosphate and halides (i.e., Br^-, Cl^-, or I^-) may form a bond with metal electrodes, thus, promoting electron transfer from these anions to the vacant orbital of N_2 and boost N_2 reduction. Additionally, specifically adsorbed halides may hinder proton adsorption and induce a larger HER overvoltage.

Organic electrolytes

Most organic electrolytes exhibit an N_2 solubility that is 1 or 2 orders of magnitude higher than that of water. Use of organic solutions affords substantially enhanced N_2 dissolution (toluene: 5 mmol L^{-1}, trifluorotoluene: 10 mmol L^{-1}, cyclohexane: 7 mmol L^{-1}, 1H,1H,2H-heptafluorocyclopentane: 12 mmol L^{-1}, heptane: 9.1 mmol L^{-1}, perfluoroheptane: 17.9 mmol L^{-1}, perfluorotributylamine: 11.8 mmol L^{-1}, ethanol: 20.0 mmol L^{-1}, 2-propanol: 23.0 mmol L^{-1})[65,66] and also regulates the supply of H^+ to favor N_2 adsorption onto electrode surface, benefiting NRR. In this context, a number of organic-based electrolyte mixtures, such as 0.2 M $LiClO_4$ in ethanol/tetrahydrofuran,[67] 0.1 M $LiClO_4$ in methanol/0.03 mol L^{-1} H_2SO_4,[68] 0.01 M H_2SO_4 in 2-propanol/water (9: 1, v/v),[69] 0.1 M LiCl in ethylenediamine,[70] 0.2 M $LiCF_3SO_3$ in ethanol/dry tetrahydrofuran,[71] and 1 M $LiBF_4$ in ethanol/dry tetrahydrofuran[72] have been applied to enhance NRR over the competing HER. In lithium (Li)-mediated N_2 reduction, Li^+ ions from solution in a polar, aprotic solvent are reduced to Li metal, which easily splits the nitrogen triple bond to form lithium nitride (Li_3N). The Li_3N then reacts with a proton source/carrier

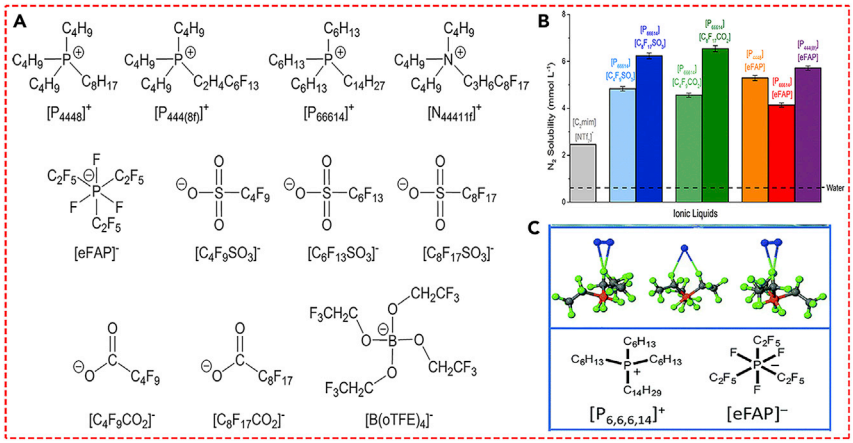

Figure 7. ILs and their interaction and solubilities for N_2

(A) Structures and abbreviations of phosphonium-based ILs paired with highly fluorinated anions.

(B) N_2 solubilities (molar concentration, mmol L^{-1}) of fluorinated ILs at 30°C and P = 1 atm. Data for water and [C_2mim][NTf_2] (at 25°C) are shown for comparison. Reprinted with permission from Kang et al.[73] Copyright 2018 American Chemical Society.

(C) Structures of the [$P_{6,6,6,14}$][eFAP] ions and their interaction with N_2. Reprinted with permission from Zhou et al.[15] Copyright 2017 Royal Society of Chemistry.

(such as ethanol) to yield NH_3. The proton carrier was claimed to play important roles in promoting both Li nitridation to form Li_3N and its further protonation to evolve NH_3.[72] However, the stability and mechanistic understanding of organic electrolytes need to be further elucidated.

Ionic liquids

Ionic liquids (ILs) with wide electrochemical stability windows are promising electrolytes for efficient NRR.[15] A family of phosphonium-based ILs with highly fluorinated anions were reported to have remarkable N_2 solubility (Figures 7A and 7B).[73] The already high N_2 solubility of these ILs could be further enhanced by the addition of fluorinated solvents, trifluorotoluene, 1H,1H,2H-heptafluorocyclopentane, and 1H,1H,5H-octafluoropentyl 1,1,2,2-tetrafluoroethyl ether (FPEE) that lack strong interactions (i.e., from hydrogen bonding, or functional groups).[66] The ionic conductivity and fluidity were improved as well. Notably, the (1-butyl-1-methylpyrrolidinium tris(pentafluoroethyl)trifluorophosphate ([C_4mpyr][eFAP])-FPEE binary electrolytes were observed to enable NRR with a high FE (32.0%) and yield rate (2.35×10^{-11} mol cm^{-2} s^{-1}) for NH_3 formation over α-Fe nanorods.[74] Despite this success, $^{15}N_2$ isotopic labeling experiments need to be performed to confirm the accuracy of the activity data. Manipulation of IL structures by changing electric potential or nanopore confinement provide another way to further improve the solubility of N_2.[75] Apart from high solubility for N_2, the IL, [C_4mpyr][eFAP], was also found to stabilize the N_2H intermediate via interaction of the F–CF_2 atom in $[FAP]^-$ with the N_2H group, thus, increasing both NRR activity and selectivity (Figure 7C).[76]

The high price and viscosity (causing diffusional transport limitations) are downsides of ILs for practical use in N_2 electrolysis. Nevertheless, the high viscosity of ILs can be circumvented by dilution with a controlled quantity of an aprotic solvent (or a mixture of solvents), while retaining their functionality. Despite the high cost of ILs, some can be recovered and reused, rendering electrolyzers that use ILs economic to a certain extent. To date, only a limited number of ILs have been examined for NRR, further

Please cite this article in press as: Shen et al., Electrochemical ammonia synthesis: mechanistic understanding and catalyst design, Chem (2021), https://doi.org/10.1016/j.chempr.2021.01.009

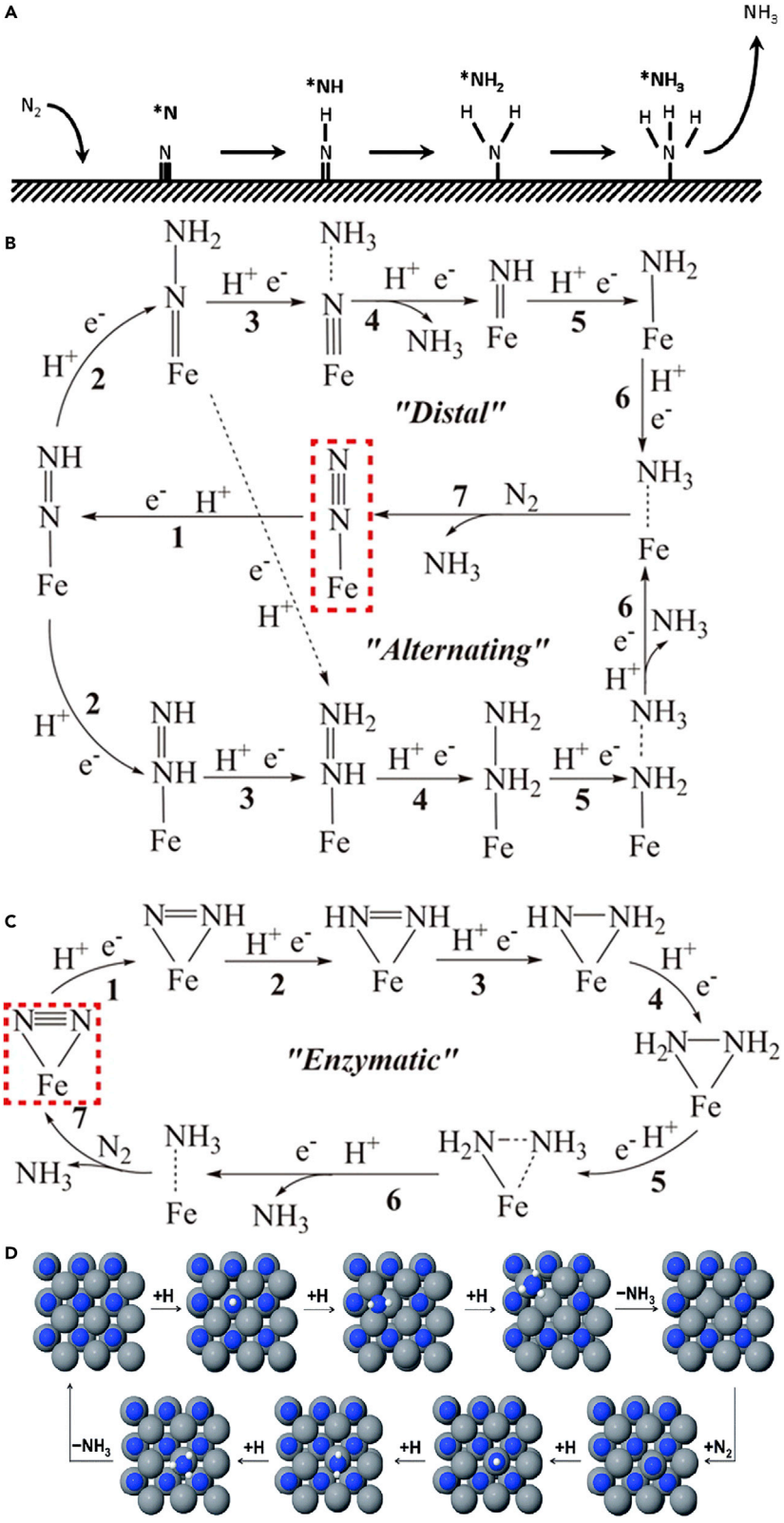

Please cite this article in press as: Shen et al., Electrochemical ammonia synthesis: mechanistic understanding and catalyst design, Chem (2021), https://doi.org/10.1016/j.chempr.2021.01.009

Figure 8. Schematics of possible reaction mechanisms of ammonia synthesis

(A) Dissociative pathway. Reprinted with permission from van der Ham et al.[26] Copyright 2014 Royal Society of Chemistry.

(B) Distal pathway and alternative pathway.

(C) Enzymatic pathway. Reprinted with permission from Li et al.[77] Copyright 2016 American Chemical Society.

(D) Mars-van Krevelen mechanism on transition metal nitride. Gray, blue, and white balls indicate transition metal, nitrogen, and hydrogen atoms, respectively. Reprinted with permission from Abghoui et al.[33] Copyright 2015 Royal Society of Chemistry.

search and development of specially tailored N_2-philic IL systems in combination with advanced *in situ* mechanistic studies would be suitable subjects of focus in the future.

Mechanistic understanding of NRR

Reaction mechanisms

Conventional mechanism of nitrogen reduction in industry. To date, most of ammonia has been produced by the Haber-Bosch process, for which there exist many extensive reviews. Here, we very briefly summarize the widely accepted mechanism of NH_3 synthesis by the Haber-Bosch process for comparison purposes with the electrochemical NRR, the focus of this review. In the conventional Haber-Bosch process, N_2 and H_2 react on heterogeneous catalysts such as Fe and Ru. Ammonia synthesis by the Haber-Bosch process has been generally believed to follow a dissociative mechanism where the adsorbed N_2 ($*N_2$) dissociates into N adatoms (*N) before undergoing hydrogenation (Figure 8A).[26] The *N is then hydrogenated to $*NH_3$ via *NH and $*NH_2$. This dissociative mechanism is generally considered for nitrogen reduction at high temperature (e.g., Haber-Bosch process) to overcome the energy barrier for dissociation of the highly stable N–N triple bond (bond energy = 226 k_{cal}/mol). Since electrochemical NRR is usually conducted at low temperature (<100°C), sluggish dissociation of the N–N triple bond makes the dissociative mechanism highly unlikely in electrochemical NRR.

Associative mechanism. In nature, enzymes called nitrogenases can produce ammonia from nitrogen, solvated protons, and electrons, via a so-called nitrogen fixation process. Contrary to Haber-Bosch process, nitrogenases can facilitate the reduction of N_2 more efficiently even at ambient conditions. The active site of nitrogenases is an FeMo cofactor consisting of an Mo/Fe/S cluster.[78] The overall reaction of nitrogen reduction by nitrogenases is:

$$N_2 + 8H^+ + 8e^- \rightarrow 2\,NH_3 + H_2. \qquad \text{(Equation 13)}$$

In addition to nitrogenases, many homogeneous catalysts (to mimics of nitrogenases) have been studied for ammonia synthesis at ambient conditions.[79] Three different mechanisms have been proposed, namely, distal pathway, alternating pathway, and enzymatic pathway, which are variations of the associative mechanistic pathway (Figures 8B and 8C).[26,77] Unlike the dissociative mechanism (Figure 8A), in which the N–N triple bond is instantaneously ruptured, the adsorbed N_2 molecule ($*N_2$) is protonated sequentially, breaking the triple bond consecutively, hence requiring relatively less energy to drive the reaction. Since N_2 can be adsorbed in two different geometries called end-on (η^1-N_2) and side-on (η^2-N_2), both geometries should be considered. In case of end-on adsorbed N_2, both the distal pathway and the alternating pathway are considered. In the distal pathway, the first NH_3 is desorbed simultaneously with hydrogenation of $*NNH_2$ ($*NNH_2 + (H^+ + e^-) \rightarrow *N + NH_3$), while the first NH_3 is desorbed simultaneously with hydrogenation of adsorbed hydrazine ($*NH_2NH_2 + (H^+ + e^-) \rightarrow *NH_2 + NH_3$) in the alternating pathway.

Please cite this article in press as: Shen et al., Electrochemical ammonia synthesis: mechanistic understanding and catalyst design, Chem (2021), https://doi.org/10.1016/j.chempr.2021.01.009

A

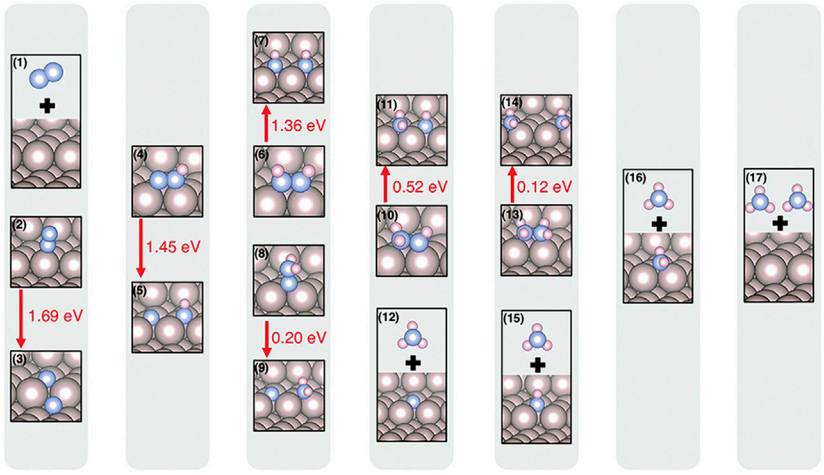

B

Mechanisms	PDS	U_L (V)
Associative mechanism	$*NH_2 \rightarrow * + NH_3$	−0.68
Dissociative mechanism	$2*NH_2 \rightarrow *NH_2 + NH_3$ Kinetically difficult N–N dissociation	−0.71
Dissociation of $*N_2H_2$	$2*NH_2 \rightarrow *NH_2 + NH_3$	−0.71
Dissociation of $*NH_2NH$	$2*NH_2 \rightarrow *NH_2 + NH_3$	−0.71
Dissociation of $*NH_2NH_2$	$2*NH_2 \rightarrow *NH_2 + NH_3$	−0.71

Figure 9. Possible NRR mechanism on Ru surface including various N–N bond dissociation steps and reaction free energy obtained by DFT calculations

(A) Activation energy of N–N bond dissociation in all reaction intermediates of NRR on Ru surface. Gray, blue, and ivory atoms indicate Ru, N, and H atoms, respectively.

(B) A summary of various possible reaction mechanisms of NRR on Ru surface. PDS and U_L indicate PDS and limiting potential, respectively.

Reprinted with permission from Back et al.[80] Copyright 2016 Royal Society of Chemistry.

In the enzymatic pathway, each nitrogen atom in side-on adsorbed N_2 is reduced alternatively similar to the alternating pathway.

Reaction mechanism of NRR on heterogeneous catalysts. Similar to homogeneous catalysts, heterogeneous catalysts generally follow the associative mechanism, and thus, most theoretical studies in literatures have also considered the conventional associative mechanism. However, other reaction pathways are also possible on heterogeneous catalysts. Contrary to single-metal sites (or small metal clusters) in homogeneous catalysts, metal surfaces can dissociate the N–N bond without the addition of a proton and electron ($H^+ + e^-$) pair.

A theoretical study on NRR over Ru surface showed that reaction pathways involving various N–N bond dissociation steps yield the NRR activity that is comparable with the associative mechanism with a similar limiting potential, suggesting the importance of considering all possible reaction pathways in addition to the conventional associative mechanism (Figure 9).[80] For example, $*NNH_2$, $*NHNH_2$, and $*NH_2NH_2$ can be dissociated into $*N + *NH_2$, $*NH + *NH_2$, and $*NH_2 + *NH_2$, respectively,

Please cite this article in press as: Shen et al., Electrochemical ammonia synthesis: mechanistic understanding and catalyst design, Chem (2021), https://doi.org/10.1016/j.chempr.2021.01.009

with low activation energy (0.20~0.52 eV), while these reaction steps are not involved in the conventional associative mechanism. Also, *in situ* studies of NRR on Ru thin film using surface-enhanced infrared absorption spectroscopy (SEIRAS) found N_2H_2 (diazene) as an intermediate product where the N_2H_2 can be decomposed or further protonated to ammonia. It can be noted that the latter reaction steps have not been considered in conventional associative mechanism. Thus, it is important to consider various potential pathways in order to describe correctly the mechanism and activity of NRR on heterogeneous catalysts.

Now, we turn to the strategies for designing efficient NRR catalysts informed by in-depth understanding of the reaction mechanism of NRR. The overall reaction and equilibrium potential for NRR involving one N_2 molecule and six proton-electron pairs can be expressed below:

$$N_2 + 6\,(H^+ + e^-) \rightarrow 2\,NH_3.\ (E^0 = 0.05\ \text{V versus NHE}) \qquad \text{(Equation 1)}$$

The equilibrium potentials of several reaction intermediates (N_2H, N_2H_2, and N_2H_4) in the associative pathway are known, and are presented in Table 1.

Although the formation of NH_3 (g) from N_2 (g) and H_2 (g) is slightly exothermic ($\Delta G_f^0 = -16.4$ kJ/mol), NRR is thermodynamically hindered by the negative equilibrium potentials of these reaction intermediates. Notably, the equilibrium potential of N_2H (g) formation, corresponding to the first protonation step in NRR, is highly negative, indicating that NRR via the associative mechanism is limited by the first protonation step.[26] Theoretical volcano plots of NRR also have shown that the first protonation step (*N_2H formation) is the thermodynamic limiting step for most catalysts, and hence, catalysts that can strongly bind N_2H favor NRR (Figures 10A and 10B).[26,29,38] In addition to stabilizing adsorbed N_2H (*N_2H), destabilization of *NH_2 is also important to design catalysts with low overpotential for NRR. A previous theoretical study has shown that the limiting step for NRR is the first protonation step ($N_2 + [H^+ + e^-] \rightarrow$ *N_2H) on weak N-binding metal surfaces, meanwhile, for strong N-binding metal surfaces, the limiting step is the final protonation step (*NH_2 + $(H^+ + e^-) \rightarrow NH_3$) (Figure 8).[38] Thus, the strategies for lowering NRR overpotential include stabilizing *N_2H and destabilizing *NH_2 independently to reduce the free energy change for $N_2 + (H^+ + e^-) \rightarrow$ *N_2H and *$NH_2 + (H^+ + e^-) \rightarrow NH_3$, respectively.

Recently, a surface-hydrogenation pathway is suggested for the NRR on noble-metal catalysts (right-leg of the volcano), such as Pd and Au.[81] The potential-determining step (PDS) is *NNH formation on Pd and Au surfaces with 1~3 eV of free energy (Figure 10A), and the experimental NRR activity is observed at lower overpotentials (Table S1). Using DFT calculations, Ling et al.[81] showed that the activation energy of *N_2H_2 formation via the surface-hydrogenation step (N_2(g) + 2*H $\rightarrow$ *N_2H_2) is lower than the formation energy of *NNH (N_2(g) + $[H^+ + e^-] \rightarrow$ *NNH) on Pd and Au surfaces (Figures 10C and 10D), indicating that the N_2 is activated by surface *H rather than surface metal atoms. After *N_2H_2 formation via surface-hydrogenation, the following reactions proceed by the addition of $(H^+ + e^-)$ exothermically (Figure 10E).

NRR mechanism on transition metal nitrides (Mars-van Krevelen mechanism)

The reaction mechanism of NRR on transition metal nitrides is different from NRR of pure or alloy transition metal surfaces, since surfaces of transition metal nitride are already covered by nitrogen atoms (nitride). On transition metal nitrides, not only N_2 feed gas but also surface nitride can be reduced to ammonia. Thus, transition metal nitrides could involve surface nitride atoms as reactants in NRR and follow a

Please cite this article in press as: Shen et al., Electrochemical ammonia synthesis: mechanistic understanding and catalyst design, Chem (2021), https://doi.org/10.1016/j.chempr.2021.01.009

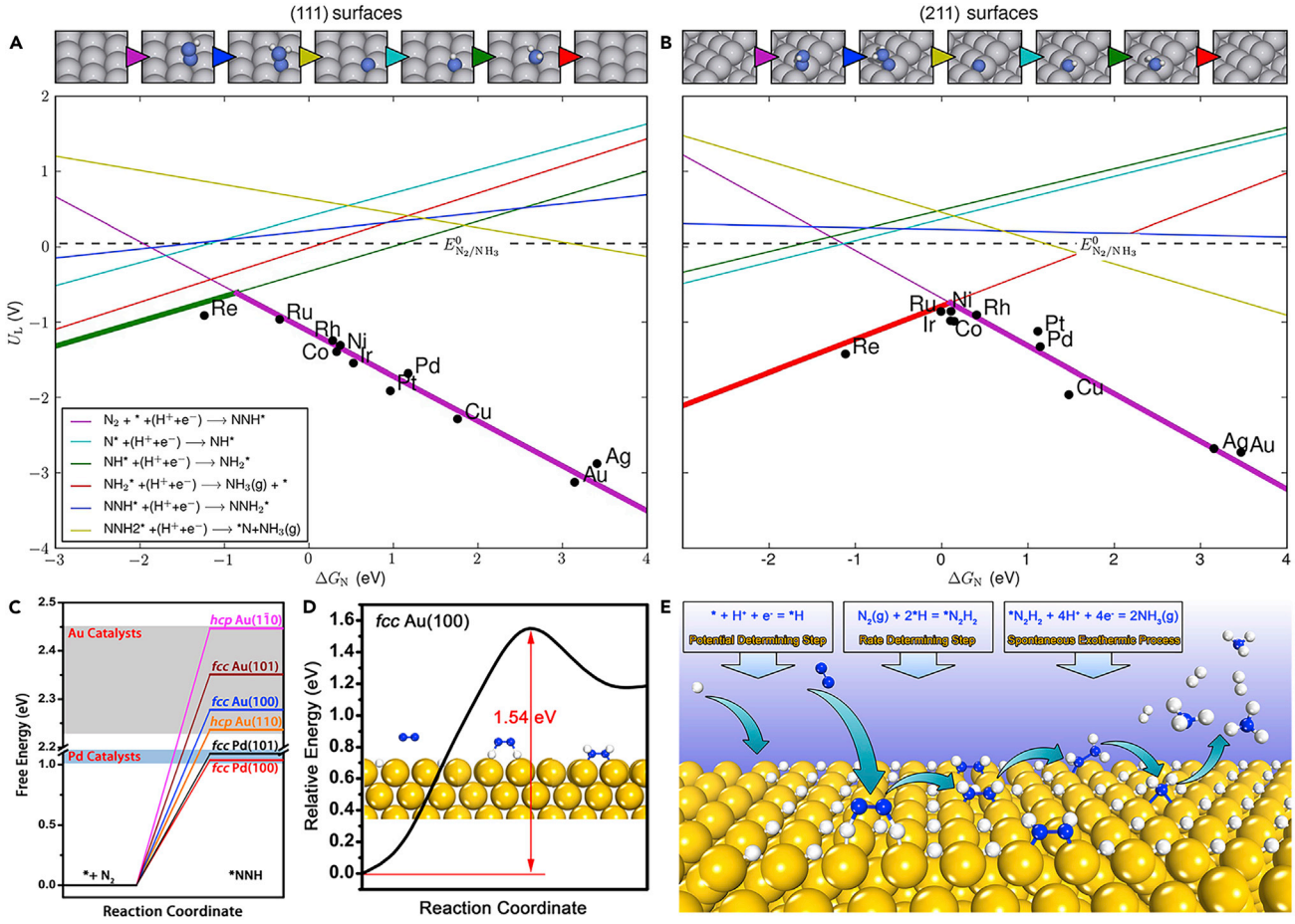

Figure 10. Volcano plot for limiting potentials (U_L) of NRR as a function of *N-binding energy descriptor for *fcc* metal surfaces and surface-hydrogenation mechanism on noble-metal catalysts

(A) U_L for NRR as a function of *N binding on *fcc*(111) surfaces.

(B) U_L for NRR as a function of *N binding on *fcc*(211) surfaces. Reprinted with permission from Montoya et al.[38] Copyright 2015 Wiley-VCH.

(C) *NNH formation free energy via * + N_2(g) → *NNH on Au and Pd surfaces.

(D) Minimum-energy pathway of *N_2H_2 formation via the hydrogenation of N_2 (N_2(g) + 2*H → *N_2H_2) on Au(100) surface.

(E) Schematic of NRR on noble-metal-based catalysts via the surface-hydrogenation mechanism. Reprinted with permission from Ling et al.[81] Copyright 2019 American Chemical Society.

so-called Mars-van Krevelen mechanism, which is generally considered for catalytic oxidation reactions on transition metal oxides. In this mechanism, surface nitride rather than N_2 feed gas is first reduced to ammonia leaving a surface nitride vacancy. Then, the N_2 feed gas regenerates the surface recovering the nitride vacancy and can be further reduced to ammonia. Skúlason and coworkers first suggested that several transition metal nitrides including CrN and VN can electrochemically reduce nitrogen to ammonia with low potential via the Mars-van Krevelen mechanism based on DFT calculations.[33] More recently, quantitative isotope (^{15}N) experiments combined with DFT calculations demonstrated that VN indeed reduces nitrogen to ammonia via the Mars-van Krevelen mechanism.[82]

Insights from in situ *and* operando *studies*

In situ/*operando* techniques enable one to probe reaction intermediate states, identify real active sites, and provide insight into their dynamic evolution. *Operando* investigation also permits identification of degradation modes of a catalyst. These

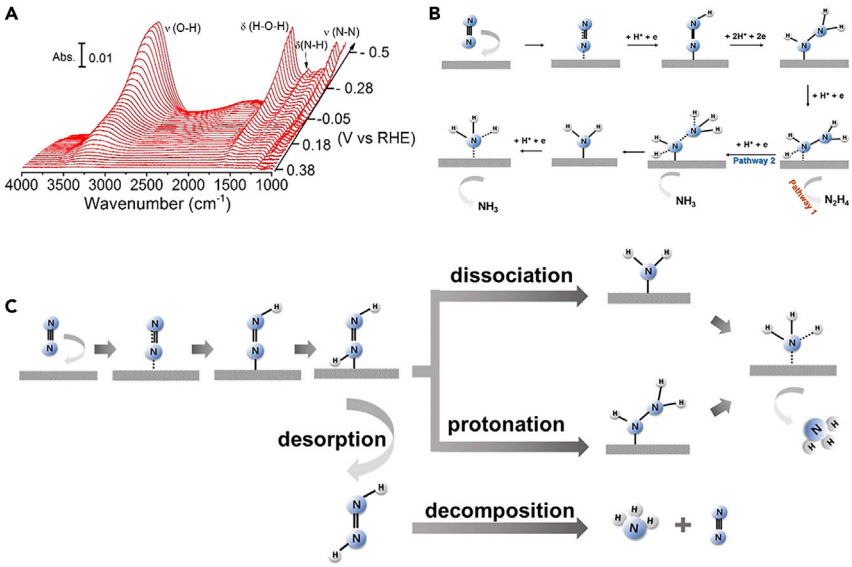

Figure 11. FTIR spectra and reaction mechanisms of NRR on Au, Ru, and Rh thin film electrodes

(A) FTIR spectra during NRR on an Au film electrode in N_2-saturated 0.1 M KOH solutions.

(B) Proposed NRR mechanism on Au surface. Reprinted with permission from Yao et al.[83] Copyright 2018 American Chemical Society.

(C) Proposed NRR mechanism on Ru surface. Reprinted with permission from Yao et al.[57] Copyright 2019 American Chemical Society.

are highly important for fundamental understanding of reaction mechanisms and rational design of improved catalysts. Despite growing interest in this regard, *in situ* mechanistic research of NRR is still in its early stages.

In situ *(surface-enhanced) infrared absorption spectroscopy.* In 2018, Shao et al. detected reaction intermediates of NRR on Au thin films using a SEIRAS technique.[83] They confirmed the bands in the infrared (IR) spectrum that were attributed to H–N–H bending, $–NH_2$ wagging, and N–N stretching of $*N_2H_y$ ($3 \leq y \leq 4$) species with increasing electrode potential and identified reaction intermediates during NRR (Figure 11A). One of the key findings was that Au follows an alternative pathway of the associative mechanism, which involves N_2H_4 as an intermediate (Figure 11B).

More recently, the SEIRAS technique revealed the NRR mechanism on a Ru surface. During NRR, the IR signal of N=N in $*N_2H_x$ ($0 \leq x \leq 2$) species was detected at potentials below 0.2 V in 0.1 M $HClO_4$ solutions.[57] However, these bands were not observed in alkaline solutions, indicating that N_2 molecules are not easily adsorbed on Ru in alkaline electrolytes. Unlike Au (Figure 11B), Ru involved N_2H_2 as reaction intermediate not N_2H_4. The N_2H_2 on the Ru surface could then be decomposed or further reduced to ammonia (Figure 11C). In contrast to Ru that is inactive in alkaline media, Rh was shown to manifest apparent IR signals from the end-on $*N_2H_x$ between 0.2 and −0.4 V in KOH solutions.[58] The NRR on Rh was inferred to proceed via a two-electron transfer pathway to form an N_2H_2 intermediate, which subsequently decomposed to produce NH_3 in the electrolyte. Based on *in situ* Fourier-transform infrared (FTIR) investigations, an associative alternating mechanism was also deduced for NiFe-MoS_2 nanocubes,[84] Fe-doped ReS_2,[85] Al-doped Co_3O_4 nanospheres,[86] and nonmetallic N, B dual doped carbons,[87] while the NRR was speculated to proceed through an associative distal pathway over phosphorus-doped carbon nanotubes.[88]

Please cite this article in press as: Shen et al., Electrochemical ammonia synthesis: mechanistic understanding and catalyst design, Chem (2021), https://doi.org/10.1016/j.chempr.2021.01.009

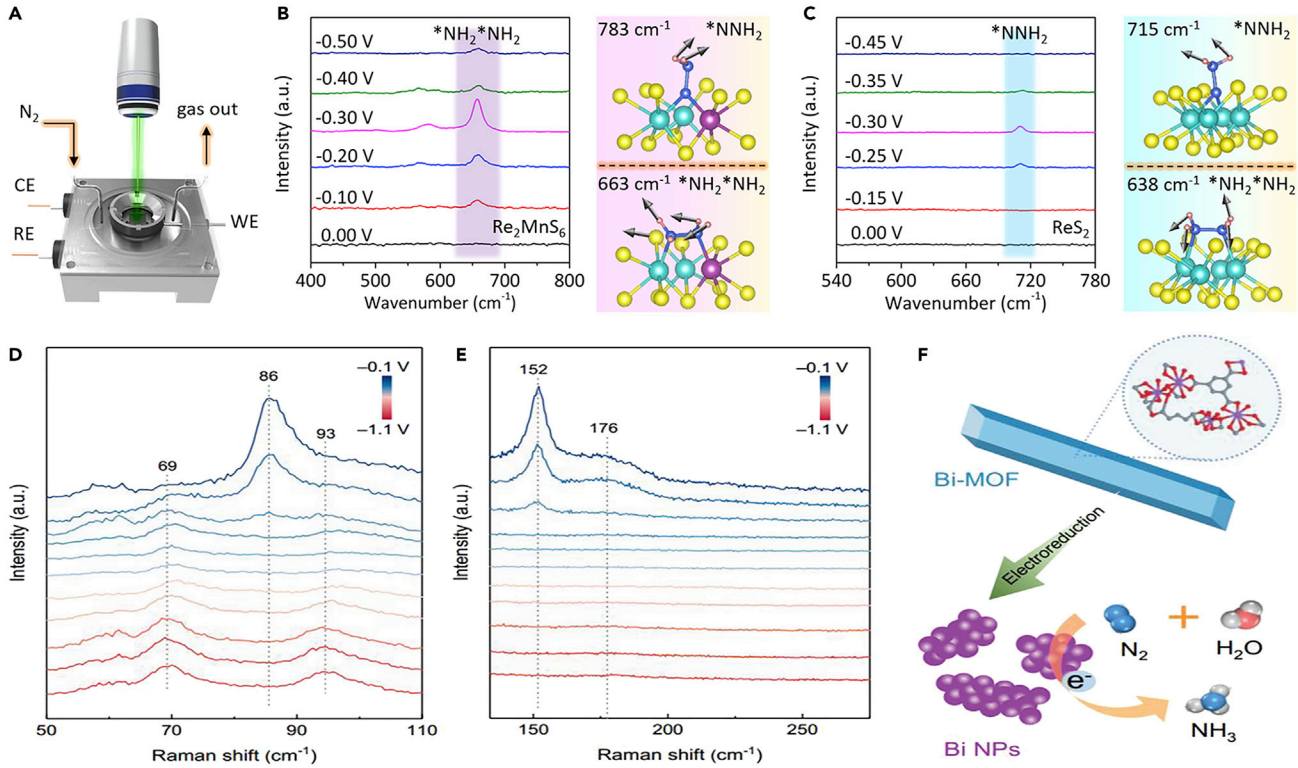

Figure 12. *In situ* Raman characterization for NRR

(A) Schematic illustration of the tailor-made electrolytic cell with a working electrode (WE), counter electrode (CE), and reference electrode (RE) for *in situ* test.

(B and C) *In situ* Raman spectra (left) and corresponding vibration modes (right) of Re_2MnS_6 (B) and ReS_2 (C) at different working potentials. Reprinted with permission from Fu et al.[89] Copyright 2020 American Chemical Society.

(D and E) *In situ* Raman spectra of the catalyst immersed into a thin electrolyte film with applied potential from −0.1 to −1.1 V (versus RHE).

(F) Schematic depiction for the *in situ* electroreduction-driven transformation from nanorods to nanoparticles. Reprinted with permission from Yao et al.[90] Copyright 2020 Wiley-VCH.

In situ *Raman spectroscopy.* *In situ* Raman spectroscopy has been employed to distinguish intermediates at molecular level and to further uncover the N_2 reduction pathway over Re_2MnS_6 (Figure 12A).[89] A pronounced Raman mode at 658 cm^{-1} was visualized for Re_2MnS_6 (Figure 12B), the signal of which increased with increasing overpotential and reached a maximum at −0.30 V. In contrast, only a weak Raman peak was discernible for ReS_2 which blue-shifted to 709 cm^{-1} (Figure 12C). The two peaks at 658 and 709 cm^{-1} could be assigned to N–H stretching of adsorbed $*NH_2*NH_2$ on the Re_2MnS_6 surface and $*NNH_2$ on the ReS_2 surface, respectively. Detection of the $*NH_2*NH_2$ species provided evidence that the NRR was driven by dual-metal sites following an associative alternating pathway. Identification of $*NNH_2$ rather than $*NH_2*NH_2$ suggested a distal pathway over single-metal ReS_2. A recent work by Qiao and coworkers showed that Bi metal organic framework (MOF) nanorods would undergo significant structural and chemical transformation to Bi nanoparticles (NPs) at potentials more negative than −0.5 V during electrochemical NRR, which was corroborated by *in situ* Raman spectroscopy (Figures 12D–12F).[90] The *in situ* reduced metallic Bi species were conjectured to be the dominant active sites for NRR. *In situ* Raman spectroscopy was used to confirm the formation of NH_3 during NRR on porous $PdH_{0.43}$ where it featured as a broad peak at 1,644.4 cm^{-1}.[91] The peak increased in intensity with applied overpotentials ascribed to accumulation of generated NH_3. Surprisingly, the potential where ammonia was

Please cite this article in press as: Shen et al., Electrochemical ammonia synthesis: mechanistic understanding and catalyst design, Chem (2021), https://doi.org/10.1016/j.chempr.2021.01.009

detectable in this work was as low as 50 mV (versus RHE) for $PdH_{0.43}$. Laser sources are required in Raman spectroscopy and thus may affect the formation and detection of NRR intermediates. To minimize such impact and avoid other optical responses (such as fluorescence) from catalysts, near-infrared laser is preferable.

In situ *DEMS.* The NRR process can be tracked with the aid of online differential electrochemical mass spectroscopy (DEMS) to monitor the volatile intermediates and products.[90] Such analysis provides important complementary direct information on electrocatalytic mechanisms. The co-existence of mass-to-charge ratio (m/z) signals at 27, 30, 31, and 33 indicates the formation of N_2H_4, while the signal at 15 can be attributed to either NH_3 or N_2H_4. Although the signals of NH_3 and water overlap (m/z = 17 and 16, respectively), the signal intensity of NH_3 varies with applied potential, which is not the case for water. Recently, Shao and co-workers[58] detected the signal of N_2H^+ (m/z = 29) with the H_2 signal (m/z = 2) at potentials below –0.3 V on Rh, whereas the signals of $N_2H_2^+$ (m/z = 30) and $N_2H_3^+$ (m/z = 31) were undetectable during the NRR. This provides evidence that a two-step reaction pathway may occur over Rh involving a two-electron transfer to form N_2H_2 followed by a subsequent decomposition in electrolyte (KOH) generating NH_3.

Operando *XAS.* *Operando* X-ray absorption spectroscopy (XAS) allows one to derive useful information on the density of unoccupied states, electronic structure, and bonding geometry of X-ray absorbing atoms. This technique has been used to characterize the surface species of VN in NRR.[82] The position and intensity of the vanadium K-edge white line at –0.1 and –0.2 V (versus RHE) were observed to be constant. A characteristic pre-edge peak at 5,468.4 eV was identified, indicating the presence of oxynitride species. Furthermore, the peak became gradually weakened with time during NRR, suggesting the conversion of $VN_{0.7}O_{0.45}$ to VN. The conversion rate increased with overpotentials, reaching 57.8% after 1 h at ≤ -0.2 V. These results support the hypothesis that the surface $VN_{0.7}O_{0.45}$ species was the active center in NRR, and the transformation of this phase to VN led to deactivation.

In situ *XPS.* By virtue of *in situ* X-ray photoelectron spectroscopy (XPS), the evolution of valence states of catalysts and adsorbed intermediate species can be probed. This helps to provide insight on possible active components and reaction pathways. Valov et al. demonstrated that N_2 can be electrochemically activated at the interface between an iridium micro-electrode and a (111)-orientated 9.5 mol % doped yttria stabilized zirconia (YSZ) singe crystal at 450°C and 10^{-5} Pa by means of *in situ* XPS (Figure 13).[92] A broad N 1s XPS peak between 397 and 398 eV was identified under cathodic voltages more negative than −1.5 V, which were deconvoluted into three components. The first peak with a binding energy (BE) at 397.2 eV was assigned to an N^{3-} ion and the other two components at BEs of 397.7 and 398.6 eV corresponded to (di)nitrogen ions in more positive oxidation states. The N 1s peak was reversible, indicating that the nitrogen species reduced at the electrode possibly accumulated only in the first top monolayers and easily desorbed from the surface when the voltage was switched off. Only at potentials more negative than −2.0 V, did reduction of the solid electrolyte take place, which could be confirmed by the appearance of new components of Zr 3d and Y 3d signals with a lower formal charge.

Advances of spectroelectrochemical cells also make it feasible for *in situ* time-resolved studies of structural changes of electrode surface accompanying the NRR by using surface X-ray scattering technique. In particular, the dynamic motions of microstructures such as kinks and steps can be tracked, providing insight into active reaction sites. To probe the microstructural and morphological changes of catalysts at

Please cite this article in press as: Shen et al., Electrochemical ammonia synthesis: mechanistic understanding and catalyst design, Chem (2021), https://doi.org/10.1016/j.chempr.2021.01.009

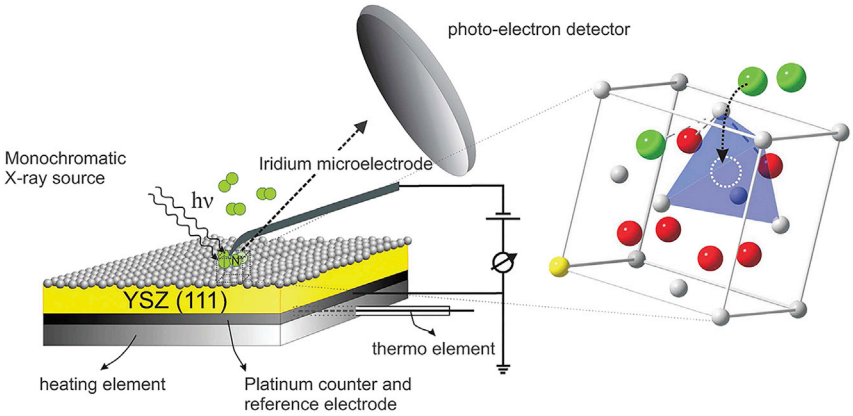

Figure 13. Scheme of the cell arrangement for electrochemical and XPS experiments
Reprinted with permission from Valov et al.[92] Copyright 2011 Royal Society of Chemistry.

the atomic scale, *in situ* electrochemical transmission electron microscopy (TEM) provides a unique possibility. We expect that this powerful emerging technique will be developed for use in NRR in the near future after some technical advances.

HETEROGENEOUS CATALYSTS FOR NRR

Experimentally explored catalysts

Materials that have been examined as catalysts for the NRR may be divided into two categories: (1) metal-containing electrocatalysts, such as pure metals, oxides, chalcogenides, nitrides, carbides, sulfides, phosphides, single-metal atoms, and metal-doped carbons; (2) metal-free electrocatalysts including carbon and its derivatives, boron and its compounds, polymeric carbon nitride, and black phosphorus. A summary of electrocatalytic studies on the reduction of N_2 with these materials is given in Table S1.

Metals, oxides, nitrides, carbides, chalcogenides, phosphides, bismuth oxyhalides, hybrids, single-atom, and cluster catalysts

The empty orbitals in metals can accept the lone-pair electrons of N_2 molecules to reduce the electron density of their HOMOs, and the separated electrons in metal atoms are donated into the antibonding π orbitals of adsorbed N_2 molecules to enhance the electron density of their LUMOs, thereby facilitating electron transfer to weaken the N≡N bond. Noble metals such as Ru,[24,57] were the first cathode demonstrated to activate N_2 for hydrogenation thanks to their strongly localized d-electrons, favorable electron affinity, and exceptional thermal and chemical stabilities. Afterward, a range of other precious metals such as Au, Pd, Ag, Pt, bimetallic AuAg, AuCo, Au/Ni, AuCu, AuBi, PtAu, PdCu, PdZn, PdRu, PdAg, PdNi, PdPb, RuCu, PtMo, Pt_3Fe, and noble-metal-free metals including Bi, Mo, Sn, Zn, Sb, Cu, bimetallic CoFe, MoCo, and Rh_2Sb have been reported to be active for NRR (Table S1). Thus far, an unprecedented FE reported for NH_3 formation via electrochemical NRR was achieved over couples of Ni and Au NPs (Au_6/Ni), approaching 67.8% at −0.14 V (versus RHE) in 0.05 M H_2SO_4 electrolytes,[93] although the maximum NH_3 production rate was not that high (7.4 μg h^{-1} $mg_{cat.}^{-1}$). However, the NH_3 yield rate needs to be further confirmed by using $^{15}N_2$ labeling via ^1H NMR. Despite exhibiting a lower FE of NH_3 (54.96%), bimetallic Au_1Cu_1 afforded a substantially higher NH_3 yield rate (154.91 μg h^{-1} $mg_{cat.}^{-1}$) at −0.2 V (versus RHE) in similar acidic electrolytes.[94] The outstanding performance was ascribed to the synergy of the Au and Cu components via modulating the electronic structure and further changing the binding affinity of adsorbed N atoms

Please cite this article in press as: Shen et al., Electrochemical ammonia synthesis: mechanistic understanding and catalyst design, Chem (2021), https://doi.org/10.1016/j.chempr.2021.01.009

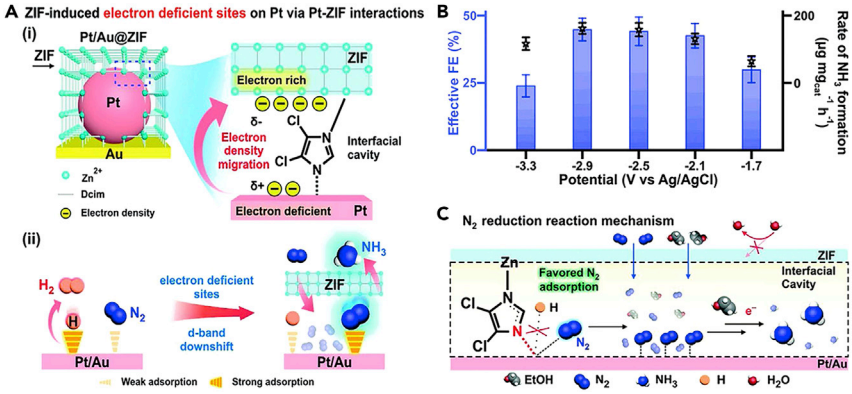

Figure 14. ZIF-modified Pt/Au for enhanced NRR

(A) The functions of ZIF: (1) inducing electron-deficient sites on Pt via electron density migration from Pt to ZIF and (2) lowering the d-band of Pt/Au.

(B) Evaluating NRR performance using 60 nm Pt/Au@ZIF at various electrochemical potentials.

(C) Proposed NRR mechanism at the Pt/Au@ZIF interfacial cavities.

Reprinted with permission from Sim et al.[96] Copyright 2019 Wiley-VCH.

on the catalyst. However, the purity of both N_2 and Ar used in this work was not provided. Additionally, the origin and quantity of NH_3 formed were not investigated by using $^{15}N_2$ isotope labeling. The NH_3 yield rate was further improved up to 228.85 $\pm$ 12.96 μg h^{-1} mg_{Rh}^{-1} on high-index facets of Rh_2Sb nanorods immobilized on commercial carbon at −0.45 V (versus RHE) in 0.5 M Na_2SO_4.[95] A zeolitic imidazole framework (ZIF)-modified Pt/Au (Figure 14A) was recently shown to drive NRR with an FE of >44.0% and an NH_3 yield rate of >161.0 μg h^{-1} $mg_{cat.}^{-1}$ at −2.9 V (versus RHE) using dry tetrahydrofuran (THF) solution containing lithium trifluoromethanesulfonate as an electrolyte (Figure 14B).[96] Coating with ZIF was supposed to lower the d-band position of the electrocatalyst leading to weakening of H adsorption, and concurrently creating electron-deficient sites to enhance catalyst-N_2 interaction. The hydrophobic ZIF layer also effectively suppressed HER. The metal-$N_{imidazole}$ interaction was further posited to be crucial for kinetic promotion of the NRR (Figure 14C). The good thing is that the authors subtracted all FE and NH_3 yield rate against control Ar experiments, which is important to avoid the risk of misinterpretation due to background interferences. However, the effect of contaminants in the supplied N_2 was not clarified. Furthermore, whether nitrogen in the catalytic system could have contributed to the formation of NH_3 was not confirmed by ^{15}N-isotope labeling.

Non-noble metals, especially transition metals, have attracted extensive interest because of their earth-abundance, low cost, and d-orbital electrons available for π back-donation to activate N_2. Apart from transition metals, the p-block metal Bi recently gained attention in NRR owing to its poor binding with H adatoms but strong interaction between the Bi 6p band and the N 2p orbitals.[17] Defect-rich Bi(110) nanoplates,[97] and Bi-MOF derived NPs[90] were all shown to catalyze NRR with an NH_3 FE exceeding 11.0% at –0.6 V (versus RHE) in either neutral or acidic solutions. Quasi-spherical Bi polyhedrons with an average size of 7.4 nm afforded an even unexpectedly high FE of up to 66.0% and an NH_3 yield rate of 200 mmol g^{-1} h^{-1} (0.052 mmol cm^{-2} h^{-1}) in H_2SO_4/K_2SO_4 solutions (pH 3.5).[17] Potassium cations were hypothesized to lower the free energy change for the PDS and regulate the proton diffusion process thereby promoting selective NRR. However, N_2 adsorption on the Bi surfaces was calculated to be thermodynamically unfavorable with an energy barrier of more than 2.7 eV.[22]

Please cite this article in press as: Shen et al., Electrochemical ammonia synthesis: mechanistic understanding and catalyst design, Chem (2021), https://doi.org/10.1016/j.chempr.2021.01.009

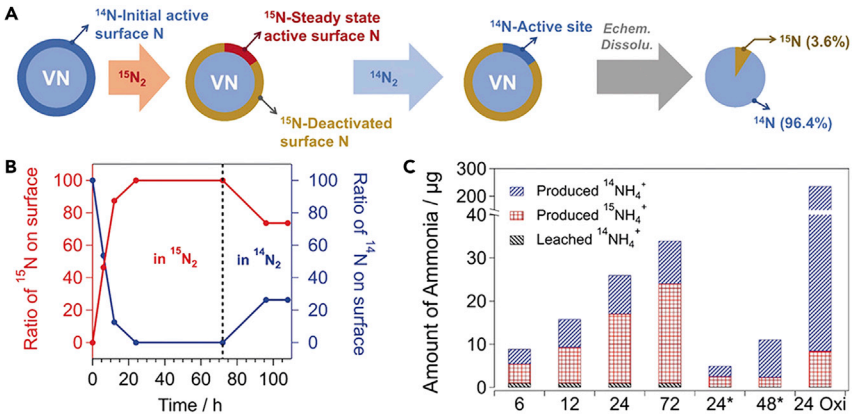

Figure 15. $V^{14}NO$ for electrocatalytic NRR

(A) Schematic illustration of the isotopic exchange experiments on $V^{14}NO$ to determine the density of initial and steady-state active sites in the NRR.

(B) Isotopic composition of active surface N sites as a function of time on stream in the NRR.

(C) Amounts of produced $^{14}NH_4^+$ and $^{15}NH_4^+$ during isotopic exchange experiments at various time points during the NRR.

Reprinted with permission from Yang et al.[32] Copyright 2019 Wiley-VCH.

Metal oxides comprising Ti^{4+}, Nb^{x+} (NbO_2, Nb_2O_5), Fe^{x+} (Fe_2O_3, Fe_3O_4), Co^{x+} (Co_3O_4), Mn^{x+} (MnO, MnO_2, Mn_3O_4), Mo^{3+}, W^{6+}, Bi^{3+}, Ta^{5+}, Sn^{4+}, Cr^{3+}, and Ce^{x+}, V^{4+}, Zr^{4+}, and La^{4+} have been evaluated for NRR (Table S1). Among these oxides, oxygen-vacancy-rich TiO_2 NPs *in situ* grown on conductive $Ti_3C_2T_x$ nanosheets exhibited an impressive NH_3 yield of 32.17 μg h^{-1} $mg_{cat.}^{-1}$ at −0.55 V (versus RHE) and an FE of 16.1% at −0.45 V (versus RHE) in 0.1 M HCl.[98] Despite this promising efficiency in NRR, the purity of N_2 employed in this work was not reported. In addition, ^{15}N-isotope labeling was not conducted to verify the actual reduction of N_2 to yield NH_3. Nb^{4+} with one 4d electron was demonstrated to be more prone to back-donation than Nb^{5+} without 4d electrons.[99] Hence, superior NRR activity was attained over NbO_2 with an NH_3 FE approaching 32.0% at −0.60 V (versus RHE) in 0.05 M H_2SO_4 solution. It is worth noting that reduction of metal oxides and removal of surface oxygen vacancies during long-term NRR may be an issue that merits attention.

Transition metal nitrides, such as VN, MoN, W_2N_3, LaN, ZrN, NbN, and CrN, have been reported to catalyze electrochemical ammonia formation through the Mars-van Krevelen mechanism (Table S1).[100] Only those surface N sites in oxygen-modified VN catalyst involved in the NRR were claimed to be active at the steady state (Figure 15A). The fraction of active sites could be quantified using an isotopic exchange method (Figures 15B and 15C).[32] Activation of adsorbed N_2 on the N vacancy of oxygen-modified VN (VNO) to adsorbed N_2H was predicted to be the rate-limiting step in the NRR. However, a recent work from Qiao et al. showed that N-vacancy engineered 2D W_2N_3 nanosheets followed a distal mechanism, and the last step of releasing the second NH_3 was the PDS.[101] The nitrogen vacancies lowered the thermodynamic limiting potential and boosted the NRR reaction with an average NH_3 formation rate of 11.66 ± 0.98 μg h^{-1} $mg_{cat.}^{-1}$ (3.80 ± 0.32 × 10^{-11} mol cm^{-2} s^{-1}) and FE of 11.67% ± 0.93% at −0.2 V (versus RHE) in 0.1 M KOH solution. Only $^{15}NH_4$ was detected in NMR when using $^{15}N_2$ as a supplied gas, ruling out the possibility that the NH_3 was generated from the decomposition of W_2N_3 or other contaminants. However, quantitative isotope-labeling experiments were not presented. Note that the chemical stability of nitrides during NRR remains

Please cite this article in press as: Shen et al., Electrochemical ammonia synthesis: mechanistic understanding and catalyst design, Chem (2021), https://doi.org/10.1016/j.chempr.2021.01.009

an issue. For example, Mo_2N was observed to undergo rapid decomposition in aqueous electrolytes and exhibited marginal catalytic activity for the NRR.[102]

2D d^2-d^4 M_3C_2 MXenes without terminal groups were shown to exhibit good activity toward the NRR.[103] M_2C was inferred to be more effective due to its least number of atomic layers relative to M_3C_2 and M_4C_3 MXenes. In particular, $4d^4$-Mo_2C was calculated to possess the lowest free energy barrier among the synthesized M_2C MXenes.[104] Other metal carbides such as MoC_6, MoC, Cr_3C_2, Fe_3C, and V_8C_7 were also demonstrated to display reasonable activity for NRR at moderate overpotentials (Table S1). It was predicted that introducing carbon vacancies to increase the ratio of surface metal to carbon atoms could reduce the adsorption of hydrogen atoms and improve the adsorption capacity of nitrogen molecules.[105] Further integration of carbon vacancies and mesoporous structure brings about more coordinatively unsaturated sites to adsorb and activate N_2 molecules over vanadium carbide (V_8C_7), promoting the NRR to NH_3 with an FE of 18.3% and an NH_3 yield rate of 23.2 $\mu g\ h^{-1}\ mg_{cat.}^{-1}$ at −0.1 V (versus RHE) in 0.1 M HCl.[106]

Perhaps inspired by nature's nitrogenase enzymes, MoS_2 has sparked research interest for NRR.[84] The Mo-edge was suggested to have a relatively low barrier in the PDS.[107] Other sulfides, such as Fe_3S_4, FeS_2, NbS_2, ReS_2, Sb_2S_3, VS_2, and Re_2MnS_6, have also been reported to catalyze electrochemical ammonia formation. Notably, the Li^+ interactions with S-edge sites of MoS_2 were found to suppress HER by reducing H* adsorption free energy while increasing N_2 adsorption free energy, thus, decreasing the activation energy barrier of the NRR controlling step.[108] An NH_3 yield rate of 43.4 $\mu g\ h^{-1}\ mg_{MoS2}^{-1}$ and FE of 9.81% were observed in the presence of strong Li–S interactions, more than eight and eighteen times compared with the same electrocatalyst in the absence of Li–S interactions, respectively. FeS_2 can prohibit HER. Further, due to possibility of FeS_2 inhibiting the HER, doping of FeS_2 with Mo(IV) ions could favor adsorption and activation of N_2, permitting selective NRR to NH_3 at mild overpotentials.[109] Additionally, selenides of $ReSe_2$[110] and $NbSe_2$[111] have been explored for electrocatalytic NRR. In particular, selenium vacancy-rich $ReSe_2$ nanofibers sandwiched by hydrophobic and porous carbonized bacterial cellulose layers could effectively drive NRR with an FE of 42.5% and an NH_3 yield rate of 28.3 $\mu g\ h^{-1}\ cm^{-2}$ at −0.25 V (versus RHE) in 0.1 M Na_2SO_4 electrolytes.[110] However, $^{15}N_2$ isotopic labeling to quantify the amount of NH_3 was not provided.

The negatively charged phosphorus can induce electron cloud density deviation of metals and modulate the surface charge state of metal phosphides, thereby improving their intrinsic catalytic properties. Indeed, phosphides, such as MoP, PdP_2, Ru_2P, RhP_x, FeP, FeP_2, Ni_2P, CoP, CoP_3, and Cu_3P, have been demonstrated to be capable of catalyzing ambient electrochemical NH_3 synthesis (Table S1).

Bismuth oxyhalides (BiOX, X = Cl, Br, I) possess a unique, layered structure, tunable energy band gap, and strong light response to boost solar energy conversion, showing potential in photocatalysis.[112] The interlayer can induce a built-in field to separate the charges and make the electrons be assembled in the Bi-O layer for activating N_2 molecules. The edge of BiOX is constructed by O atoms and oxygen vacancies can easily form at the surface of BiOX under mild conditions. However, application of BiOX in electrocatalytic NRR has been rarely reported. Only $Bi_4O_5I_2$ modified with oxygen vacancies and hydroxyl groups on the surface was demonstrated to electrocatalyze the conversion of N_2 to NH_3 with a prominent FE of 32.4%, outperforming most *p*-block-element-based catalysts.[113]

Please cite this article in press as: Shen et al., Electrochemical ammonia synthesis: mechanistic understanding and catalyst design, Chem (2021), https://doi.org/10.1016/j.chempr.2021.01.009

Increasing effort is concentrated on creation of hybrids to promote nitrogen fixation by taking advantage of a synergistic effect between different components. Amorphous $Bi_4V_2O_{11}/CeO_2$[114] and phosphorus-doped carbon/Sb/$SbPO_4$[115] both substantially exceeded respective individual counterparts in NRR with the latter exhibiting an impressive NH_3 FE over 30.0% in either acidic or neutral electrolytes at low overpotentials. 3D graphdiyne–cobalt nitride (GDY/Co_2N) has been applied for NRR.[116] It is noteworthy that a respectable NH_3 yield rate (219.72 μg h^{-1} $mg_{cat.}^{-1}$) and FE (58.6%) were achieved at atmospheric pressure and room temperature in acidic conditions. However, despite this high efficiency, the stability of Co_2N during prolonged electrolysis needs to be resolved. The NH_3 yield rate needs to be further confirmed by quantitative $^{15}N_2$ labeling measurements.

The size of a metal catalyst is a key factor in determining the catalytic performance since the specific activity per metal atom increases with downsizing metal particle. The ultimate specific activity can be achieved by using single-atom catalyst (SAC), which contains atomically dispersed metal atoms in support materials. In addition to ultimate specific activity, SAC shows distinct catalytic activity due to its size effects, such as low-coordination environment of metal center, quantum size effects, and metal-support effects. Many SACs, such as N-doped carbon or metal-oxide-supported single-metal atoms, have been reported in literature for various applications. In recent years, applications of SACs for NRR also have notably increased. In 2018, Choi et al. screened 120 N-doped or defective graphene-based SACs for NRR by DFT calculations and suggested several promising SACs including Ti@N_4 and V@N_4.[117] The key finding of this work was that SACs can suppress HER during NRR compared with metal surfaces owing to the lack of atomic ensemble in the active sites. These results indicate that SACs can be a promising platform for increasing faradic efficiency of NRR. Several SACs have indeed been experimentally proven to be very active for NRR in the literature (Table S1). For example, Sun and coworkers prepared Ru single atoms embedded at ZrO_2 and N-doped carbon (Ru@ZrO_2/NC), and the Ru@ZrO_2/NC exhibited high NH_3 yield rate (3.665 mg h^{-1} mg_{Ru}^{-1}) and FE (21.0%) at −0.21 V (versus RHE) (Figure 16) in 0.1 M HCl solution.[118] These data need to be further confirmed by quantitative NMR measurements. DFT calculations revealed that Ru single atoms anchored at surface O-vacancies in ZrO_2 and N-doped graphene showed low free energy for NRR and improved *N_2/*H adsorption selectivity. In addition to Ru SAC, SACs consisting of Mo, Fe, Y, and Pt have also been experimentally demonstrated to be efficient for NRR (Table S1). Xin and coworkers demonstrated that atomically dispersed Mo at N-doped porous carbon (SA-Mo/NPC) could catalyze NRR with high efficiency.[61] The SA-Mo/NPC showed improved NH_3 yield rate (34.0 μg h^{-1} $mg_{cat.}^{-1}$) and FE (14.6%) at room temperature. Various types of Fe single atoms embedded at N-doped carbon have displayed improved catalytic activity toward NRR.[119,120] Zheng and coworkers revealed that Fe-N/C-carbon nanotube (Fe-N/C-CNT) containing Fe-N_3 active sites achieved 34.83 μg h^{-1} $mg_{cat.}^{-1}$ of NH_3 yield rate and 9.28% of FE in 0.1 M KOH solutions.[120] Further DFT calculations established that Fe–N_3 sites could strongly bind N_2 and reduce N_2 to NH_3 with 0.84 eV of free energy. FeN_4 moiety embedded carbon catalysts have also been reported for NRR in both neutral and alkaline media.[121] A coordination of Fe–(O–C_2)$_4$ as active sites supported on nitrogen-free lignocellulose-derived carbon provided even higher NRR performance.[122] The NH_3 production rate reached 307.7 μg h^{-1} $mg_{cat.}^{-1}$ with an FE of 51.0% at −0.1 V (versus RHE) over Fe–(O–C_2)$_4$ immobilized on a glassy carbon electrode in 0.1 M KOH electrolytes. Li and coworkers demonstrated that Au single-atom-embedded C_3N_4 (Au_1/C_3N_4) exhibited outstanding NH_3 formation (1,305 μg h^{-1} mg_{Au}^{-1}) and FE (11.1%) at −0.1 V (versus RHE).[123] Theoretical calculations suggested that Au_1/C_3N_4

Please cite this article in press as: Shen et al., Electrochemical ammonia synthesis: mechanistic understanding and catalyst design, Chem (2021), https://doi.org/10.1016/j.chempr.2021.01.009

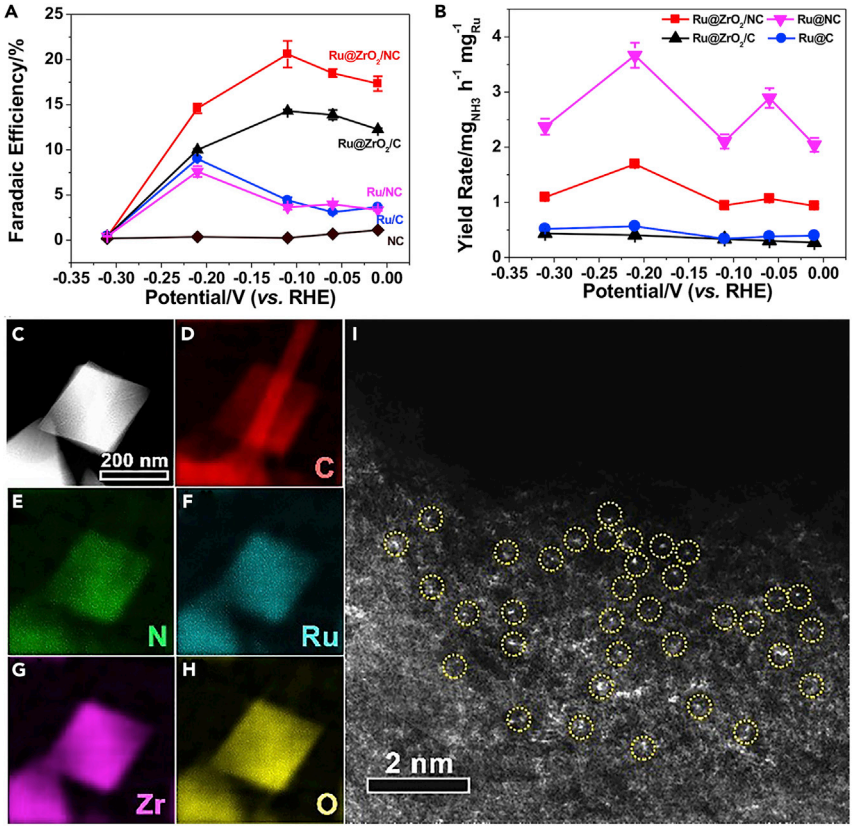

Figure 16. NRR evaluation and structure characterization of $Ru@ZrO_2/NC$

(A and B) (A) FEs and (B) yield rates of NH_3 over $Ru@ZrO_2/NC$, $Ru@ZrO_2/C$, Ru/NC, RU/C, and NC at various applied potentials.

(C) Low-magnification HAADF-STEM image of $Ru@ZrO_2/NC$ after six cycle tests of NRR.

(D–H) EDS maps of C (D), N (E), Ru (F), Zr (G), and O (H) atoms in the region shown in (C), respectively.

(I) HAADF-STEM image showing the presence of single Ru sites annotated with yellow dotted circles.

Reprinted with permission from Tao et al.[118] Copyright 2019 Elsevier.

required lower free energy for NRR than Au(211) surface. However, whether the nitrogen in C_3N_4 had contributed to the evolution of NH_3 remained unclear. The formation of NH_3 from NRR needs to be explored by $^{15}N_2$-isotope labeling qualitatively and quantitatively.

Metal-free carbon and its derivatives, boron and its compounds, polymeric carbon nitride, black phosphorus, and red phosphorus

A number of carbon materials, such as heteroatom (N, S, F, Te, or Se)-doped carbon, P-doped carbon nanotube, Cl-doped graphdiyne, defective graphene, (reduced) graphene oxide, heteroatom (P, N, B, S, and F)-doped graphene, B-doped nanostructured diamond, B- and N-codoped carbon, and N, P-codoped carbon, were shown to exhibit comparable and even superior NRR activity than many metal-based electrocatalysts (Table S1). A nanohybrid of S dots and graphene was also revealed to be active for N_2 fixation.[124] Strikingly, an NH_3 production rate of 19.1 $\mu g\ h^{-1}\ cm^{-2}$ and FE as high as 21.2% were attained over boron-doped nanostructured diamond/Ti electrodes in 0.05 M H_2SO_4 solution containing 0.2 M Li_2SO_4.[125] Of interest is that the electrode retained stability for over 8 days without obvious decay in activity.

Please cite this article in press as: Shen et al., Electrochemical ammonia synthesis: mechanistic understanding and catalyst design, Chem (2021), https://doi.org/10.1016/j.chempr.2021.01.009

Boron doping was supposed to induce NRR active sites in diamond lattices and buildup of surface charges, leading to enhanced catalytic performance.

In addition to carbon-based materials, electron-deficient boron[126] and its compounds such as boron nitride, C-doped boron nitride, boron carbide, and boron phosphide have emerged as appealing metal-free catalysts for the NRR. A "π back-donation" process was proposed on boron (borylene) with empty sp^2 orbital and occupied p orbital for effective N_2 activation.[127] Compared with conventional transition metal surfaces that were shown to require up to 1 eV for NRR by DFT calculations, the (021) and (104) surfaces of boron nanosheets demand much less free energy to drive the NRR (0.21 and 0.39 eV, respectively).[126] Indeed, exposed icosahedron boron in the (021) and (104) surfaces was observed to effectively catalyze the NRR.

Polymeric carbon nitride (PCN) provides plentiful and homogeneously distributed nitrogen vacancies (NVs).[128] By heating in an atmosphere of argon, the contents of NVs in PCN obtained by polycondensation of melamine were readily tuned. This allows for modulation of the π-electron delocalization in the conjugated system, resulting in strong N_2 activation.[128]

Zigzag and diff-zigzag edges of exfoliated black phosphorous (BP) nanosheets were recently shown to be active centers for N_2 adsorption and N≡N triple bond activation, which enable NRR via an alternating hydrogenation pathway, delivering a high NH_3 production rate of 31.37 μg h^{-1} $mg_{cat.}^{-1}$ albeit with a moderate FE of 5.07% at −0.6 V (versus RHE) in 0.1 M HCl solution.[129] The FE for NH_3 formation was stated to be improved by N and O doping of BP surfaces to impart hydrophobicity and hinder the competitive HER.[130] However, BP suffers from oxidative degradation especially in the presence of water,[131] thus, limiting its practical application in NRR. Nanoribbons of red phosphorus, a more stable allotrope of phosphorus, were shown to facilitate NRR, providing an FE of 9.4% and an NH_3 yield of 15.4 μg h^{-1} $mg_{cat.}^{-1}$ at –0.5 V (versus RHE) in 0.1 M Na_2SO_4.[132] The NRR performance was credited to the apparent anisotropy and the quasi-one dimensional morphology of nanoribbons, endowing red phosphorus with efficient charge transfer and abundant exposed-edge sites.

Potential alternative catalysts for N_2 conversion

To date, various types of catalysts have been suggested for NRR. Here, we briefly introduce promising catalysts for NRR suggested in the literatures, such as boron-based catalysts and metal sulfides, but not experimentally realized. Previous studies have shown that boron can reduce N_2 both in homogeneous and heterogeneous catalysts. It has been shown that boron atom can activate N_2 with π back-donation which is the mechanism of N_2 activation on transition metals (Figure 17A).[127] Experiments combined with DFT calculations demonstrate that boron 2D nanosheets can facilitate NRR with low overpotential.[126] Also, boron-doped or boron-based catalysts, such as B-doped graphene[36] and B_4C,[133] have been proven efficient for NRR experimentally. In addition to these catalysts, single-boron-doped catalysts and transition metal borides have been suggested for NRR by DFT calculations (Figure 17B). Liu et al.[134] explored boron single site doped in various 2D materials (graphene, BN, BS, BP, s-triazine, tri-s-triazine, *h*-MoS_2, and *t*-MoS_2) and showed that negatively charged boron sites are promising for low overpotential and high selectivity for NRR. Among various boron sites, boron-doped graphene and *h*-MoS_2 were identified as promising boron sites for NRR. In addition to doped boron sites, transition metal borides (MB_x) have been suggested for NRR.[135] Surface boron atoms in

Please cite this article in press as: Shen et al., Electrochemical ammonia synthesis: mechanistic understanding and catalyst design, Chem (2021), https://doi.org/10.1016/j.chempr.2021.01.009

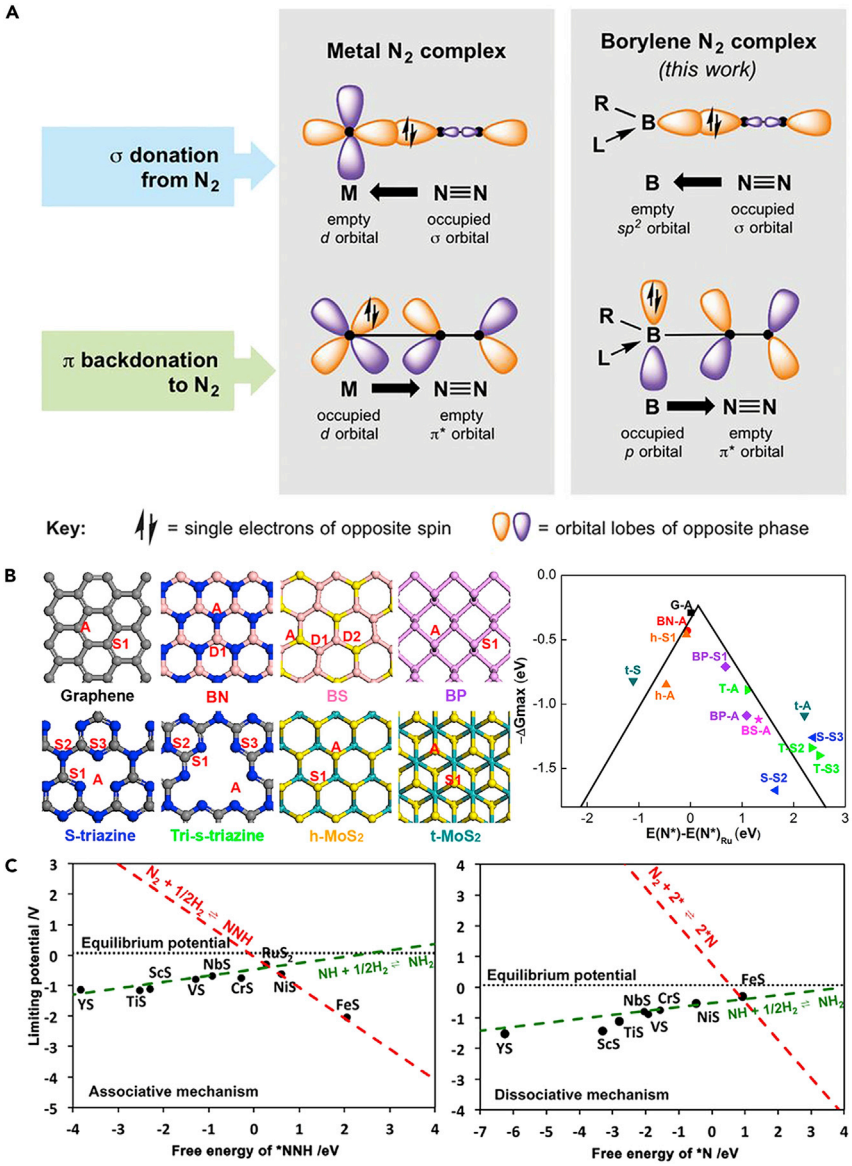

Figure 17. Volcano plot for NRR activity on transition metal sulfides

(A) Simplified schematic of the end-on bound transition metal-N_2 complexes (left) and borylene-N_2 complex (right). Reprinted with permission from Légaré et al.[127] Copyright 2018 American Association for the Advancement of Science.

(B) Different boron doping sites in various 2D materials and maximum free energy required for NRR. Reprinted with permission from Liu et al.[134] Copyright 2019 American Chemical Society.

(C) Volcano plot for limiting potential of NRR on various transition metal sulfides via associative mechanism (left) and dissociative mechanism (right). Reprinted with permission from Abghoui et al.[136] Copyright 2019 Wiley-VCH.

Mo_2B, Fe_2B, and Co_2B are suggested for NRR with (−0.75 ~ −0.84 V versus RHE) being the optimal limiting potential.[135]

As described above, ammonia in nature is synthesized at ambient conditions by enzymes whose active site, for example, is a transition-metal sulfide cluster ($MoFe_7S_9N$). Skúlason and coworkers studied the possibility of catalyzing ammonia formation on the surface of transition metal sulfides that, owing to presence of the

Please cite this article in press as: Shen et al., Electrochemical ammonia synthesis: mechanistic understanding and catalyst design, Chem (2021), https://doi.org/10.1016/j.chempr.2021.01.009

transition metal and sulfur atoms, offer some similarity to the structure of active sites of the enzyme.[136] NRR on various low-index surfaces of transition metal sulfides such as rocksalt(100), NiAs-type(111), pyrite(100), and pyrite(111) via associative and dissociative mechanisms were investigated. They obtained a volcano plot for NRR activity on transition metal sulfides (Figure 17C). RuS_2 was predicted to have low overpotential (0.3 V), and the other promising candidates (CrS, NbS, VS, and TiS) showed 0.7~1.1 V of overpotential.

ML models for NRR

Recently, machine learning (ML) approaches have become popular and proven useful in the design of catalysts as the advancement in computational power led to big data and development in ML methods.[137] In the NRR field, ML has been used to screen promising catalysts[138,139] and optimize morphology of catalysts.[140] Here, we briefly discuss several ML models that were specifically used to develop NRR catalysts, and refer readers to the recent comprehensive review papers for general aspects of ML in catalysis.[137,141]

Kim et al.[138] screened various transition metal alloys for NRR by developing a slab graph convolutional neural network (SGCNN), which is an extended model of the existing crystal graph CNN (CGCNN).[142] The CGCNN has proven its accuracy in predicting bulk properties but not yet tested for surface-related properties at that time. To incorporate surface effects, surface graph (S_1 or S_2) and bulk graph (B) are constructed (Figure 18A). Total 3,040 binding energies, which consist of 465 catalysts with different crystal spaces (*fcc*, *bcc*, *hcp*, $L1_0$, B2, and core-shell), and 5 adsorbate types (H, N_2, N_2H, NH, and NH_2) and sites were used for the SGCNN training. For input features, a combination of 5 low-level input features (group number [GR], Pauling-scale electronegativity [EN], atomic volume [AV], electron affinity [EA], and atomic weight [AW]) was used since it shows minimum mean absolute error (MAE) of 0.23 eV (Figure 18B). The SGCNN model trained by 465 catalysts was used for screening 870 candidates consisting of (111) facet of A_3B structure (Figure 18C). Among 870 candidates, 10 catalysts (e.g., V_3Ir, Tc_3Hf, V_3Ni, and Tc_3Ta) were included in the screening criteria (Figure 18D).

Various structures of single transition-metal-atom-embedded B-doped graphene were explored for NRR by using machine learning-based methods (Figure 18E).[139] The Coulomb matrix was used as a descriptor for representing atomic geometric structures. The eligible catalysts which could facilitate $*N_2$, $*N_2H$, and $*NH_3$ formation were classified by using the deep neural network (DNN). The reaction free energies were predicted by ML model trained by the light gradient boosting machine (LGBM) model (RMSE = 0.11 eV). The most important feature was the coordination number of the metal and the number of hydrogen atoms for the DNN and LGBM models, respectively. Promising catalysts, such as CrB_3C_1 (U_L = −0.29 V), HfB_1C_2 (U_L = −0.42 V), and TcB_3C_1 (U_L = −0.44 V), were finally screened.

ML accelerates not only the catalysts screening process but also optimization of the material morphology. Liu and coworkers explored how the electrode's morphology contributes to NRR activity and provided the means to quickly optimize wire-array morphology.[140] About 200,000 finite element methods (FEM)[143] simulations were conducted to yield values of total current density (i_{total}) and FE of NRR as a function of feature variable vector x, which is described in Figure 18F. The variable vector x consists of physical features of morphologies such as diameter (*d*), length (*l*), and array periodicity in a square lattice (*p*) and kinetics information such as exchange current density of the Volmer step of HER ($i_{1,0,HER}$), the Heyrovsky step of HER ($i_{2,0,HER}$),

Please cite this article in press as: Shen et al., Electrochemical ammonia synthesis: mechanistic understanding and catalyst design, Chem (2021), https://doi.org/10.1016/j.chempr.2021.01.009

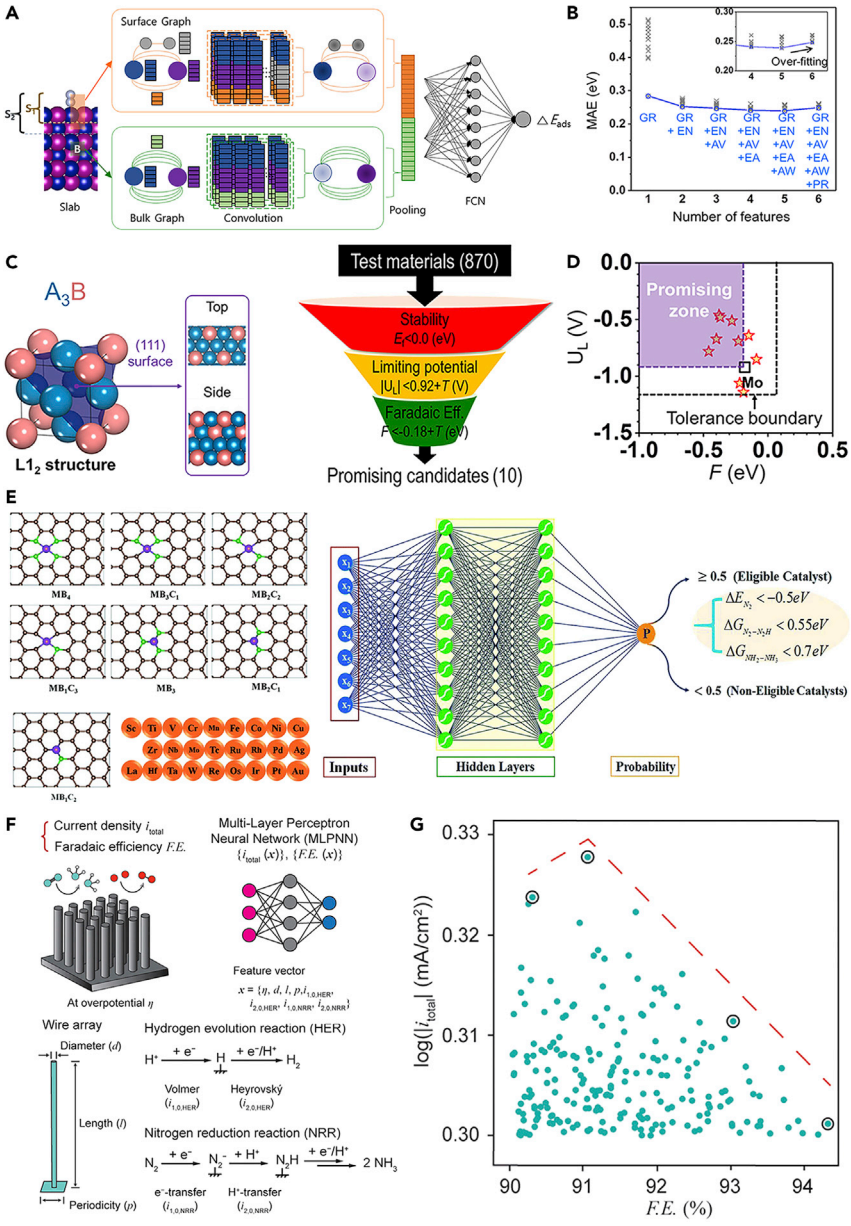

Figure 18. Studies of ML on screening promising NRR catalysts and optimizing morphologies of catalysts

(A) Schematic of the main architecture of the SGCNN model. B and S_1 (or S_2) represent the bulk graph and surface graph with the top layer (or top two layers), respectively.

(B) MAE values as a function of various feature combinations.

(C) Bulk and (111) surface of the $L1_2$ ordered phase of A_3B (left) and screening process to search for stable and efficient NRR catalysts, which potentially outperform Mo(110) (right).

(D) U_L and F values predicted by the SGCNN model for 10 screened promising catalysts. Reprinted with permission from Kim et al.[138] Copyright 2020 American Chemical Society.

(E) Structure of B-doped graphene with single-metal atoms considered for screening. Reprinted with permission from Zafari et al.[139] Copyright 2020 Royal Society of Chemistry.

(F) ANN (10 neurons in each hidden layer) architecture and criteria for eligible NRR catalysts.

(G) Selection of hypothetical promising catalysts for NRR among over 4,000,000 scenarios generated by trained MLPNNs. Reprinted with permission from Hoar et al.[140] Copyright 2020 American Chemical Society.

Please cite this article in press as: Shen et al., Electrochemical ammonia synthesis: mechanistic understanding and catalyst design, Chem (2021), https://doi.org/10.1016/j.chempr.2021.01.009

the first electron transfer step of NRR ($i_{1,0,NRR}$) and the first proton transfer step of NRR ($i_{2,0,NRR}$), and overpotential (η). The two feed-forward[144] multilayer perceptron neural networks (MLPNNs) were used for training the FEM datasets. The MLPNN prediction shows an accuracy of 2.810%^{2} and 6.76 × 10^{-4} mA^2/cm^4 of mean squared error (MSE) for FE of NRR and total current density, respectively. In total, 4,000,000 scenarios were generated by trained MLPNNs and over 200 scenarios, which meet $|i_{total}| > 2.0$ mA/cm^2 and FE > 90.0% were shown in Figure 18G. Top 4 scenarios which are denoted in Figure 18G, converge to a similar range of parameter values, $\eta \approx -0.7$ V versus RHE, $d \approx 8$ μm, $l \approx 40$ μm, $p \approx 10$ μm, $i_{1,0,NRR} \approx 10^{-3}$, $i_{2,0,NRR} \approx 10^{-3}$, $i_{1,0,HER} \approx 10^{-8}$, and $i_{2,0,HER} \approx 10^{-8}$ mA/cm^2, corresponding to the reasonable kinetic reactivity and geometry for optimal NRR catalyst.

All of these ML approaches efficiently predict NRR activity. For example, 870 catalysts were screened by the SGCNN model trained by data of 465 catalysts (53% of screening data)[138] and 4,000,000 scenarios were investigated by using the MLPNNs trained by 200,000 FEM data (5%).[144] In other words, noticeable amounts of potentially unnecessary simulations (from 47% to 95%) were eliminated.

Challenges and outlooks of theoretical approaches for understanding NRR

As aforementioned, theoretical studies have played an important role in elucidating the reaction mechanism of NRR, understanding the NRR activity trend, and suggesting promising catalysts (Figures 9, 10, and 17). Furthermore, ML has been emerged as a sufficient method for accelerating the development NRR catalysts (Figure 18). However, current result of DFT calculations sometimes does not describe the experimental results. The most dominant reaction during NRR is the HER; however, the competition between the NRR and HER has not been well discussed theoretically. Here, we discuss the challenges and outlooks of theoretical approaches for further understanding of NRR.

One of the most significant problems in current DFT calculations is that the reported theoretical limiting potentials disagree with the experimental electrode potential at maximum NRR activity in most cases. The theoretical limiting potentials (U_L), where the overall electrochemical reaction becomes thermodynamically exothermic, on various *fcc* transition metal surfaces are at least –1 V (versus RHE) theoretically (Figure 10). However, maximum NRR activities are often observed at –0.05 ~ –0.60 V (versus RHE), highly more positive than theoretical U_L (Table S1). For example, maximum NH_3 yield rates were obtained at –0.1 V (versus RHE) on Ru nanoparticles[145] and –0.2 V (versus RHE) on Au nanorods,[146] while their theoretical U_L are around at –1.0 V (versus RHE) and –3.0 V (versus RHE), respectively. The origin for such large discrepancy has not been clearly clarified; however, a possible reason has been suggested, namely dominant H coverages at negative electrode potentials. The H adsorption via * + (H^+ + e^-) → *H (due to its electrochemical nature of the reaction) increases faster than the N_2 adsorption (* + N_2 → *N_2, non-electrochemical reaction) with more negative electrode potential.[27] Thus, dominant H coverages at negative electrode potentials block the N_2 adsorption after which NRR activity decreases although the electrochemical reduction rates of NRR themselves might increase with more negative potential. However, this possibility has not been quantitatively established or validated since the *in situ* measurements of N_2 and H coverage during NRR is still highly challenging. Thus, the *in situ* investigation, either experimentally or theoretically, of N_2 versus H coverage changes and NRR activity with electrode potential would provide invaluable insights to fully understand the origin of the decreasing NRR activity with electrode potential.

Please cite this article in press as: Shen et al., Electrochemical ammonia synthesis: mechanistic understanding and catalyst design, Chem (2021), https://doi.org/10.1016/j.chempr.2021.01.009

Most of theoretical studies on NRR neglected the kinetics and focused on the thermodynamic reaction energies.[147] Only a few studies considered activation energy during the proton-electron transfer reactions in NRR.[148,149] To fully understand the NRR, theoretical studies should consider the potential-dependent competition between NRR and HER including the N_2 versus H binding and kinetics.

Electrolytes as well as the active sites are important in enhancing the NRR activity. By tuning the electrolytes (e.g., ILs and non-aqueous electrolytes), enhancement in N_2 solubility and FE of NRR can be achieved.[15,74] Several theoretical studies on the effect of electrolyte have been reported. For example, Zhang et al. demonstrated that HER can be suppressed during NRR by utilizing a non-aqueous bulky proton donor[150] and Ortuño et al. showed stabilization of reaction intermediates of NRR by ILs.[76] We expect that further theoretical studies on electrolytes at atomic level will be helpful for designing electrolytes.

So far, ML techniques have been rarely used in the NRR field, while they have been widely utilized for various chemical reactions. We believe that ML approaches developed in other catalytic reactions would be also helpful in investigating the NRR. For example, Ulissi and coworkers identified the most likely reaction pathways of syngas on Rh(111) among more than 2,000 potential pathways by using the Gaussian process with group additivity descriptors.[151] Similar ML approaches will be applied for investigating the reaction mechanism and reaction kinetics of NRR. While various catalysts have been theoretically suggested, synthesizability as well as NRR activity is also quite important. Recently, Jang et al. proposed data-driven metric of the crystal-likeness score, which estimates the synthesizability of crystalline material.[152] This ML approach will be employed to estimate the synthesizability of proposed catalysts before its experimental validation.

STRATEGIES FOR IMPROVING N_2 ELECTROCATALYTIC ACTIVITY

Strategies to promote the electrocatalytic performance of materials for NRR should take into account the following: (1) enhancing adsorption and activation of N_2 at low overpotentials, (2) suppressing side reactions such as HER, and (3) increasing long-term stability, as illustrated in Figure 19. This section focuses on basic information and understanding for improving the activity.

Surface engineering

Surface modification

Surface functionalization with chemical moieties offers an effective way to tune electrocatalysis through modulating the electronic properties of catalyst surfaces and the resultant adsorption energies of reaction intermediates.[12] Surface selenation was recently demonstrated to greatly boost NRR performance (Figure 20).[153] An upshift of the d-band center was observed for surface selenated Rh nanocrystals (NCs), which was hypothesized to strengthen N_2 adsorption. The Se sites may also play a role in promoting electron transfer between N-species and nearby Rh-sites. Alternatively, introducing –O or –OH species was shown to facilitate improved NRR. Oxygen functional groups in oxidized carbon nanotubes or graphene oxide alter the electron distribution in the surrounding carbon atoms, resulting in optimized binding strengths of N_2 and NRR reaction intermediates on carbon to enhance NRR.[154] Surface hydroxyl modification of Ti_3C_2 MXene either by alkalization intercalation and agitation[155] or via ethylene glycol solvothermal treatment[156] was manifested to increase the electronic density of states at the Fermi level and lower resistance, as compared with oxygen termination and original Ti_3C_2. This favors electron transfer to the 2π orbitals of N_2 and promotes its chemisorption and activation. By contrast,

Please cite this article in press as: Shen et al., Electrochemical ammonia synthesis: mechanistic understanding and catalyst design, Chem (2021), https://doi.org/10.1016/j.chempr.2021.01.009

Figure 19. Summary of strategies for improving the performance of electrocatalysts for NRR

Ti_3C_2 with –F groups was predicted to exhibit poor N_2 adsorption capacity with higher energy barrier, unfavorable for NRR. Li^+ modification was shown to enable suppression of the undesired HER.[62] It may also afford positively charged active sites that favor N_2 capture and reduction.[108] Enlightened by the metal-sulfur (M–S) linkages in the nitrogenase enzyme, surface tethering of Ru with aliphatic thiols was applied to modify its electronic structure, thus, promoting adsorption and polarization of N_2.[157] Concomitantly, the organic and hydrophobic nature of the thiols impeded proton transfer while allowing flow of N_2 to the surface of the catalyst. This synergistically boosted the rate of NH_3 generation.

Heteroatom doping can profoundly adjust the electronic structures of materials. Doping of nanocarbons with single or multiple heteroatoms (p-block elements such as B, N, O, S, Se, Te, P, F, Cl, Br, and I) was revealed to induce charge and spin densities on adjacent carbon atoms.[158] Charge accumulation favors N_2 adsorption on carbon atoms, while spin polarization facilitates the PDS of the first protonation to yield *NNH. These are expected to synergistically regulate the competition between NRR and HER. Boron doping can create Lewis acid sites with empty orbitals to bind N_2 forming B–N bonds. Among the boron structures, BC_3, BC_2O, and BCO_2, BC_3 was computed to display the lowest reaction energy barrier, which probably functioned as the major electrocatalytic centers in NRR.[36] However, the overpotential for HER may decrease with the increase of the boron content.[125] There exists an optimal boron content to improve the overall NRR efficiency and selectivity. The pyridinic N_3 configuration embedded in a graphitic layer, containing one protonated

Please cite this article in press as: Shen et al., Electrochemical ammonia synthesis: mechanistic understanding and catalyst design, Chem (2021), https://doi.org/10.1016/j.chempr.2021.01.009

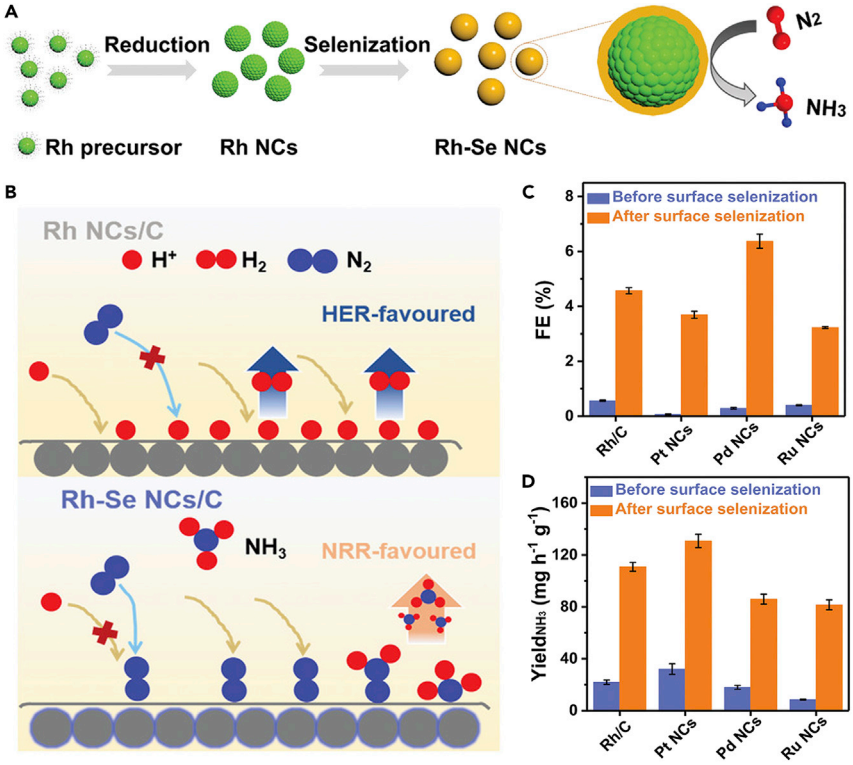

Figure 20. Schematic illustration of selenization process and comparison of Rh, Pt, Pd, and Ru for NRR before and after surface selenization

(A) Schematic illustrating selenization of Rh NCs.

(B) Schematic showing the proposed mechanism for NRR on the catalytic surface of the Rh NCs/C and Rh-Se NCs/C.

(C) NH_3 yield at −0.10 V (versus RHE) of various catalysts.

(D) FE for NH_3 formation at −0.10 V (versus RHE) on various catalysts.

Reprinted with permission from Yang et al.[153] Copyright 2020 Wiley-VCH.

pyridinic nitrogen and one neighboring atomic vacancy site, was predicted to promote N_2 chemisorption and reduction with relatively lower free energy requirements. The content of pyridinic-N in carbons can be further improved by addition of a secondary dopant (B or F), resulting in higher NRR activity.[87] In contrast to pristine and O-doped carbon atoms that barely adsorb N_2, S-, Se-, and Te-substituted C exhibited substantially increased N_2 adsorption, benefiting NRR.[159] Apart from the above-mentioned effects, doping of elements (such as B, F, and low-valence transition metal dopants)[160] into metal oxides or oxide-hydroxides may enrich surface oxygen vacancies by replacing the O atom rather than the metal atom.[161] Alternatively, doping of TiO_2 with stable Zr^{4+} induced tensile and compressive strains, hence, generating oxygen vacancies associated with adjoining bi-Ti^{3+} sites.[161] The oxygen vacancies promoted the back-donation of electrons to N_2 and accelerated the conversion of $*NH_2NH_2$ to $*NH_2$ and $*NH_3$. The dopant and oxygen vacancies jointly contribute to efficient conversion of N_2. Incorporation of Fe into reducible CeO_2 also facilitated formation of active Ce^{3+}–Ce^{3+} pairs to improve the selectivity of NRR with respect to HER.[162] Additionally, morphology evolution from CeO_2 nanoparticles to nanosheets with a larger surface area was induced upon Fe doping. These coupling impacts led to enhanced NH_3 yield. A recent work from Chen et al.[85] showed that M^{4+}-positioned Re in ReS_2 nanosheets could be replaced by metal species (e.g., Fe, Co, Ni, Cu, and Zn), leading to intensified charge density

Please cite this article in press as: Shen et al., Electrochemical ammonia synthesis: mechanistic understanding and catalyst design, Chem (2021), https://doi.org/10.1016/j.chempr.2021.01.009

around the dopant cations. The low-valent metal domain was revealed to offer more active sites for N_2 chemisorption and weaken the N≡N bonds for easier dissociation through proton coupling.

To further boost NRR activities, there are continuous efforts to modify the bulk and surface electronic properties and physical characteristics of electrocatalysts by tailoring the types and location of dopant atoms. Elucidation of active sites and optimization of activity are critically required as well. This is likely to be addressed by combining knowledge-guided controllable synthesis complimented by improved *in situ* and *operando* characterization techniques. Noteworthy, electrocatalysis of the NRR on N-doped materials should be studied with scrutiny to confirm the origin of evolved NH_3.

Surface structure tuning

Modulation of the surface structure of electrocatalysts can be achieved mainly by tailoring several important aspects: (1) surface amorphism; (2) exposed crystal facets; (3) lattice strain; (4) surface active areas; (5) surface porosity; (6) edges; (7) surface vacancies; (8) surface phase; and (9) single-atom sites.

Amorphization of an electrocatalyst enables a large increase of unsaturated coordination sites (resulting from dangling bonds), often giving rise to better catalytic activity than the crystalline counterpart.[163] In addition to abundant active sites, localized electrons in metal oxides could be augmented for π-back-donation, favoring N_2 activation and N≡N cleavage.[114] Despite these advantages, amorphous materials suffer from poor chemical and structure stability, hindering practical applications in NRR.

Crystal facets play a pivotal role in determining activity and selectivity of reactions. Surface facets differ in Lewis acidity and polarizing power and can therefore affect the adsorption and activation of N_2. Exposed facets may also influence adsorption of electrolytes on the catalyst surface, thus, affecting the catalytic performance. Facets that can selectively stabilize $*N_2H$ or destabilize $*NH_2$ are favorable to reduce N_2 to NH_3. Guided by these findings, Mo(110) nanofilms,[164] Au(730) nanorods,[146] and RhSb nanorods with high-index facets[95] were designed for effective N_2 electroreduction. For most metals except Re, the (211) step was modeled to be more reactive with lower theoretical overpotential than the (111) terrace.[38]

Strain (by changing the lattice spacing) can increase surface reactivity and selectivity of electrocatalysts by breaking the linear scaling relationship. In the *d*-band model, lattice expansion mitigates orbital overlap in transition metal atoms, thus, narrowing *d*-band along with shift to a higher energy level. This leads to a stronger interaction with adsorbates. In the eigenstress model, eigenstress takes place where adsorbates evoke strain at the catalyst surface. The binding energies of different intermediates can vary independently according to sizes and binding interactions with the strained surface. It is worth pointing out that the explicit use of strain to enhance the NRR is rarely reported.

Design of catalysts with high active surface areas can enrich the accessibility of catalytic sites for reactions.[165] This allows large physicochemical contact between the catalyst surface and N_2, which is essential for ambient N_2 conversion. The interactions between electrode and electrolyte are also strengthened, promoting interfacial adsorption-desorption dynamics and mass transport. Likewise, creation of a hierarchical architecture with high porosity and interconnected micro-, meso-, and

Please cite this article in press as: Shen et al., Electrochemical ammonia synthesis: mechanistic understanding and catalyst design, Chem (2021), https://doi.org/10.1016/j.chempr.2021.01.009

macroporous texture offers a way to enhance the adsorption and capture of N_2, potentially enhancing N_2 conversion rate and efficiency.[165] Macropores (>50 nm) accelerate transport and diffusion of reactants and products over electrodes, whereas mesopores (2–50 nm) and micropores (<2 nm) facilitate a high exposure of active sites. Further tailoring the diameter, volume, structure, and hydrophobicity of pores or channels allows for effective regulation of activity and selectivity.

Edges have coordination unsaturation and dangling bonds, providing useful catalytic sites. Increase of edge defects was demonstrated to promote NRR electrocatalysis. N_2 molecules were observed to preferably interact with the middle Ti atoms at the edge plane of Ti_3C_2 MXenes with low activation barriers.[166] As opposed to the basal plane that is inert for NRR, the edges of MoS_2 are capable of polarizing and converting N_2 to NH_3.[167] The positively charged Mo-edge was revealed to aid the formation of Mo−N bonds and reduce energy barriers for the PDS of $*N_2$ protonation to form *NNH.

Engineering of surface vacancies can regulate the electronic structure of catalysts, enabling enhanced charge transfer and optimal adsorption energetics of intermediates for electrocatalytic reactions. Oxygen vacancies in metal oxides,[21,35] NVs in polymeric carbon nitride[128] and metal nitrides,[2,32,101] and chalcogen vacancies in metal chalcogenides[110] have been claimed to efficiently bind and activate N_2. The underlying role of these vacancies is to modulate electron delocalization (inducing electron deficiency), boosting back-donation of electrons into the π N–N antibonding to weaken the N≡N triple bond. Additionally, carbon vacancies in MoC were predicted to diminish proton accumulation and increase the surface affinity of the metal carbide for N_2 and the NRR reaction intermediates.[168] Analogously, unsaturated carbons with single vacancy or double vacancy in reduced graphene oxide were found to bind N_2 strongly but suppress the binding of H, thereby improving the NH_3 selectivity.[154] Apart from the vacancies mentioned above, cation vacancies such as Fe^{3+},[169] Mo^{3+},[170] and Bi^{3+}[97] also enable a stronger binding of N_2 and its reduction intermediates, in effect lowering the overpotential required for the NRR. However, despite tremendous attempts to tune vacancies for efficient NRR, the decisive factors that vacancies play to determine catalytic behaviors remain to be answered. Creating a synergism between different vacancy sites may be promising to further enhance NRR. Equally importantly, the evolution of vacancies during NRR needs to be clarified. The surface vacancies may be deactivated by refilling corresponding atoms, restricting long-term N_2 fixation. To ameliorate this issue, partially filling these vacancies with an appropriate nonmetal dopant was shown to be useful.[171]

Surface active phases can be tailored by alloying or construction of bimetallic structures. This can induce surface rearrangement as well as spill-over effects and alter adsorption energies of reactants and intermediates, ultimately affecting reaction kinetics and selectivity. By incorporation of a suitable second metal, the *d*-band position of a metal can be lowered, weakening H adsorption. Concurrently, electron-deficient sites are created, affording strong N_2 affinity to kinetically drive NRR.[96] Additionally, effective *d–d* coupling between two metal sites may occur, which can bridge the electron transfer Coulomb gap toward rapid NRR.[172]

Single-atom sites display distinct catalytic activities due to low-coordination environment of the metal center, quantum size effects, and metal-support interactions. Isolated metal atoms have shown efficiency in catalyzing NRR at low overpotentials. The single-atom sites that are highly spin-polarized were supposed to activate $*N_2$,

Please cite this article in press as: Shen et al., Electrochemical ammonia synthesis: mechanistic understanding and catalyst design, Chem (2021), https://doi.org/10.1016/j.chempr.2021.01.009

stabilize *N_2H, and destabilize *NH_2 species. Meanwhile, adsorption of H on single atoms (with only top adsorption sites) may be hampered as a result of an ensemble effect, thus, restraining the HER.[117] Besides, single atoms supported on a curvature-rich surface may trigger interfacial polarization, which drives electron injection into the antibonding orbitals of N_2 to accelerate NRR.[173] However, more efforts are needed to unveil the exact coordination states of single sites for NRR. Finely tuning the interface between single-metal sites and support[118] as well as two individual dissimilar atoms may further improve NRR.

Construction of heterostructures

Heterostructure formation can enhance charge transfer and induce combined electronic and geometric effects to facilitate N_2 conversion. Relevant parameters such as interfacial compositions and facets, active surface areas, interfacial defects, and electronic coupling can be tuned to reach an optimum for NRR. For example, optimizing the interaction between entities at the interface permits creation of remarkably stable active sites for N_2 activation.[116] Hydrogen evolution is also impeded. In particular, the synergy arising from the interaction of different components can be attuned to maximize the orbital overlap with N_2 for optimal adsorption and reduction. Alternatively, a synergistic interplay between one phase as N_2 binding and activation sites and nearby phases as centers for hydrogenation could facilitate NH_3 formation. Such concept has been underscored by introducing a CoO_x layer to modulate the local electronic structure of Au NPs with positive valence sites.[174] The Au^{1+} active sites on Au NPs facilitate break of the N≡N bond and formation of N=N– intermediates via NRR, while Au^0 likely binds N–N– intermediates for subsequent hydrogenation reaction.

CONCLUSIONS AND FUTURE PERSPECTIVE

Over the past 5 years, significant and encouraging advances have been achieved for ambient electrochemical NRR to synthesize NH_3. However, there remain key challenges that need to be addressed in realizing the "green ammonia economy." Despite being thermodynamically feasible, high overpotentials are usually demanded to overcome the kinetic barrier of N≡N cleavage. Both yield rate and FE toward NH_3 formation remain low, which are typically less than 10^{-8} mol cm^{-2} s^{-1} and 10% (with the HER as the dominant reaction) respectively, far below the rate of 9.3×10^{-7} mol cm^{-2} s^{-1} that is desired for a commercially viable project.[175] Large overpotential and low selectivity intensify energy efficiency problem. Much more research efforts are thus required to make the electrochemical route competitive with the current NH_3 industry. The longevity of the NRR process is another critical concern. The normally reported stability tests in the literature are very commonly under 20 h, which is a too short duration for industrial implementation where thousands of hours of stable operation at high current density are expected. Therefore, future protocols for catalyst durability need to target much longer test durations. Endeavors also need to be put on illumination of catalyst degradation mechanisms. To promote the electrochemical synthesis, catalyst and electrolyte should always be taken into account and optimized together. Hence, we provide the following perspectives:

(1) Coupling different strategies for design of electrocatalysts. Compared with other electrochemical processes, the variety of materials reported for NRR is rather small. Investigation of new promising electrocatalysts continues to be an exciting arena. A combination of various design schemes enables one to jointly/collaboratively optimize the binding energies of the reactant and key intermediates, facilitating preferential NRR electrocatalysis. Mimicking an enzyme system allows for creation of multi-model active sites

to improve catalyst performance. Meanwhile, manipulation of the interplay between single atoms with different compositions with HER-inactive supports may maximize the exposure of active sites while concurrently suppressing the parasitic HER.

(2) Tuning electrocatalytic interface for active and selective NRR. At the electrode-electrolyte interface, the NRR and HER contest for protons from the electrolyte, electrons transferred from the catalyst, and surface active sites. The competition from the HER drastically affects the selectivity of NRR and governs the kinetics of NRR, such that the NRR activity drops at relatively more negative potentials. The low adsorption of N_2 molecules on the catalyst surface is another hurdle that limits the NRR. Design of a solid-liquid-gas tri-phase interface in a flow cell shows the potential to mitigate these issues. In this system, an airbag structure is formed on the surface of a superhydrophobic substrate. N_2 can be rapidly and continuously delivered to the catalyst layer, ensuring a high local concentration of the reactant. The contact area and time between the catalyst and N_2 are also greatly increased, leading to a high N_2 reduction rate.

(3) Combining *in situ* characterizations, theoretical calculations, and predictions (using a ML model). Development of *in situ*/*operando* techniques will aid in building up more valid theoretical models and deepen understanding of reaction pathways, degradation modes as well as catalytic structure-property relationships specific to given materials, further guiding new direction for catalyst design. Greater advances are expected through the collective knowledge and insights to be gained from fundamental research that integrates experiments and theory.

(4) Establishing standards and protocols for accurate, reliable, and repeatable NRR measurements. The impurity composition of N_2 supply should be clearly specified. Highly pure N_2 ($\geq$99.999%) and Ar ($\geq$99.999%) are suggested for adoption in NRR. Prior to NRR, the N_2 feed gas, electrolyte salts, electrocatalysts, and PEMs need to be purified to rule out artifacts from exogenous nitrogen contaminants (NH_3, nitrate/nitrite, and nitrous oxide). In particular, for catalysts that either contain structural/lattice nitrogen or are prepared from nitrates or ammonium precursors, $^{15}N_2$ isotopic labeling should be conducted to confirm the actual reduction of N_2. To avoid inadvertent NH_3 contamination and guarantee a true NRR, multiple control experiments at different applied potentials are necessary. It is also urgently required to develop more selective, precise, and *in situ* methods for NH_3 determination.

SUPPLEMENTAL INFORMATION

Supplemental Information can be found online at https://doi.org/10.1016/j.chempr.2021.01.009.

ACKNOWLEDGMENTS

This work was supported by the National Natural Science Foundation of China (21972010); Beijing Natural Science Foundation (2192039); the State Key Laboratory of Organic-Inorganic Composites (oic-201901001); Beijing University of Chemical Technology (XK180301, XK1804-2); and National Research Foundation of Korea (NRF-2019M3D1A1079303 and NRF-2019M3D3A1A01069099).

AUTHOR CONTRIBUTIONS

Conceptualization, Z.S.; writing – original draft, Z.S., H.S., X.L., C.C., and Y.J.; writing – review & editing, Z.S., J.M., and J.Q.; funding acquisition, Z.S. and Y.J.; supervision, Z.S.

Please cite this article in press as: Shen et al., Electrochemical ammonia synthesis: mechanistic understanding and catalyst design, Chem (2021), https://doi.org/10.1016/j.chempr.2021.01.009

CellPress

DECLARATION OF INTERESTS

The authors declare no competing interests.

REFERENCES

1. Andersen, S.Z., Čolić, V., Yang, S., Schwalbe, J.A., Nielander, A.C., McEnaney, J.M., Enemark-Rasmussen, K., Baker, J.G., Singh, A.R., Rohr, B.A., et al. (2019). A rigorous electrochemical ammonia synthesis protocol with quantitative isotope measurements. Nature *570*, 504–508.
2. Ye, T.N., Park, S.W., Lu, Y., Li, J., Sasase, M., Kitano, M., Tada, T., and Hosono, H. (2020). Vacancy-enabled N_2 activation for ammonia synthesis on an Ni-loaded catalyst. Nature *583*, 391–395.
3. Soloveichik, G. (2019). Electrochemical synthesis of ammonia as a potential alternative to the Haber–Bosch process. Nat. Catal. *2*, 377–380.
4. Liu, T., Gau, M.R., and Tomson, N.C. (2020). Mimicking the constrained geometry of a nitrogen-fixation intermediate. J. Am. Chem. Soc. *142*, 8142–8146.
5. Foster, S.L., Bakovic, S.I.P., Duda, R.D., Maheshwari, S., Milton, R.D., Minteer, S.D., Janik, M.J., Renner, J.N., and Greenlee, L.F. (2018). Catalysts for nitrogen reduction to ammonia. Nat. Catal. *1*, 490–500.
6. Lancaster, K.M., Roemelt, M., Ettenhuber, P., Hu, Y., Ribbe, M.W., Neese, F., Bergmann, U., and DeBeer, S. (2011). X-ray emission spectroscopy evidences a central carbon in the nitrogenase iron-molybdenum cofactor. Science *334*, 974–977.
7. Davy, H. (1807). I. The Bakerian Lecture, on some chemical agencies of electricity. Phil. Trans. R. Soc. *97*, 1–56.
8. Fichter, F., and Suter, R. (1922). Zur Frage der kathodischen Reduktion Des elementaren Stickstoffs. Helv. Chim. Acta *5*, 246–255.
9. MacLaughlin, C. (2019). Role for standardization in electrocatalytic ammonia synthesis: a conversation with leo liu, Lauren Greenlee, and Douglas macfarlane. ACS Energy Lett. *4*, 1432–1436.
10. Marnellos, G., and Stoukides, M. (1998). Ammonia synthesis at atmospheric pressure. Science *282*, 98–100.
11. Rod, T.H., Logadottir, A., and Nørskov, J.K. (2000). Ammonia synthesis at low temperatures. J. Chem. Phys. *112*, 5343–5347.
12. Sun, Z., Ma, T., Tao, H., Fan, Q., and Han, B. (2017). Fundamentals and challenges of electrochemical CO_2 reduction using two-dimensional materials. Chem *3*, 560–587.
13. Singh, A.R., Rohr, B.A., Statt, M.J., Schwalbe, J.A., Cargnello, M., and Nørskov, J.K. (2019). Strategies toward selective electrochemical ammonia synthesis. ACS Catal. *9*, 8316–8324.
14. Singh, A.R., Rohr, B.A., Schwalbe, J.A., Cargnello, M., Chan, K., Jaramillo, T.F., Chorkendorff, I., and Nørskov, J.K. (2017). Electrochemical ammonia synthesis—the selectivity challenge. ACS Catal. *7*, 706–709.
15. Zhou, F., Azofra, L.M., Ali, M., Kar, M., Simonov, A.N., McDonnell-Worth, C., Sun, C., Zhang, X., and MacFarlane, D.R. (2017). Electro-synthesis of ammonia from nitrogen at ambient temperature and pressure in ionic liquids. Energy Environ. Sci. *10*, 2516–2520.
16. Chalkley, M.J., Del Castillo, T.J., Matson, B.D., and Peters, J.C. (2018). Fe-mediated nitrogen fixation with a metallocene mediator: exploring pKa effects and demonstrating electrocatalysis. J. Am. Chem. Soc. *140*, 6122–6129.
17. Hao, Y.C., Guo, Y., Chen, L.W., Shu, M., Wang, X.Y., Bu, T.A., Gao, W.Y., Zhang, N., Su, X., Feng, X., et al. (2019). Promoting nitrogen electroreduction to ammonia with bismuth nanocrystals and potassium cations in water. Nat. Catal. *2*, 448–456.
18. Ma, J.L., Bao, D., Shi, M.M., Yan, J.M., and Zhang, X.B. (2017). Reversible nitrogen fixation based on a rechargeable lithium-nitrogen battery for energy storage. Chem *2*, 525–532.
19. Koh, C.S.L., Lee, H.K., Fan Sim, H.Y., Han, X., Phan-Quang, G.C., and Ling, X.Y. (2020). Turning water from a hindrance to the promotor of preferential electrochemical nitrogen reduction. Chem. Mater. *32*, 1674–1683.
20. Wang, J., Yu, L., Hu, L., Chen, G., Xin, H., and Feng, X. (2018). Ambient ammonia synthesis via palladium-catalyzed electrohydrogenation of dinitrogen at low overpotential. Nat. Commun. *9*, 1795.
21. Han, Z., Choi, C., Hong, S., Wu, T.S., Soo, Y.L., Jung, Y., Qiu, J., and Sun, Z. (2019). Activated TiO_2 with tuned vacancy for efficient electrochemical nitrogen reduction. Appl. Catal. B *257*, 117896.
22. Jaecheol, C., Hoang-Long, D., Manjunath, C., Bryan, H.R., Alexandr, S., and Douglas, M. (2020). Promoting nitrogen electroreduction to ammonia with bismuth nanocrystals and potassium cations in water. https://chemrxiv.org/articles/preprint/Promoting_Nitrogen_Electroreduction_to_Ammonia_with_Bismuth_Nanocrystals_and_Potassium_Cations_in_Water/11768814/1.
23. Lazouski, N., Chung, M., Williams, K., Gala, M.L., and Manthiram, K. (2020). Non-aqueous gas diffusion electrodes for rapid ammonia synthesis from nitrogen and water-splitting-derived hydrogen. Nat. Catal. *3*, 463–469.
24. Kitano, M., Inoue, Y., Yamazaki, Y., Hayashi, F., Kanbara, S., Matsuishi, S., Yokoyama, T., Kim, S.W., Hara, M., and Hosono, H. (2012). Ammonia synthesis using a stable electride as an electron donor and reversible hydrogen store. Nat. Chem. *4*, 934–940.
25. Cui, X., Tang, C., and Zhang, Q. (2018). A review of electrocatalytic reduction of dinitrogen to ammonia under ambient conditions. Adv. Energy Mater. *8*, 1800369.
26. van der Ham, C.J.M., Koper, M.T.M., and Hetterscheid, D.G.H. (2014). Challenges in reduction of dinitrogen by proton and electron transfer. Chem. Soc. Rev. *43*, 5183–5191.
27. Hu, L., Xing, Z., and Feng, X. (2020). Understanding the electrocatalytic interface for ambient ammonia synthesis. ACS Energy Lett. *5*, 430–436.
28. Sippel, D., Rohde, M., Netzer, J., Trncik, C., Gies, J., Grunau, K., Djurdjevic, I., Decamps, L., Andrade, S.L.A., and Einsle, O. (2018). A bound reaction intermediate sheds light on the mechanism of nitrogenase. Science *359*, 1484–1489.
29. Skúlason, E., Bligaard, T., Gudmundsdóttir, S., Studt, F., Rossmeisl, J., Abild-Pedersen, F., Vegge, T., Jónsson, H., and Nørskov, J.K. (2012). A theoretical evaluation of possible transition metal electro-catalysts for N_2 reduction. Phys. Chem. Chem. Phys. *14*, 1235–1245.
30. Pool, J.A., Lobkovsky, E., and Chirik, P.J. (2004). Hydrogenation and cleavage of dinitrogen to ammonia with a zirconium complex. Nature *427*, 527–530.
31. Iwamoto, M., Akiyama, M., Aihara, K., and Deguchi, T. (2017). Ammonia synthesis on wool-like Au, Pt, Pd, Ag, or Cu electrode catalysts in nonthermal atmospheric-pressure plasma of N_2 and H_2. ACS Catal. *7*, 6924–6929.
32. Yang, X., Kattel, S., Nash, J., Chang, X., Lee, J.H., Yan, Y., Chen, J.G., and Xu, B. (2019). Quantification of active sites and elucidation of the reaction mechanism of the electrochemical nitrogen reduction reaction on vanadium nitride. Angew. Chem. Int. Ed. Engl. *58*, 13768–13772.
33. Abghoui, Y., Garden, A.L., Hlynsson, V.F., Björgvinsdóttir, S., Ólafsdóttir, H., and Skúlason, E. (2015). Enabling electrochemical reduction of nitrogen to ammonia at ambient conditions through rational catalyst design. Phys. Chem. Chem. Phys. *17*, 4909–4918.
34. Comer, B.M., Liu, Y.H., Dixit, M.B., Hatzell, K.B., Ye, Y., Crumlin, E.J., Hatzell, M.C., and Medford, A.J. (2018). The role of adventitious carbon in photo-catalytic nitrogen fixation by titania. J. Am. Chem. Soc. *140*, 15157–15160.
35. Sun, Z., Huo, R., Choi, C., Hong, S., Wu, T.S., Qiu, J., Yan, C., Han, Z., Liu, Y., Soo, Y.-L., and Joong, Y. (2019). Oxygen vacancy enables electrochemical N_2 fixation over WO_3 with tailored structure. Nano Energy *62*, 869–875.
36. Yu, X., Han, P., Wei, Z., Huang, L., Gu, Z., Peng, S., Ma, J., and Zheng, G. (2018). Boron-doped graphene for electrocatalytic N_2 reduction. Joule *2*, 1610–1622.
37. Medford, A.J., Vojvodic, A., Hummelshøj, J.S., Voss, J., Abild-Pedersen, F., Studt, F., Bligaard, T., Nilsson, A., and Nørskov, J.K. (2015). From the Sabatier principle to a

predictive theory of transition-metal heterogeneous catalysis. J. Catal. *328*, 36–42.

38. Montoya, J.H., Tsai, C., Vojvodic, A., and Nørskov, J.K. (2015). The challenge of electrochemical ammonia synthesis: a new perspective on the role of nitrogen scaling relations. ChemSusChem *8*, 2180–2186.

39. Suryanto, B.H.R., Du, H.L., Wang, D., Chen, J., Simonov, A.N., and MacFarlane, D.R. (2019). Challenges and prospects in the catalysis of electroreduction of nitrogen to ammonia. Nat. Catal. *2*, 290–296.

40. Halmann, M. (1984). Electrochemical reduction of molecular nitrogen to ammonia in aqueous alakli: a re-examination. J. Electroanal. Chem. Interfacial Electrochem. *181*, 307–308.

41. Tang, C., and Qiao, S.Z. (2019). How to explore ambient electrocatalytic nitrogen reduction reliably and insightfully. Chem. Soc. Rev. *48*, 3166–3180.

42. Chen, Y., Liu, H., Ha, N., Licht, S., Gu, S., and Li, W. (2020). Revealing nitrogen-containing species in commercial catalysts used for ammonia electrosynthesis. Nat. Catal. *3*, 1055–1061.

43. Chen, G.F., Ren, S., Zhang, L., Cheng, H., Luo, Y., Zhu, K., Ding, L.X., and Wang, H. (2019). Advances in electrocatalytic N_2 reduction—strategies to tackle the selectivity challenge. Small Methods *3*, 1800337.

44. Choi, J., Du, H.L., Nguyen, C.K., Suryanto, B.H.R., Simonov, A.N., and MacFarlane, D.R. (2020). Electroreduction of nitrates, nitrites, and gaseous nitrogen oxides: a potential source of ammonia in dinitrogen reduction studies. ACS Energy Lett. *5*, 2095–2097.

45. Dabundo, R., Lehmann, M.F., Treibergs, L., Tobias, C.R., Altabet, M.A., Moisander, P.H., and Granger, J. (2014). The contamination of commercial $^{15}N_2$ gas stocks with ^{15}N-labeled nitrate and ammonium and consequences for nitrogen fixation measurements. PLoS One *9*, e110335.

46. Shan, W., Liu, F., He, H., Shi, X., and Zhang, C. (2011). The remarkable improvement of a Ce–Ti based catalyst for NO x abatement, prepared by a homogeneous precipitation method. ChemCatChem *3*, 1286–1289.

47. Wang, Z., Wang, Z., Ye, Y., Chen, N., and Li, H. (2016). Study on the removal of nitric oxide (NO) by dual oxidant (H_2O_2/$S_2O_8^{2-}$) system. Chem. Eng. Sci. *145*, 133–140.

48. Ivančič, I., and Degobbis, D. (1984). An optimal manual procedure for ammonia analysis in natural waters by the indophenol blue method. Water Res. *18*, 1143–1147.

49. Yuen, S.H., and Pollard, A.G. (1954). Determination of nitrogen in agricultural materials by the nessler reagent. II.—micro-determinations in plant tissue and in soil extracts. J. Sci. Food Agric. *5*, 364–369.

50. Bower, C.E., and Holm-Hansen, T. (1980). A salicylate–hypochlorite method for determining ammonia in seawater. Can. J. Fish. Aquat. Sci. *37*, 794–798.

51. Michalski, R., and Kurzyca, I. (2006). Determination of nitrogen species (nitrate, nitrite and ammonia ions) in environmental samples by ion chromatography. Pol. J. Environ. Stud. *15*, 5–18.

52. LeDuy, A., and Samson, R. (1982). Testing of an ammonia ion selective electrode for ammonia nitrogen measurement in the methanogenic sludge. Biotechnol. Lett. *4*, 303–306.

53. Cohn, V.H., and Lyle, J. (1966). A fluorometric assay for glutathione. Anal. Biochem. *14*, 434–440.

54. Liu, C., Sakimoto, K.K., Colón, B.C., Silver, P.A., and Nocera, D.G. (2017). Ambient nitrogen reduction cycle using a hybrid inorganic-biological system. Proc. Natl. Acad. Sci. USA *114*, 6450–6455.

55. Hodgetts, R.Y., Kiryutin, A.S., Nichols, P., Du, H.L., Bakker, J.M., Macfarlane, D.R., and Simonov, A.N. (2020). Refining universal procedures for ammonium quantification via rapid ^{1}H NMR analysis for dinitrogen reduction studies. ACS Energy Lett. *5*, 736–741.

56. Yu, W., Lewis, N.S., Gray, H.B., and Dalleska, N.F. (2020). Isotopically selective quantification by UPLC-MS of aqueous ammonia at submicromolar concentrations using dansyl chloride derivatization. ACS Energy Lett. *5*, 1532–1536.

57. Yao, Y., Wang, H., Yuan, X.Z., Li, H., and Shao, M. (2019). Electrochemical nitrogen reduction reaction on ruthenium. ACS Energy Lett. *4*, 1336–1341.

58. Yao, Y., Zhu, S., Wang, H., Li, H., and Shao, M. (2020). A spectroscopic study of electrochemical nitrogen and nitrate reduction on rhodium surfaces. Angew. Chem. Int. Ed. Engl. *59*, 10479–10483.

59. Watt, G.W., and Chrisp, J.D. (1952). Spectrophotometric method for determination of hydrazine. Anal. Chem. *24*, 2006–2008.

60. Giddey, S., Badwal, S.P.S., and Kulkarni, A. (2013). Review of electrochemical ammonia production technologies and materials. Int. J. Hydrogen Energy *38*, 14576–14594.

61. Han, L., Liu, X., Chen, J., Lin, R., Liu, H., Lü, F., Bak, S., Liang, Z., Zhao, S., Stavitski, E., et al. (2019). Atomically dispersed molybdenum catalysts for efficient ambient nitrogen fixation. Angew. Chem. Int. Ed. Engl. *58*, 2321–2325.

62. Chen, G.F., Cao, X., Wu, S., Zeng, X., Ding, L.X., Zhu, M., and Wang, H. (2017). Ammonia electrosynthesis with high selectivity under ambient conditions via a Li^+ incorporation strategy. J. Am. Chem. Soc. *139*, 9771–9774.

63. Köleli, F., and Kayan, D.B. (2010). Low overpotential reduction of dinitrogen to ammonia in aqueous media. J. Electroanal. Chem. *638*, 119–122.

64. Zhang, Q., Liu, B., Yu, L., Bei, Y., and Tang, B. (2020). Synergistic promotion of the electrochemical reduction of nitrogen to ammonia by phosphorus and potassium. ChemCatChem *12*, 334–341.

65. Battino, R., Rettich, T.R., and Tominaga, T. (1984). The solubility of nitrogen and air in liquids. J. Phys. Chem. Ref. Data *13*, 563–600.

66. Kang, C.S.M., Zhang, X., and MacFarlane, D.R. (2019). High nitrogen gas solubility and physicochemical properties of [C4mpyr][eFAP]–fluorinated solvent mixtures. J. Phys. Chem. C *123*, 21376–21385.

67. Tsuneto, A., Kudo, A., and Sakata, T. (1994). Lithium-mediated electrochemical reduction of high pressure N_2 to NH_3. J. Electroanal. Chem. *367*, 183–188.

68. Köleli, F., and Röpke, T. (2006). Electrochemical hydrogenation of dinitrogen to ammonia on a polyaniline electrode. Appl. Catal. B *62*, 306–310.

69. Kim, K., Lee, N., Yoo, C.-Y., Kim, J.-N., Yoon, H.C., and Han, J.-I. (2016). Communication—electrochemical reduction of nitrogen to ammonia in 2-propanol under ambient temperature and pressure. J. Electrochem. Soc. *163*, F610–F612.

70. Kim, K., Yoo, C.Y., Kim, J.N., Yoon, H.C., and Han, J.I. (2016). Electrochemical synthesis of ammonia from water and nitrogen in ethylenediamine under ambient temperature and pressure. J. Electrochem. Soc. *163*, F1523–F1526.

71. Lee, H.K., Koh, C.S.L., Lee, Y.H., Liu, C., Phang, I.Y., Han, X., Tsung, C.K., and Ling, X.Y. (2018). Favoring the unfavored: selective electrochemical nitrogen fixation using a reticular chemistry approach. Sci. Adv. *4*, eaar3208.

72. Lazouski, N., Schiffer, Z.J., Williams, K., and Manthiram, K. (2019). Understanding continuous lithium-mediated electrochemical nitrogen reduction. Joule *3*, 1127–1139.

73. Kang, C.S.M., Zhang, X., and MacFarlane, D.R. (2018). Synthesis and physicochemical properties of fluorinated ionic liquids with high nitrogen gas solubility. J. Phys. Chem. C *122*, 24550–24558.

74. Suryanto, B.H.R., Kang, C.S.M., Wang, D., Xiao, C., Zhou, F., Azofra, L.M., Cavallo, L., Zhang, X., and MacFarlane, D.R. (2018). Rational electrode–electrolyte design for efficient ammonia electrosynthesis under ambient conditions. ACS Energy Lett. *3*, 1219–1224.

75. Yan, R., Antonietti, M., and Oschatz, M. (2018). Toward the experimental understanding of the energy storage mechanism and ion dynamics in ionic liquid based supercapacitors. Adv. Energy Mater. *8*, 1800026.

76. Ortuño, M.A., Hollóczki, O., Kirchner, B., and López, N. (2019). Selective electrochemical nitrogen reduction driven by hydrogen bond interactions at metal–ionic liquid interfaces. J. Phys. Chem. Lett. *10*, 513–517.

77. Li, X.F., Li, Q.K., Cheng, J., Liu, L., Yan, Q., Wu, Y., Zhang, X.H., Wang, Z.Y., Qiu, Q., and Luo, Y. (2016). Conversion of dinitrogen to ammonia by FeN_3-embedded graphene. J. Am. Chem. Soc. *138*, 8706–8709.

78. Einsle, O., Tezcan, F.A., Andrade, S.L.A., Schmid, B., Yoshida, M., Howard, J.B., and Rees, D.C. (2002). Nitrogenase MoFe-protein

at 1.16 Å resolution: a central ligand in the FeMo-cofactor. Science *297*, 1696–1700.

79. Yandulov, D.V., and Schrock, R.R. (2003). Catalytic reduction of dinitrogen to ammonia at a single molybdenum center. Science *301*, 76–78.

80. Back, S., and Jung, Y. (2016). On the mechanism of electrochemical ammonia synthesis on the Ru catalyst. Phys. Chem. Chem. Phys. *18*, 9161–9166.

81. Ling, C., Zhang, Y., Li, Q., Bai, X., Shi, L., and Wang, J. (2019). New mechanism for N_2 reduction: the essential role of surface hydrogenation. J. Am. Chem. Soc. *141*, 18264–18270.

82. Yang, X., Nash, J., Anibal, J., Dunwell, M., Kattel, S., Stavitski, E., Attenkofer, K., Chen, J.G., Yan, Y., and Xu, B. (2018). Mechanistic insights into electrochemical nitrogen reduction reaction on vanadium nitride nanoparticles. J. Am. Chem. Soc. *140*, 13387–13391.

83. Yao, Y., Zhu, S., Wang, H., Li, H., and Shao, M. (2018). A spectroscopic study on the nitrogen electrochemical reduction reaction on gold and platinum surfaces. J. Am. Chem. Soc. *140*, 1496–1501.

84. Zeng, L., Li, X., Chen, S., Wen, J., Huang, W., and Chen, A. (2020). Unique hollow Ni–Fe@MoS_2 nanocubes with boosted electrocatalytic activity for N_2 reduction to NH_3. J. Mater. Chem. A *8*, 7339–7349.

85. Lai, F., Chen, N., Ye, X., He, G., Zong, W., Holt, K.B., Pan, B., Parkin, I.P., Liu, T., and Chen, R. (2020). Refining energy levels in ReS_2 nanosheets by low-valent transition-metal doping for dual-boosted electrochemical ammonia/hydrogen production. Adv. Funct. Mater. *30*, 1907376.

86. Lv, X.W., Liu, Y., Hao, R., Tian, W., and Yuan, Z.Y. (2020). Urchin-like Al-doped Co_3O_4 nanospheres rich in surface oxygen vacancies enable efficient ammonia electrosynthesis. ACS Appl. Mater. Interfaces *12*, 17502–17508.

87. Ren, J.T., Wan, C.Y., Pei, T.Y., Lv, X.W., and Yuan, Z.Y. (2020). Promotion of electrocatalytic nitrogen reduction reaction on N-doped porous carbon with secondary heteroatoms. Appl. Catal. B *266*, 118633.

88. Yuan, L.P., Wu, Z.Y., Jiang, W.J., Tang, T., Niu, S., and Hu, J.S. (2020). Phosphorus-doping activates carbon nanotubes for efficient electroreduction of nitrogen to ammonia. Nano Res. *13*, 1376–1382.

89. Fu, Y., Li, T., Zhou, G., Guo, J., Ao, Y., Hu, Y., Shen, J., Liu, L., and Wu, X. (2020). Dual-metal-driven selective pathway of nitrogen reduction in orderly atomic-hybridized Re_2MnS_6 ultrathin nanosheets. Nano Lett. *20*, 4960–4967.

90. Yao, D., Tang, C., Li, L., Xia, B., Vasileff, A., Jin, H., Zhang, Y., and Qiao, S.Z. (2020). In situ fragmented bismuth nanoparticles for electrocatalytic nitrogen reduction. Adv. Energy Mater. *10*, 2001289.

91. Xu, W., Fan, G., Chen, J., Li, J., Zhang, L., Zhu, S., et al. (2020). Nanoporous palladium hydride for electrocatalytic N_2 reduction under ambient conditions. Angew. Chem. Int. Ed. Engl. *59*, 3511–3516.

92. Valov, I., Luerssen, B., Mutoro, E., Gregoratti, L., De Souza, R.A., Bredow, T., Günther, S., Barinov, A., Dudin, P., Martin, M., and Janek, J. (2011). Electrochemical activation of molecular nitrogen at the Ir/YSZ interface. Phys. Chem. Chem. Phys. *13*, 3394–3410.

93. Xue, Z.H., Zhang, S.N., Lin, Y.X., Su, H., Zhai, G.Y., Han, J.T., Yu, Q.Y., Li, X.H., Antonietti, M., and Chen, J.S. (2019). Electrochemical reduction of N_2 into NH_3 by donor-acceptor couples of Ni and Au nanoparticles with a 67.8% faradaic efficiency. J. Am. Chem. Soc. *141*, 14976–14980.

94. Liu, Y., Huang, L., Zhu, X., Fang, Y., and Dong, S. (2020). Coupling Cu with Au for enhanced electrocatalytic activity of nitrogen reduction reaction. Nanoscale *12*, 1811–1816.

95. Zhang, N., Li, L., Wang, J., Hu, Z., Shao, Q., Xiao, X., and Huang, X. (2020). Surface-regulated rhodium–antimony nanorods for nitrogen fixation. Angew. Chem. Int. Ed. Engl. *59*, 8066–8071.

96. Sim, H.Y.F., Chen, J.R.T., Koh, C.S.L., Lee, H.K., Han, X., Phan-Quang, G.C., Pang, J.Y., Lay, C.L., Pedireddy, S., Phang, I.Y., et al. (2020). ZIF-induced d-band modification in a bimetallic nanocatalyst: achieving over 44 % efficiency in the ambient nitrogen reduction reaction. Angew. Chem. Int. Ed. Engl. *59*, 16997–17003.

97. Wang, Y., Shi, M.-M., Bao, D., Meng, F.-L., Zhang, Q., Zhou, Y.T., Liu, K.-H., Zhang, Y., Wang, J.-Z., Chen, Z.-W., et al. (2019). Generating defect-rich bismuth for enhancing the rate of nitrogen electroreduction to ammonia. Angew. Chem. Int. Ed. Engl. *58*, 9464–9469.

98. Fang, Y., Liu, Z., Han, J., Jin, Z., Han, Y., Wang, F., Niu, Y., Wu, Y., and Xu, Y. (2019). High-performance electrocatalytic conversion of N_2 to NH_3 using oxygen-vacancy-rich TiO_2 in situ grown on Ti_3C_2Tx MXene. Adv. Energy Mater. *9*, 1803406.

99. Huang, L., Wu, J., Han, P., Al-Enizi, A.M., Almutairi, T.M., Zhang, L., and Zheng, G. (2019). NbO_2 electrocatalyst toward 32% faradaic efficiency for N_2 fixation. Small Methods *3*, 1800386.

100. Abghoui, Y., and Skúlason, E. (2017). Electrochemical synthesis of ammonia via Mars-van Krevelen mechanism on the (111) facets of group III–VII transition metal mononitrides. Catal. Today *286*, 78–84.

101. Jin, H., Li, L., Liu, X., Tang, C., Xu, W., Chen, S., Song, L., Zheng, Y., and Qiao, S.Z. (2019). Nitrogen vacancies on 2D layered W_2N_3: a stable and efficient active site for nitrogen reduction reaction. Adv. Mater. *31*, 1902709.

102. Hu, B., Hu, M., Seefeldt, L., and Liu, T.L. (2019). Electrochemical dinitrogen reduction to ammonia by Mo_2N: catalysis or decomposition? ACS Energy Lett. *4*, 1053–1054.

103. Peng, J., Chen, X., Ong, W.J., Zhao, X., and Li, N. (2019). Surface and heterointerface engineering of 2D MXenes and their nanocomposites: insights into electro- and photocatalysis. Chem *5*, 18–50.

104. Wang, S., Li, B., Li, L., Tian, Z., Zhang, Q., Chen, L., and Zeng, X.C. (2020). Highly efficient N_2 fixation catalysts: transition-metal carbides M_2C (MXenes). Nanoscale *12*, 538–547.

105. Matanovic, I., and Garzon, F.H. (2018). Nitrogen electroreduction and hydrogen evolution on cubic molybdenum carbide: a density functional study. Phys. Chem. Chem. Phys. *20*, 14679–14687.

106. Zhang, C., Wang, D., Wan, Y., Lv, R., Li, S., Li, B., Zou, X., and Yang, S. (2020). Vanadium carbide with periodic anionic vacancies for effective electrocatalytic nitrogen reduction. Mater. Today *40*, 18–25.

107. Li, X., Li, T., Ma, Y., Wei, Q., Qiu, W., Guo, H., Shi, X., Zhang, P., Asiri, A.M., Chen, L., et al. (2018). Boosted electrocatalytic N_2 reduction to NH_3 by defect-rich MoS_2 nanoflower. Adv. Energy Mater. *8*, 1801357.

108. Liu, Y., Han, M., Xiong, Q., Zhang, S., Zhao, C., Gong, W., Wang, G., Zhang, H., and Zhao, H. (2019). Dramatically enhanced ambient ammonia electrosynthesis performance by in-operando created Li–S interactions on MoS_2 electrocatalyst. Adv. Energy Mater. *9*, 1803935.

109. Wang, H.-B., Wang, J.Q., Zhang, R., Cheng, C.-Q., Qiu, K.-W., Yang, Y.-J., Mao, J., Liu, H., Du, M., Dong, C.-K., et al. (2020). Bionic design of a Mo(IV)-doped FeS_2 catalyst for electroreduction of dinitrogen to ammonia. ACS Catal. *10*, 4914–4921.

110. Lai, F., Zong, W., He, G., Xu, Y., Huang, H., Weng, B., Rao, D., Martens, J.A., Hofkens, J., Parkin, I.P., and Liu, T. (2020). N_2 electroreduction to NH_3 by selenium vacancy-rich $ReSe_2$ catalysis at an abrupt interface. Angew. Chem. Int. Ed. Engl. *59*, 13320–13327.

111. Wang, Y., Chen, A., Lai, S., Peng, X., Zhao, S., Hu, G., Qiu, Y., Ren, J., Liu, X., and Luo, J. (2020). Self-supported $NbSe_2$ nanosheet arrays for highly efficient ammonia electrosynthesis under ambient conditions. J. Catal. *381*, 78–83.

112. Sun, Z., Talreja, N., Tao, H., Texter, J., Muhler, M., Strunk, J., and Chen, J. (2018). Catalysis of carbon dioxide photoreduction on nanosheets: fundamentals and challenges. Angew. Chem. Int. Ed. Engl. *57*, 7610–7627.

113. Lv, C., Zhong, L., Yao, Y., Liu, D., Kong, Y., Jin, X., Fang, Z., Xu, W., Yan, C., Dinh, K.N., et al. (2020). Boosting electrocatalytic ammonia production through mimicking "π back-donation". Chem *6*, 2690–2702.

114. Lv, C., Yan, C., Chen, G., Ding, Y., Sun, J., Zhou, Y., and Yu, G. (2018). An amorphous noble-metal-free electrocatalyst that enables nitrogen fixation under ambient conditions. Angew. Chem. Int. Ed. Engl. *57*, 6073–6076.

115. Liu, X., Jang, H., Li, P., Wang, J., Qin, Q., Kim, M.G., Li, G., and Cho, J. (2019). Antimony-based composites loaded on phosphorus-doped carbon for boosting faradaic efficiency of the electrochemical nitrogen reduction reaction. Angew. Chem. Int. Ed. Engl. *58*, 13329–13334.

116. Fang, Y., Xue, Y., Li, Y., Yu, H., Hui, L., Liu, Y., Xing, C., Zhang, C., Zhang, D., Wang, Z., et al. (2020). Graphdiyne interface engineering:

highly active and selective ammonia synthesis. Angew. Chem. Int. Ed. Engl. *59*, 13021–13027.

117. Choi, C., Back, S., Kim, N.Y., Lim, J., Kim, Y.H., and Jung, Y. (2018). Suppression of hydrogen evolution reaction in electrochemical N_2 reduction using single-atom catalysts: a computational guideline. ACS Catal. *8*, 7517–7525.

118. Tao, H., Choi, C., Ding, L.X., Jiang, Z., Han, Z., Jia, M., Fan, Q., Gao, Y., Wang, H., Robertson, A.W., et al. (2019). Nitrogen fixation by Ru single-atom electrocatalytic reduction. Chem *5*, 204–214.

119. Lü, F., Zhao, S., Guo, R., He, J., Peng, X., Bao, H., Fu, J., Han, L., Qi, G., Luo, J., et al. (2019). Nitrogen-coordinated single Fe sites for efficient electrocatalytic N_2 fixation in neutral media. Nano Energy *61*, 420–427.

120. Wang, Y., Cui, X., Zhao, J., Jia, G., Gu, L., Zhang, Q., Meng, L., Shi, Z., Zheng, L., Wang, C., et al. (2019). Rational design of Fe–N/C hybrid for enhanced nitrogen reduction electrocatalysis under ambient conditions in aqueous solution. ACS Catal. *9*, 336–344.

121. Wang, M., Liu, S., Qian, T., Liu, J., Zhou, J., Ji, H., Xiong, J., Zhong, J., and Yan, C. (2019). Over 56.55% faradaic efficiency of ambient ammonia synthesis enabled by positively shifting the reaction potential. Nat. Commun. *10*, 341.

122. Zhang, S., Jin, M., Shi, T., Han, M., Sun, Q., Lin, Y., Ding, Z., Zheng, L.R., Wang, G., Zhang, Y., et al. (2020). Electrocatalytically active Fe-($O-C_2$)$_4$ single-atom sites for efficient reduction of nitrogen to ammonia. Angew. Chem. Int. Ed. Engl. *59*, 13423–13429.

123. Wang, X., Wang, W., Qiao, M., Wu, G., Chen, W., Yuan, T., Xu, Q., Chen, M., Zhang, Y., Wang, X., et al. (2018). Atomically dispersed Au_1 catalyst towards efficient electrochemical synthesis of ammonia. Sci. Bull. *63*, 1246–1253.

124. Chen, H., Zhu, X., Huang, H., Wang, H., Wang, T., Zhao, R., Zheng, H., Asiri, A.M., Luo, Y., and Sun, X. (2019). Sulfur dots–graphene nanohybrid: a metal-free electrocatalyst for efficient N_2-to-NH_3 fixation under ambient conditions. Chem. Commun. *55*, 3152–3155.

125. Liu, B., Zheng, Y., Peng, H.Q., Ji, B., Yang, Y., Tang, Y., Lee, C.S., and Zhang, W. (2020). Nanostructured and boron-doped diamond as an electrocatalyst for nitrogen fixation. ACS Energy Lett. *5*, 2590–2596.

126. Fan, Q., Choi, C., Yan, C., Liu, Y., Qiu, J., Hong, S., Jung, Y., and Sun, Z. (2019). High-yield production of few-layer boron nanosheets for efficient electrocatalytic N_2 reduction. Chem. Commun. *55*, 4246–4249.

127. Légaré, M.A., Bélanger-Chabot, G., Dewhurst, R.D., Welz, E., Krummenacher, I., Engels, B., and Braunschweig, H. (2018). Nitrogen fixation and reduction at boron. Science *359*, 896–900.

128. Lv, C., Qian, Y., Yan, C., Ding, Y., Liu, Y., Chen, G., and Yu, G. (2018). Defect engineering metal-free polymeric carbon nitride electrocatalyst for effective nitrogen fixation under ambient conditions. Angew. Chem. Int. Ed. Engl. *57*, 10246–10250.

129. Zhang, L., Ding, L.X., Chen, G.F., Yang, X., and Wang, H. (2019). Ammonia synthesis under ambient conditions: selective electroreduction of dinitrogen to ammonia on black phosphorus nanosheets. Angew. Chem. Int. Ed. Engl. *58*, 2612–2616.

130. Xu, G., Li, H., Bati, A.S.R., Bat-Erdene, M., Nine, M.J., Losic, D., Chen, Y., Shapter, J.G., Batmunkh, M., and Ma, T. (2020). Nitrogen-doped phosphorene for electrocatalytic ammonia synthesis. J. Mater. Chem. A *8*, 15875–15883.

131. Zhang, Y., Dong, N., Tao, H., Yan, C., Huang, J., Liu, T., Robertson, A.W., Texter, J., Wang, J., and Sun, Z. (2017). Exfoliation of stable 2D black phosphorus for device fabrication. Chem. Mater. *29*, 6445–6456.

132. Liu, Q., Zhang, X., Wang, J., Zhang, Y., Bian, S., Cheng, Z., Kang, N., Huang, H., Gu, S., Wang, Y., et al. (2020). Crystalline red phosphorus nanoribbons: large-scale synthesis and electrochemical nitrogen fixation. Angew. Chem. Int. Ed. Engl. *59*, 14383–14387.

133. Qiu, W., Xie, X.Y., Qiu, J., Fang, W.H., Liang, R., Ren, X., Ji, X., Cui, G., Asiri, A.M., Cui, G., et al. (2018). High-performance artificial nitrogen fixation at ambient conditions using a metal-free electrocatalyst. Nat. Commun. *9*, 3485.

134. Liu, C., Li, Q., Wu, C., Zhang, J., Jin, Y., MacFarlane, D.R., and Sun, C. (2019). Single-boron catalysts for nitrogen reduction reaction. J. Am. Chem. Soc. *141*, 2884–2888.

135. Liu, X., Jiao, Y., Zheng, Y., and Qiao, S.Z. (2020). Isolated boron sites for electroreduction of dinitrogen to ammonia. ACS Catal. *10*, 1847–1854.

136. Abghoui, Y., Sigtryggsson, S.B., and Skúlason, E. (2019). Biomimetic nitrogen fixation catalyzed by transition metal sulfide surfaces in an electrolytic cell. ChemSusChem *12*, 4265–4273.

137. Gu, G.H., Noh, J., Kim, I., and Jung, Y. (2019). Machine learning for renewable energy materials. J. Mater. Chem. A *7*, 17096–17117.

138. Kim, M., Yeo, B.C., Park, Y., Lee, H.M., Han, S.S., and Kim, D. (2020). Artificial intelligence to accelerate the discovery of N_2 electroreduction catalysts. Chem. Mater. *32*, 709–720.

139. Zafari, M., Kumar, D., Umer, M., and Kim, K.S. (2020). Machine learning-based high throughput screening for nitrogen fixation on boron-doped single atom catalysts. J. Mater. Chem. A *8*, 5209–5216.

140. Hoar, B.B., Lu, S., and Liu, C. (2020). Machine-learning-enabled exploration of morphology influence on wire-array electrodes for electrochemical nitrogen fixation. J. Phys. Chem. Lett. *11*, 4625–4630.

141. Noh, J., Gu, G.H., Kim, S., and Jung, Y. (2020). Machine-enabled inverse design of inorganic solid materials: promises and challenges. Chem. Sci. *11*, 4871–4881.

142. Xie, T., and Grossman, J.C. (2018). Crystal graph convolutional neural networks for an accurate and interpretable prediction of material properties. Phys. Rev. Lett. *120*, 145301.

143. Logan, D.L. (2011). A First Course in the Finite Element Method (Cengage Learning).

144. Goodfellow, I., Bengio, Y., and Courville, A. (2016). Deep Learning (MIT Press).

145. Wang, D., Azofra, L.M., Harb, M., Cavallo, L., Zhang, X., Suryanto, B.H.R., and MacFarlane, D.R. (2018). Energy-efficient nitrogen reduction to ammonia at low overpotential in aqueous electrolyte under ambient conditions. ChemSusChem *11*, 3416–3422.

146. Bao, D., Zhang, Q., Meng, F.L., Zhong, H.X., Shi, M.M., Zhang, Y., Yan, J.M., Jiang, Q., and Zhang, X.B. (2017). Electrochemical reduction of N_2 under ambient conditions for artificial N_2 fixation and renewable energy storage using N_2/NH_3 cycle. Adv. Mater. *29*, 1604799.

147. Choi, J., Suryanto, B.H.R., Wang, D., Du, H.L., Hodgetts, R.Y., Ferrero Vallana, F.M., MacFarlane, D.R., and Simonov, A.N. (2020). Identification and elimination of false positives in electrochemical nitrogen reduction studies. Nat. Commun. *11*, 5546.

148. Tayyebi, E., Abghoui, Y., and Skúlason, E. (2019). Elucidating the mechanism of electrochemical N_2 reduction at the Ru(0001) electrode. ACS Catal. *9*, 11137–11145.

149. Chen, L.Y., Kuo, T.C., Hong, Z.S., Cheng, M.J., and Goddard, W.A. (2019). Mechanism and kinetics for both thermal and electrochemical reduction of N_2 catalysed by Ru(0001) based on quantum mechanics. Phys. Chem. Chem. Phys. *21*, 17605–17612.

150. Zhang, L., Mallikarjun Sharada, S., Singh, A.R., Rohr, B.A., Su, Y., Qiao, L., and Nørskov, J.K. (2018). A theoretical study of the effect of a non-aqueous proton donor on electrochemical ammonia synthesis. Phys. Chem. Chem. Phys. *20*, 4982–4989.

151. Ulissi, Z.W., Medford, A.J., Bligaard, T., and Nørskov, J.K. (2017). To address surface reaction network complexity using scaling relations machine learning and DFT calculations. Nat. Commun. *8*, 14621.

152. Jang, J., Gu, G.H., Noh, J., Kim, J., and Jung, Y. (2020). Structure-based synthesizability prediction of crystals using partially supervised learning. J. Am. Chem. Soc. *142*, 18836–18843.

153. Yang, C., Huang, B., Bai, S., Feng, Y., Shao, Q., and Huang, X. (2020). A generalized surface chalcogenation strategy for boosting the electrochemical N_2 fixation of metal nanocrystals. Adv. Mater. *32*, e2001267.

154. Zhang, M., Choi, C., Huo, R., Gu, G.H., Hong, S., Yan, C., Xu, S., Robertson, A.W., Qiu, J., Jung, Y., and Sun, Z. (2020). Reduced graphene oxides with engineered defects enable efficient electrochemical reduction of dinitrogen to ammonia in wide pH range. Nano Energy *68*, 104323.

155. Jin, Z., Liu, C., Liu, Z., Han, J., Fang, Y., Han, Y., Niu, Y., Wu, Y., Sun, C., and Xu, Y. (2020). Rational design of hydroxyl-rich Ti_3C_2Tx MXene quantum dots for high-performance electrochemical N_2 reduction. Adv. Energy Mater. *10*, 2000797.

156. Xia, J., Yang, S.Z., Wang, B., Wu, P., Popovs, I., Li, H., Irle, S., Dai, S., and Zhu, H. (2020). Boosting electrosynthesis of ammonia on surface-engineered MXene Ti_3C_2. Nano Energy *72*, 104681.

157. Ahmed, M.I., Liu, C., Zhao, Y., Ren, W., Chen, X., Chen, S., and Zhao, C. (2020). Metal–sulfur linkages achieved by organic tethering of ruthenium nanocrystals for enhanced electrochemical nitrogen reduction. Angew. Chem. Int. Ed. Engl. *59*, 21465–21469.

158. Zou, H., Rong, W., Long, B., Ji, Y., and Duan, L. (2019). Corrosion-induced Cl-doped ultrathin graphdiyne toward electrocatalytic nitrogen reduction at ambient conditions. ACS Catal. *9*, 10649–10655.

159. Yang, Y., Zhang, L., Hu, Z., Zheng, Y., Tang, C., Chen, P., Wang, R., Qiu, K., Mao, J., Ling, T., and Qiao, S.-Z. (2020). The crucial role of charge accumulation and spin polarization in activating carbon-based catalysts for electrocatalytic nitrogen reduction. Angew. Chem. Int. Ed. Engl. *59*, 4525–4531.

160. Yang, M., Huo, R., Shen, H., Xia, Q., Qiu, J., Robertson, A.W., Li, X., and Sun, Z. (2020). Metal-tuned $W_{18}O_{49}$ for efficient electrocatalytic N_2 reduction. ACS Sustainable Chem. Eng. *8*, 2957–2963.

161. Wu, T., Zhu, X., Xing, Z., Mou, S., Li, C., Qiao, Y., Liu, Q., Luo, Y., Shi, X., Zhang, Y., and Sun, X. (2019). Greatly improving electrochemical N_2 reduction over TiO_2 nanoparticles by iron doping. Angew. Chem. Int. Ed. Engl. *58*, 18449–18453.

162. Chu, K., Cheng, Y.H., Li, Q.Q., Liu, Y.P., and Tian, Y. (2020). Fe-doping induced morphological changes, oxygen vacancies and Ce^{3+}–Ce^{3+} pairs in CeO_2 for promoting electrocatalytic nitrogen fixation. J. Mater. Chem. A *8*, 5865–5873.

163. Shi, M.M., Bao, D., Li, S.J., Wulan, B.R., Yan, J.M., and Jiang, Q. (2018). Anchoring PdCu amorphous nanocluster on graphene for electrochemical reduction of N_2 to NH_3 under ambient conditions in aqueous solution. Adv. Energy Mater. *8*, 1800124.

164. Yang, D., Chen, T., and Wang, Z. (2017). Electrochemical reduction of aqueous nitrogen (N_2) at a low overpotential on (110)-oriented Mo nanofilm. J. Mater. Chem. A *5*, 18967–18971.

165. Nazemi, M., Panikkanvalappil, S.R., and El-Sayed, M.A. (2018). Enhancing the rate of electrochemical nitrogen reduction reaction for ammonia synthesis under ambient conditions using hollow gold nanocages. Nano Energy *49*, 316–323.

166. Huang, L., Gu, X., and Zheng, G. (2019). Tuning active sites of MXene for efficient electrocatalytic N_2 fixation. Chem *5*, 15–17.

167. Zhang, L., Ji, X., Ren, X., Ma, Y., Shi, X., Tian, Z., Asiri, A.M., Chen, L., Tang, B., and Sun, X. (2018). Electrochemical ammonia synthesis via nitrogen reduction reaction on a MoS_2 catalyst: theoretical and experimental studies. Adv. Mater. *30*, e1800191.

168. Guo, X., and Huang, S. (2018). Tuning nitrogen reduction reaction activity via controllable Fe magnetic moment: A computational study of single Fe atom supported on defective graphene. Electrochim. Acta *284*, 392–399.

169. Li, Y., Kong, Y., Hou, Y., Yang, B., Li, Z., Lei, L., and Wen, Z. (2019). In situ growth of nitrogen-doped carbon-coated γ-Fe_2O_3 nanoparticles on carbon fabric for electrochemical N_2 fixation. ACS Sustain. Chem. Eng. *7*, 8853–8859.

170. Yang, X., Ling, F., Su, J., Zi, X., Zhang, H., Zhang, H., Li, J., Zhou, M., and Wang, Y. (2020). Insights into the role of cation vacancy for significantly enhanced electrochemical nitrogen reduction. Appl. Catal. B *264*, 118477.

171. Chu, K., Li, Q.Q., Liu, Y.P., Wang, J., and Cheng, Y.H. (2020). Filling the nitrogen vacancies with sulphur dopants in graphitic C_3N_4 for efficient and robust electrocatalytic nitrogen reduction. Appl. Catal. B *267*, 118693.

172. Tong, W., Huang, B., Wang, P., Li, L., Shao, Q., and Huang, X. (2020). Crystal-phase-engineered PdCu electrocatalyst for enhanced ammonia synthesis. Angew. Chem. Int. Ed. Engl. *59*, 2649–2653.

173. Li, J., Chen, S., Quan, F., Zhan, G., Jia, F., Ai, Z., and Zhang, L. (2020). Accelerated dinitrogen electroreduction to ammonia via interfacial polarization triggered by single-atom protrusions. Chem *6*, 885–901.

174. Zheng, J., Lyu, Y., Qiao, M., Veder, J.P., Marco, R.D., Bradley, J., Wang, R., Li, Y., Huang, A., Jiang, S.P., and Wang, S. (2019). Tuning the electron localization of gold enables the control of nitrogen-to-ammonia fixation. Angew. Chem. Int. Ed. Engl. *58*, 18604–18609.

175. McPherson, I., and Zhang, J. (2020). Can electrification of ammonia synthesis decrease its carbon footprint? Joule *4*, 12–14.